VIBRATIONALLY-ASSISTED COLLECTIVE QUANTUM OPTICAL EFFECTS

by
William Myles Brown

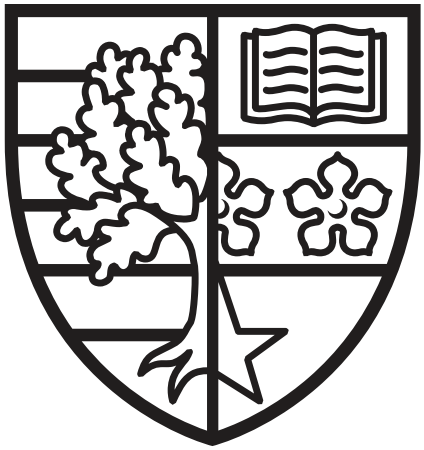

Submitted for the degree of
Doctor of Philosophy

Institute of Photonics and Quantum Sciences
School of Engineering and Physical Sciences

Heriot-Watt University

July 2020

Abstract

This thesis considers a variety of systems which are designed to take advantage of collective optical effects in the presence of a vibrational environment; a necessary condition for such systems to exist on a quantum platform outside of superconducting qubits. The first research chapter considers the effect of superabsorption, the time-reversed process of Dicke superradiance. A series of conditions for a guide-slide superabsorber are proposed, which allow a system to sacrifice some optical coupling for the benefit of still operating when coupled to a phonon bath. We suggest a system geometry which meets these properties, and then use this as a case study to show such a system does indeed display the hallmarks of superabsorbing behaviour. This remains when disorder is introduced to the system, as well as with a strongly-coupled vibrational environment in the polaron frame, amongst several other model extensions. The second research chapter looks at optical ratcheting, a process whereby an artificial light-harvester with an extraction bottleneck can improve performance by relaxing to a state which is dark with respect to optical relaxation, while still being able to absorb more photons. We examine how the performance scales with system size before looking at how the phenomena performs in the polaron frame. While strong vibrational coupling can be the undoing of collective optical effects, we find that it is still possible to observe ratcheting in the strong-coupling regime. We use the model as a platform to investigate more accurate means of incorporating extraction via a trap, by treating it as an additional dipole in the system. This change means one needs to consider both the optical and geometric properties of the trap to achieve optimal performance. The third research chapter stems from collaborative work with quantum biologists. We study the recently resolved structure of a photosynthetic complex, iron stress-induced protein A (IsiA), to establish if the structure allows the complex to utilise vibrational relaxation into a collectively dark delocalised state to reduce the likelihood of loss. By distorting different components, we establish which parts of the structure this effect is susceptible to changes in, providing insight into the function of the complex. Finally, the fourth research chapter investigates the feasibility of using a molecular aggregate of two identical absorbers as a gain medium in a laser. With adequate control of the geometry, we show that the combination of collective optical coupling and rapid vibrational relaxation make population inversion possible. By coupling a disordered collection of such systems to a resonant cavity, we demonstrate that a stable laser field can be generated. The results of this work support an approach derived by our collaborators, allowing larger, more complex aggregates to be used instead, which require less fine control over the molecular geometry to achieve lasing behaviour.

For Bessie and Colin,

who together embodied the principle that there is no substitute for curiosity, kindness, dedication, and practise; a lesson which I perhaps could have more readily applied in the preparation of this slightly delayed thesis. Greater success was had in teaching me that nothing tastes as good as homegrown fruit (specifically gooseberries), and that it is never too late to successfully hit a strike, dunk a basketball, or learn about quantum mechanics

. . . also the importance of always knowing when lunch is!

Acknowledgements

It is somewhat challenging to express quite how grateful I am to my supervisor Erik Gauger. His dedication and focus on both the quality of work produced by, and experience of his students is nothing short of inspirational, and the impact of his friendship and academic guidance throughout my studies cannot be understated. I am confident I would have been hard-pressed to find such a supportive and positive academic experience elsewhere as the one offered by his supervision of the Heriot-Watt Quantum Theory Team.

Moreover, I would like to gratefully acknowledge the important contributions to this thesis in collaborative works by (in alphabetical order) Francesco Mattiotti, Hanan Schoffman, Luca Celardo, Nicola Piovella, Nir Keren, Stefano Olivares, and Yossi Paltiel. Additionally, Dominic Rouse, Eleanor Scerri, and Oliver Brown deserve special mention for a range of interesting and insightful discussions that enlightened me on a variety of topics over the years, and without which this thesis would undoubtedly be notably shorter.

Furthermore, I would also like to thank the wider collective of QTT members, past and present, for making my entire time in the team so enjoyable, whether through the extensive range of events compiled by the Social Secretary, or our regular afternoon Brio's trips, even if it came at the cost that I now hardly ever drink instant coffee. In the same vein it has been great to be part of the IPaQS and UK Polaron Day researchers groups, which have provided their share of both stimulating academic discussions and entertainment over the years. The Scottish Condensed Matter Centre for Doctoral Training management team must also be credited for both their support, and the enrichment provided from my first day in Edinburgh, and I am specifically grateful to my fellow members of Cohort 7 for ensuring all of our in-person meetings were a delightful experience.

Finally, I wish to express my unending gratitude to all of my friends and family for their support, encouragement, and company throughout my time in Edinburgh, which helped to make it the amazing and unforgettable experience it has been.

For financial support throughout my studentship, I am indebted to the Scottish Condensed Matter Centre for Doctoral Training (EPSRC grant no. EP/L015110/1), alongside the Scottish Universities Physics Alliance, and Heriot-Watt University.

Contents

Chapter 1

Introduction

1.1 Motivation

In 1954, Dicke predicted that a collection of N identical excited optical emitters would relax with an enhanced optical decay rate, a phenomena which was coined 'superradiance' [1]. Rather than decaying over an exponential envelope N times larger than the envelope for a single emitter, as would be classically expected, Dicke predicted a 'superradiant pulse', whereby the emission rate would become proportional to N. This theorised collective quantum optical effect sparked interest in work looking at direct practical applications, such as a experimental observation of the effect [2, 3], and a proposal for a superradiant lasing system[4], as well as additional work into other collective effects. Single photon superradience, for example, is where a single excitation is in a delocalised state of a collection of N identical emitters, and the decay occurs N times faster than it would for a single emitter [5], while single photon subradiance is where a group of emitters can hold onto an excitation for longer than would be classically expected for a constituent emitter [6, 7].

There are a variety of applications, like the superradient laser mentioned above, for which these collective effects might be able to offer a quantum advantage over classical counterparts. One approach is to improve the design of detectors by utilising designs with interacting components [8, 9, 10]. Taking advantage of subradiance for the purpose of developing energy storage solutions has also been suggested [11]. One such example is a Dicke quantum battery which uses collectively-enhanced coupling to charge and then subradient states for storage. This is achieved by applying an external field to a collection of identical quantum subsystems [12, 13, 14]. Light-harvesters is another area where such effects could be beneficial. Taking advantage of the astronomical power source that is the Sun for the benefit of mankind is an endeavour which is classically bound by the Shockley-Queisser limit [15]. The limit considers the maximum efficiency a band gap absorber could achieve when capturing light from a black body spectrum, with losses from incident photons with energies which are beneath the band gap, or due to relaxation processes for those with en-

ergies above the band gap. For a blackbody at 6000 K , the limit is roughly 30%. There have been several suggestions relying on quantum mechanics for methods to surpass this limit [16, 17, 18, 19, 20, 21, 22].

One thing to be aware of in quantum technologies is interactions with environments. Quantum states can be influenced by external factors causing the systems to leave the desired states needed for quantum schemes to work [10, 23]. This can be a major contributor to the difficulties in developing such systems, with an obvious case study being the progress of developing a quantum computer from the conception of the idea in 1980 [24], to the carefully constructed, clean systems being developed today which can require cryogenic temperatures to limit noise.

Nature, after billions of years of evolution, may have some part to play in informing designs we choose to use for such quantum technologies. Photosynthesis, for example, powers most life on Earth [25] and has been used as inspiration for some artificial light-harvesting applications [26, 27, 28]. Results from a few areas in the field of quantum biology have found evidence to support the suggestion that Nature harnesses quantum effects for its benefit, despite the systems being considerably more noisy and disordered than those being considered in a typical experimental lab.

The question of whether photosynthesis relies on quantum mechanics has been considered for some time [29], with particular focus on the high efficiency with which absorbed photons arrive at the reaction centre, where the excitations are transformed into chemical energy to be used by the rest of the organism [30, 31, 32]. One of the most commonly studied complexes for transferring excitations is the Fenna-Matthews-Olsen (FMO) complex, which is found in green-sulphur bacteria [33]. The FMO complex is made up of seven or eight bacteriochlorophyll molecules surrounded by a noisy protein structure, which acts as the environment for the combined system. Despite short electronic excitation lifetimes on the order of nanoseconds [34], yet nearly all arrive at the reaction centre. This claim is also supported by quantum coherent wave-like motion of excitations observed with electronic spectroscopy [35, 36, 37]. It should be noted however that there is ongoing discussion about whether such coherent results are due to the nature of excitation in the specific experimental setup, calling into question whether it occurs under natural incoherent sunlight conditions [38].

As well as efficient energy transport in photosynthesis, quantum biologists have taken interest in the absorption process. Some aquatic systems, for example, are able to thrive despite being found deep in murky water [39, 40], where ambient light levels are are a few photons per molecule per second, much lower than the photon density surface organisms recieve. This provides some evidence for the efficiency of solutions Nature has developed over the course of evolution. Geothermal radiation from hydrothermal deep-sea vents is used by green sulphur bacteria, rather

than sunlight, as an alternative source of weak incoherent excitation [41]. These efficient light-harvesting solutions that operate even in harsh environments has inspired work studying the symmetric structures of molecular aggregates Nature employs to harvest and transport energy [42, 43].

There are two other examples where quantum mechanics is believed to be involved in processes inside biological systems. These are not directly related to light-harvesting and collective optical effects, but still act as inspiration for ways to control quantum states in messy environments. Firstly there is the avian compass, studied in European robins, that are capable of migrating south on their own in their first winter with no influence from other other robins who have already made the journey. After a proposal that birds are able to perceive the Earth's magnetic field as a form of heads-up display [44]. A scheme was proposed where, due to Zeeman splitting, incident photons create singlet states in a compound found inside the robin's retina. This singlet would then be sensitive to the direction of a magnetic field [45, 46, 47]. Working off of data from studies involving live robins [48, 49], it was shown that long-lived coherence times, on the order of tens of microseconds, would need to be possible within the messy biological systems [50, 51]. A second case is the sense of smell. One study has found that fruit flies are able to distinguish between different isotopes of hydrogen and deuterium in identical structures in odourants [52]. This implies that a vibrational spectrometer is being used to identify compounds, rather than just the shape or chemical properties, though this is still debated [53, 54].

1.2 Outline

Taking inspiration from Nature, this thesis focuses on systems that can take advantage of collective quantum optical effects, where the inclusion of realistic features like a room temperature vibrational environment, and disorder amongst the system components still allow the system to function. Such systems not only operate in spite of the inclusion of a warm vibrational environment, but in fact rely on it to operate optimally.

After a brief overview of some of the mathematical techniques that are implemented throughout this thesis the first two chapters focus on artificial light-harvesting proposals. Chapter 2 looks at the requirements needed to achieve 'superabsorption', a phenomena suggested in a publication in 2014 [10], which an experimental study recently reported the observation of using atomic sytstems [55]. Our study builds on the original work, developing a model that shows that while bold in scope, the model proposed would not operate effectively in a system which is coupled to a vibrational environment, i.e. any quantum platform other than superconducting qubits. Instead we propose a list of properties for a 'guide-slide superabsorber'

and then suggest a system configuration that would meet such conditions. We then perform a variety of tests and extensions to confirm the robustness of the superabsorbing behaviour in the proposed system. Such tests include introducing disorder, strong vibrational coupling via a polaron transformation [56], as well as introduction of additional non-radiative loss mechanisms. The work from this chapter has been published in Ref. [23].

Chapter 3 focuses on optical ratcheting, a proposal that takes advantage of collective effects in a an artificial light-harvester to prevent through vibration relaxation the loss of a photon after an absorption event, while still being able to achieve further absorption [19]. A useful trait if the transfer and conversion of energy is a bottleneck in a system. Our work significantly expands on the original proposal and tests its validity in more realistic circumstances. By looking at varied system sizes to confirm the optimal distribution of antennae for such a system. This model is also expanded to include strong vibrational coupling to see how that effects performance, and a more realistic implementation for modelling the extraction via a trap site is developed. The results from this work are currently being developed for a manuscript in the near future.

Having studied examples of collective effects in artificial light-harvesters in Chapters 2 and 3, Chapter 4 looks at the possibility such collective effects are being utilised in a photosynthetic system. The structure of iron stress-induced protein A (IsiA), a complex for which the purpose is still a point of debate in quantum biology, has recently been resolved [57]. Working with collaborators in that field we apply our model to see if this system might be taking advantage of optical darkness to hold onto excitations for longer than would be classically expected before reemission. Optical ratcheting in Chapters 3 is an idealised version of such an effect, whereby an excitation would never decay via optical pathways in a precisely-designed and symmetrically ordered system [19]. While photosynthetic complexes contain too many components, and are too messy to achieve prefect optical darkness they can still obtain some advantage. By introducing disorder to the different components in the system we could establish how resilient such an effect is, as well as which components are more influential in such behaviour, an important result for gaining biological insight. The collaborative work in this chapter has been compiled into a manuscript which is currently under review for publication [58].

The final research chapter, Chapter 5, presents work completed as part of a collaborative project on a laser proposal based on molecular aggregates. By initially considering a collective system of two identical molecules, we show that with adequate control of the molecule positioning one can expect population inversion from coupling such a system to a shared optical bath simulating solar excitement, as well as vibrational environments. By enhancing one optical transition and suppressing another, vibrational relaxation can rapidly move the system to a lasing state af-

ter absorption. By coupling our system to a semi classical field, and looking for agreement between our results and those of our collaborators, we give validity to their approach which is able to model larger structures, which have less stringent requirements on the design control necessary for a lasing system. A manuscript for a paper has been produced from the work of this collaboration, which is currently under review for publication [59].

While the approaches we typically take are general for quantum systems, we typically choose parameters which are suited to molecular systems. In the latter two chapters this is dictated by the scope of the work, but in the first two chapters, where we propose schemes for artificial light-harvesters and could potentially fit the model to use parameters for any platform. We choose molecules because of the balance of brightness and potential for small separations [60, 61, 62]. The proposal of constructing molecular light-harvesting systems using DNA origami has already been suggested [63], a promising step for the feasibility of synthesising the structures we propose. Additionally, molecular porphyrin nano-ring structures have been artificially synthesised [64, 65].

1.3 Background theory

1.3.1 Open quantum systems introduction

In the following section we will outline some of the techniques which are used regularly in the research chapters of this thesis. The theory primarily follows the work found in Refs. [66, 67].

When modelling systems which are coupled to environments, we write the Hamiltonian for the total system as

$$\hat{H}_{tot} = \hat{H}_S + \hat{H}_I + \hat{H}_E \ , \tag{1.1}$$

where $\hat{H}_S$ and $\hat{H}_E$ are respectively the system Hamiltonian, which only contains terms that act on the system Hilbert space, and the environment Hamiltonian, which only contains terms that act on the environment Hilbert space. The third term, $\hat{H}_I$, is the interaction Hamiltonian, which contains terms which act in both Hilbert spaces. System surroundings are modelled as a potentially infinite bath of oscillators, allowing them to replicate a wide range of possible environments.

To determine the evolution of such a system, one uses the interaction picture (denoted with a tilde), performing the unitary transformation on $\hat{H}_I$ to give

$$\tilde{\hat{H}}_I(t) = \hat{U}_0^\dagger(t, t_0)\hat{H}_I\hat{U}_0(t, t_0) \ , \tag{1.2}$$

where

$$\hat{U}_0(t, t_0) = e^{-i(\hat{H}_S + \hat{H}_E)t} \ . \tag{1.3}$$

If one assumes a generic interaction Hamiltonian form, $\hat{A} \otimes \hat{B}$, where $\hat{A}$ is the system components of the interaction, and $\hat{B}$ is the bath components, this transformation to the interaction picture gives

$$\hat{\tilde{H}}_I(t) = \sum_\omega e^{-i\omega t} \hat{A}(\omega) \otimes \hat{B}(t) = \sum_\omega e^{i\omega t} \hat{A}^\dagger(\omega) \otimes \hat{B}^\dagger(t) \ , \tag{1.4}$$

where ω is the change in system energy associated with the process $\hat{A}(\omega)$ and the environment terms pick up similar frequency dependence with

$$\hat{B}(t) = e^{i\hat{H}_E t} \hat{B} e^{-i\hat{H}_E t} \ . \tag{1.5}$$

It is also important to note that

$$\hat{A}^\dagger(\omega) = \hat{A}(-\omega) \ . \tag{1.6}$$

1.3.2 Evolution

The evolution of the entire system is both computationally demanding and not very interesting. We want to understand the evolution of the system. If the system was isolated with no coupling to the environment, the behaviour would be determined by the unitary dynamics,

$$\frac{d}{dt}\tilde{\rho}_S(t) = -i[\hat{H}_S, \rho_S] \ , \tag{1.7}$$

where ρ_S is the reduced density matrix for the system. The effect of the dissipative dynamics, which appear as a result of coupling to an environment can be written in the interaction picture, and solved to second order using two main assumptions:

1. The system is small compared to the environment, and as such does not influence it.

2. The historical behaviour of the system has no impact on the future behaviour.

After these assumptions, the form of dissipative dynamics is

$$\frac{d}{dt}\tilde{\rho}_S(t) = -\int_0^\infty ds \mathrm{Tr}_B\big[\hat{\tilde{H}}_I(t), [\hat{\tilde{H}}_I(t-s), \tilde{\rho}_S(t) \otimes \tilde{\rho}_B]\big] \ , \tag{1.8}$$

where $\tilde{\rho}_S$ and $\tilde{\rho}_B$ are the reduced density matrices in the interaction picture for the system and environment respectively.

With these included, one can write the Born-Markov master equation in the

interaction picture as

$$\frac{d}{dt}\tilde{\rho}_S(t) = \sum_{n,m}\sum_{\omega,\omega'}\Bigg(e^{i(\omega'-\omega)t}\hat{A}_m(\omega)\tilde{\rho}_S(t)\hat{A}_n^\dagger(\omega')\Gamma_{nm}(\omega) + e^{-i(\omega'-\omega)t}\hat{A}_n(\omega')\tilde{\rho}_S(t)\hat{A}_m^\dagger(\omega)\Gamma_{nm}^\dagger(\omega) - e^{-i(\omega'-\omega)t}\tilde{\rho}_S(t)\hat{A}_m^\dagger(\omega)\hat{A}_n(\omega')\Gamma_{nm}^\dagger(\omega) - e^{i(\omega'-\omega)t}\hat{A}_n^\dagger(\omega')\hat{A}_m(\omega)\tilde{\rho}_S(t)\Gamma_{nm}(\omega)\Bigg) , \quad (1.9)$$

where environment correlation functions of the form

$$\Gamma_{nm}(\omega) = \int_0^\infty ds e^{i\omega s}\,\langle \hat{B}_n^\dagger(t)\hat{B}_m(t-s)\rangle \ , \qquad \Gamma_{nm}^\dagger(\omega) = \int_0^\infty ds e^{-i\omega s}\,\langle \hat{B}_m^\dagger(t-s)\hat{B}_n(t)\rangle \ , \quad (1.10)$$

are included, in which

$$\langle \hat{B}_n^\dagger(t)\hat{B}_m(t-s)\rangle = \mathrm{Tr}_B\Big(\hat{B}_n^\dagger(t)\hat{B}_m(t-s)\tilde{\rho}_B\Big) \ . \quad (1.11)$$

Returning to the Schrödinger picture, one can write the a Bloch-Redfield dissipator as

$$\mathcal{D} = \sum_{n,m}\sum_{\omega,\omega'}\Bigg(\hat{A}_m(\omega)\rho_S\hat{A}_n^\dagger(\omega')\Gamma_{nm}(\omega) + \hat{A}_n(\omega')\rho_S\hat{A}_m^\dagger(\omega)\Gamma_{nm}^\dagger(\omega) - \rho_S\hat{A}_m^\dagger(\omega)\hat{A}_n(\omega')\Gamma_{nm}^\dagger(\omega) - \hat{A}_n^\dagger(\omega')\hat{A}_m(\omega)\rho_S\Gamma_{nm}(\omega)\Bigg) , \quad (1.12)$$

which gives the dissipative dynamics induced in the system by the coupling to an environment. By forming dissipators for all of the different environments one can write out the evolution as for the system by adding the dissipators to the unitary dynamics:

$$\frac{d}{dt}\rho_S = -i[\hat{H}_S, \rho_S] + \sum_i \mathcal{D}_i \ . \quad (1.13)$$

It should be noted that one can perform a rotating wave approximation by only considering terms where $\omega = \omega'$, leading to a secular Lindblad form. This greatly reduces the number of terms that need to be considered, but potentially causes problems if there are near degenerate terms ($\omega \approx \omega'$) which are relevant to the dynamics but dropped in this approximation. For this reason we typically avoid such an approximation, and instead calculate the complete Bloch-Redfield dissipators.

1.3.3 Bath correlation functions

The environment correlation functions are calculated by assuming the environment is in a thermal state. The result will be the same regardless of picture, so here we

revert to the Schrödinger picture. The bath density operator becomes

$$\rho_E = \frac{1}{Z_E} e^{-\beta \hat{H}_E} = \frac{e^{-\beta \hat{H}_E}}{\mathrm{Tr}[e^{-\beta \hat{H}_E}]} \ , \tag{1.14}$$

where $\beta = 1/k_B T$ is the inverse thermal energy of the bath. For a multi-mode bath one can write

$$\frac{1}{\mathrm{Tr}[e^{-\beta \hat{H}_E}]} = \prod_k 1 - e^{-\beta \hbar \omega_k} \ . \tag{1.15}$$

One can then solve for the expectation values of different bath operator pairings to find

$$\begin{aligned}
\langle \hat{b}_k \hat{b}_{k'}^\dagger \rangle &= \delta_{k,k'} \big(1 + n(\omega_k)\big) \ , \\
\langle \hat{b}_k^\dagger \hat{b}_{k'} \rangle &= \delta_{k,k'} n(\omega_k) \ , \\
\langle \hat{b}_k \hat{b}_{k'} \rangle &= 0 \ , \\
\langle \hat{b}_k^\dagger \hat{b}_{k'}^\dagger \rangle &= 0 \ ,
\end{aligned} \tag{1.16}$$

where k denotes the mode, and

$$n(\omega_k) = \frac{1}{e^{\beta \hbar \omega_k} - 1} \ , \tag{1.17}$$

is the Planck distribution. Since $n(-\omega) = -(1 + n(\omega)))$, one can state that terms which increase a systems energy by ω will have an environment-dependent rate proportional to $n(\omega)$, whilst a relaxation process will have a rate proportional to $(1 + n(\omega))$. Accounting for this, one can write the correlation function terms as

$$\Gamma_{nm}(\omega) = \delta_{nm} \left(\frac{1}{2} \gamma(\omega) + i S(\omega) \right) \ , \tag{1.18}$$

$$\Gamma_{nm}^\dagger(\omega) = \delta_{nm} \left(\frac{1}{2} \gamma(\omega) - i S(\omega) \right) \ , \tag{1.19}$$

where the dissipative rates are

$$\gamma(\omega) \propto \big(1 + n(\omega)\big) \ . \tag{1.20}$$

The imaginary terms, $S(\omega)$, lead to renormalisation effects in the system energy scales. It is possible to ignore these effects and assume such a renormalisation has already occurred when defining system energies, reducing the calculations that need to be completed.

1.3.4 Optical processes

When considering coupling of a single dipole with dipole moment $\boldsymbol{d}$, modelled as a two level system (2LS) to an optical field, the quantum optical interaction Hamiltonian is given by

$$\hat{H}_{I,\mathrm{opt}} = -\hat{\hat{\boldsymbol{D}}} \cdot \hat{\boldsymbol{E}} \ , \tag{1.21}$$

where the dipole operator of the system is $\hat{\boldsymbol{D}} = \boldsymbol{d}\hat{\sigma}^x$ (using Pauli spin operators) and $\hat{\boldsymbol{E}}$ is the Schrödinger picture electric field operator:

$$\hat{\boldsymbol{E}} = i\sum_k \sum_{\lambda=1,2} \sqrt{\frac{2\pi\hbar\omega_k}{V}} \boldsymbol{e}_\lambda(\boldsymbol{k})(\hat{b}_{k,\lambda} - \hat{b}^\dagger_{k,\lambda}) \ . \tag{1.22}$$

Here, $\hat{b}^{(\dagger)}_{k,\lambda}$ represents the annihilation (creation) operator for the optical mode k, with polarisation λ.

The dipole moments we typically consider are transition dipoles, rather than permanent dipole moments. Permanent dipoles arise in molecules where two atoms attract electrons unevenly, causing an uneven buildup of charge, resulting in a permanent static dipole. By contrast, transition dipoles couple to radiation, allowing transitions between charge states with different wavefunctions and associated probability distribution for electrons, producing a dipole.

When we calculate the environment correlation terms for this interaction to find the rates we get

$$\begin{aligned} \gamma(\omega) &= \frac{4\omega^3|\boldsymbol{d}|^2}{3\hbar c^3}\big(1 + n(\omega)\big) \ , \\ &= \gamma_{\mathrm{opt}}\big(1 + n(\omega)\big) \ , \end{aligned} \tag{1.23}$$

where γ_{opt} is the spontaneous decay rate of the 2LS, which is proportional to the cube of the transition frequency of the optical transition in the single system.

As we will consider multiple, typically identical systems connected to the same optical bath throughout this thesis, there are two important features to discuss.

Firstly, the imaginary components of the environment correlation functions as well as inducing renormalising shifts in system energy scales (as discussed above) also induce off-diagonal terms in the system Hamiltonian. These induced couplings allow excitations to hop between absorbers, and they are Förster-type dipole-dipole couplings. As with the renormalisation of the system energies, we will always include the effect from the start in our system Hamiltonian, and then consider it to have already been renormalised, meaning we only need to calculate the dissipative dynamics.

Secondly, the induced couplings will cause shifts in the system eigenenergies, meaning optical transitions will cover different frequencies depending on the eigenstates being considered, changing the ω^3 dependence in the dissipative rates. To

account for this, we take define

$$\kappa_{\text{opt}} = \frac{\gamma_{\text{opt}}}{\omega_A^3} \ , \tag{1.24}$$

where ω_A is the transition frequency of the 2LSs making up the system. This allows the dissipative rates for a transition linking shifted eigenstates with transition frequency ω_k and transition dipole moment $\boldsymbol{d}_k$ to be written as

$$\gamma(\omega_k) = \frac{|\boldsymbol{d}_k|^2}{|\boldsymbol{d}|^2}\kappa_{\text{opt}}\omega_k^3\big(1 + n(\omega_k)\big) \ . \tag{1.25}$$

1.3.5 Vibrational processes

Coupling a single 2LS to a vibrational bath is done with a spin-boson interaction Hamiltonian [66]:

$$\hat{H}_{I,\text{vib}} = \hat{\sigma}^z \otimes \sum_q g_q(\hat{b}_q + \hat{b}_q^\dagger) \ , \tag{1.26}$$

where g_q and $\hat{b}_q^{(\dagger)}$ are, respectively, the coupling strength and annihilation (creation) operator for the phonon mode q. This coupling can induce small shifts in system energy levels and dephasing effects anticipated from vibrational interaction.

The rates for phonon excitation and relaxation processes are derived from the environment correlation terms which are calculated over a pair of environment interaction terms as was shown in Eq. 1.10. Following Ref. [68], the coupling strength for electron-phonon interactions with a flat spectral density has the proportionality

$$g_q \propto \sqrt{\frac{\hbar}{2\mu V\omega_q}} \ , \tag{1.27}$$

where μ is the mass density of the solid. The main difference between this form and the coupling of the quantum optical master equation in Eq. 1.22 is the frequency dependence, which has changed from $\sqrt{\omega}$ to $\sqrt{\omega^{-1}}$. And when we calculates the rates we find

$$\begin{aligned}\gamma(\omega) &\propto \omega\big(1 + n(\omega)\big) \ , \\ &= \gamma_{\text{vib}}\big(1 + n(\omega)\big) \ .\end{aligned} \tag{1.28}$$

Similar to the treatment with photons, we define a base phonon timescale, γ_{vib} which we typically choose to be 1 ps, and then we calculate an average transition frequency for phonon transitions, $\overline{\omega_{\text{vib}}}$. This is because we will consider systems with vibration transitions of varying size. We can then define

$$\kappa_{\text{vib}} = \frac{\gamma_{\text{vib}}}{\overline{\omega_{\text{vib}}}} \ , \tag{1.29}$$

as the prefactor for determining phonon process rates:

$$\gamma(\omega) = \kappa_{\text{vib}}\omega\big(1 + n(\omega)\big) \ . \tag{1.30}$$

It should be noted that this approach is suitable for weakly-coupled phonon environments. Modelling strongly-coupled phonon environments will be discussed later.

1.3.6 Additional dissipators

Throughout this thesis we will also introduce phenomenological dissipators, to include additional processes such as decay at a sink site, non-radiative loss, or additional dephasing processes. In these instances we will construct an interaction term, $\hat{X}$, that covers the expected phenomenological behaviour in the system Hilbert space, either defined in the site basis or the energy basis depending on purpose. A dissipator is then constructed, $\mathcal{D}_x$, based on Eq. 1.12, with the form

$$\mathcal{D}_x = \gamma_x \sum_{n,m} \left(\hat{X}_m \rho_S \hat{X}_n^\dagger + \hat{X}_n \rho_S \hat{X}_m^\dagger - \rho_S \hat{X}_m^\dagger \hat{X}_n - \hat{X}_n^\dagger \hat{X}_m \rho_S\right) \ , \tag{1.31}$$

where $\hat{X}_\alpha$ are the components of the interaction term, and γ_x is the phenomenological rate. For these phenomenological processes we set $n = m$ to produce a dissipator with Lindblad form.

1.3.7 Calculation of steady states

Once the dissipators have been formed for the system evolution, one can write the master equation governing the evolution as

$$\frac{d}{dt}\rho_S = -i[\hat{H}_S, \rho_S] + \sum_i \mathcal{D}_i \ , \tag{1.32}$$

which can be rewritten in the Liouvillian ($\mathcal{L}$) form

$$\frac{d}{dt}\rho_S = \mathcal{L}\rho_S \ , \tag{1.33}$$

with the formal solution

$$\rho_S(t) = e^{\mathcal{L}t}\rho_S(0) \ . \tag{1.34}$$

By diagonalising the Liouvillian, the master equation becomes

$$\rho_S(t) = \begin{pmatrix} e^{\lambda_1 t} & 0 & \cdots \\ 0 & e^{\lambda_2 t} & \cdots \\ \vdots & \vdots & \ddots \end{pmatrix} \rho_S(0) \ , \tag{1.35}$$

where λ_i are the complex eigenvalues of $\mathcal{L}$. When all eigenstates of the system Hamiltonian are connected by the dissipative processes, there is a unique steady state, leading to a single zero-valued eigenvalue for the Liouvillian (all others having negative real parts). As $t \to \infty$ only the eigenstate with associated $\Re(\lambda) = 0$ survives, and the steady state of the system is then given by this eigenvector, regardless of the initial system state. By only calculating the two smallest eigenvalues for $\mathcal{L}$ one can confirm that only one is zero and solve for the steady state efficiently.

If however, there are multiple steady states for a system, which can occur in some of the systems we look at later if optical and vibrational processes are not both included, then one will have multiple zero-value eigenvalues. In this case one needs to define an initial state to calculate the steady state arising from all the non-decaying components in Eq. 1.35. To do this one still needs to calculate all of the eigenvalues however, as the representation of the initial state needs to be transformed to the eigenbasis of $\mathcal{L}$ to calculate the weights of the different eigenvectors which then need to be transformed back to the lab frame of $\mathcal{L}$ for a solution. Needing to solve for all eigenvalues is more time consuming than when there is a single zero-value eigenstate, but more efficient than solving for long timescales, as needs to be done when there is no steady state.

We now have all of the components in place to start examining the applications of collective optical interactions in systems with vibrational environments, such as typical condensed matter systems, over the following research chapters.

Chapter 2

Guide-Slide Superabsorption

2.1 Introduction

This chapter is focused on the work published in Ref. [23], in which we present a proposal for light-harvesting systems which exhibit a super-linear scaling of power output with system size. After proposing the necessary properties for such a system, we propose a biologically-inspired ring design (see Fig. 2.1), and then benchmark its performance. With appropriate design, such a system is aided, rather than hindered by vibrational interactions, and is in fact robust against significant disorder in both the dipole geometry and optical parameters.

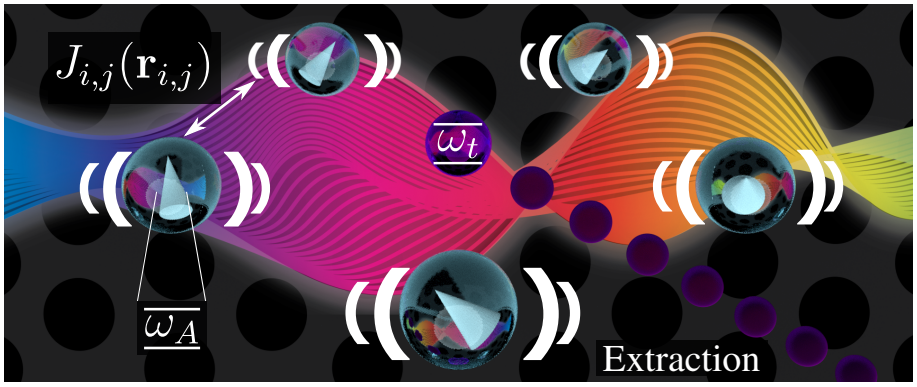

Figure 2.1: Artistic depiction of a guide-slide superabsorber: A ring of skewed optical dipoles interacting with a shared photon environment, local phonon baths, and a central extracting trap. A photonic crystal suppresses interaction with certain optical modes.

There have been several proposals over the last few years for pushing photovoltaic devices beyond the traditional limit of photocells stated by the Shockley-Queisser limit [15] by using quantum mechanics. Such proposals have centred around limiting emission using interference in multi-level systems [16, 69], as well as dark-state protection in systems of multiple interacting dipoles [17, 70, 18, 71, 72]. Optical

ratcheting [19, 73] is another proposal, uses darkness to prevent relaxation, while still being able to absorb photons, which will be discussed in greater detail in Chapter 3.

Rather than limiting emission, an alternative way to improve the performance of a photocells is to increase the absorption. Superradiance, where N atoms exhibit a collectively-enhanced emission rate proportional to N^2, was first proposed by Dicke in 1954 [1]. The light-harvesting proposal, which utilises the time-reversed phenomenon, is called superabsoprtion [10]. This original proposal relies on lifting degeneracies in the system by introducing symmetric dipole interactions between a ring of absorbers, allowing the system to maintain superabsorbing behaviour. Superabsorption is a multi-excitation effect, occurring when half of the absorbers in the collective system are excited, for this reason it would not be expected to occur in natural light-harvesting complexes, but the ring design was inspired by the rings of photosynthetic antennae which surround reaction centres where absorbed excitations are converted to useful chemical energy in nature [74, 75]. These biological systems, which will be discussed in greater detail in Chapter 4, are different from the artificial absorbers we discuss here as their design tends to align dipoles tangentially around the ring [76], and also includes mechanisms for preventing photo-damage [77]. Artificial systems on the other hand, which are solely concerned with capturing and converting as much energy as possible, can benefit from a strong collective dipole.

In this chapter we examine the potential of condensed matter nanostructures to act as superabsorbers. We show that the original dipole geometry proposal for superabsorption (Ref. [10]) does not work in the presence of a vibrational environment. We therefore propose a 'guide-slide superabsorber', as a collection of optical dipoles which possess the following properties:

1. A ladder of excitation manifolds, with rapid relaxation to a well-defined lowest energy state in each.

2. Collectively enhanced optical transitions linking the lowest energy states of neighbouring manifolds.

3. Spectral selectivity allowing the suppression of optical decay below an enhanced target transition.

As a candidate system for meeting these criteria, we propose a ring of 'skewed' optical dipoles.

2.2 Reference model

2.2.1 System components

We consider a ring of N dipoles (see Fig. 2.1), each modelled as a degenerate two-level system (2LS) with transition energy $\omega_A = 1.8$ eV ($\hbar = 1$), near the peak of the

solar power spectrum. Allowing N uncoupled dipoles to interact collectively with an electromagnetic environment leads to a Dicke ladder with $N+1$ equally spaced 'rungs' separated by steps of ω_A, as depicted in the left hand side of Fig. 2.2. The rungs each represent a collective state for a specific number of excitations in the system, from 0 to N. The optical rates linking these states are collectively enhanced with those at the ends of the ladder being proportional to N, and those at the middle being proportional to N^2 [1, 67]. The introduction of dipole-dipole interactions can perturb the Dicke picture, though the system still retains a ladder of eigenstates which are connected by enhanced optical transitions, but the ladder rungs are no longer evenly spaced spaced, as depicted in the right hand side of Fig. 2.2. Instead, one obtains a chirped profile with a frequency increment determined by the strength of the dipolar couplings [10].

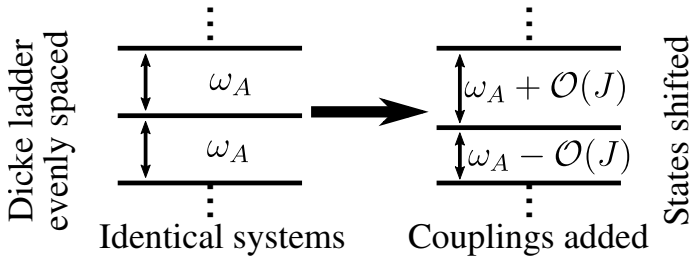

Figure 2.2: Couplings $J_{i,j}$ between dipoles cause a perturbation to the Dicke ladder, primarily lifting the degeneracy of ladder rung spacings.

Closely spaced absorbers, that are coupled to a collective optical bath experience Förster dipole-dipole coupling terms from the 'cross Lamb-shift' terms in the many body quantum optical master equation [78, 79, 66],

$$J_{i,j}(\boldsymbol{r}_{i,j}) = \frac{1}{4\pi\epsilon_0|\boldsymbol{r}_{i,j}|^3}\left(\boldsymbol{d}_i\cdot\boldsymbol{d}_j - \frac{3(\boldsymbol{r}_{i,j}\cdot\boldsymbol{d}_i)(\boldsymbol{r}_{i,j}\cdot\boldsymbol{d}_j)}{|\boldsymbol{r}_{i,j}|^2}\right), \tag{2.1}$$

where $\boldsymbol{r}_{i,j}$ is the vector linking the two dipoles i,j, and $\boldsymbol{d}_i$ is the dipole moment at site i whose strength is related to the natural lifetime τ_L of an isolated 2LS by $|\boldsymbol{d}| = \sqrt{3\pi\epsilon_0\tau_L^{-1}c^3/\omega_A^3}$ [80, 81].

We only consider dipole arrangements with symmetry around the ring, this is achieved by defining two angles, which are shown in Fig. 2.3 as a visual representation. The equatorial angle, θ_{eq}, gives rotation in the plane of the ring, and the zenith angle, θ_{zen} gives inclination. Both angles are defined locally relative to the radial vector from the ring centre to the absorber position.

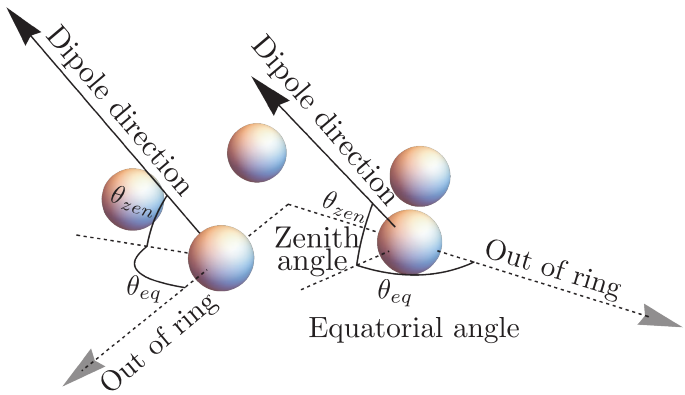

Figure 2.3: Representation in a pentamer of the equatorial angle, θ_{eq} and the zenith angle θ_{zen}, used to define dipole directions.

With the usual definition of Pauli operators, we write the ring Hamiltonian as

$$\hat{H}_{\text{ring}} = \omega_A \sum_{i=1}^{N} \hat{\sigma}_i^z + \sum_{i,j=1}^{N} J_{i,j}(\boldsymbol{r}_{i,j})(\hat{\sigma}_i^+ \hat{\sigma}_j^- + \hat{\sigma}_i^- \hat{\sigma}_j^+) \ . \tag{2.2}$$

As we assume a ring with a diameter that is small compared to relevant photon wavelengths ($\sim 2\pi c/\omega_A$) we write the multi-site quantum optical interaction Hamiltonian as

$$\hat{H}_{I,\text{opt}} = \sum_{i=1}^{N} \boldsymbol{d}_i \hat{\sigma}_i^x \otimes \sum_k f_k(\hat{a}_k + \hat{a}_k^\dagger) \ , \tag{2.3}$$

where f_k and $\hat{a}_k^{(\dagger)}$ are, respectively, the coupling strength and annihilation (creation) operator for the optical mode k [66, 10]. To model the condensed-matter nature of typical nanostructures, we introduce local vibrational baths which are generically coupled to each 2LS with a spin-boson type coupling [68]:

$$\hat{H}_{I,\text{vib}} = \sum_{i=1}^{N} \hat{\sigma}_i^z \otimes \sum_q g_{i,q}(\hat{b}_{i,q} + \hat{b}_{i,q}^\dagger) \ , \tag{2.4}$$

where $g_{i,q}$ and $\hat{b}_{i,q}^{(\dagger)}$ are, respectively, the coupling strength and annihilation (creation) operator for the phonon mode q for the bath associated with site i [66, 19].

2.2.2 Parallel setup

We consider two different symmetric setups for our ring system. The first is inspired by the original paper on superabsorption [10], where the dipoles are all perpendicular to the plane of the ring. We refer to this as parallel superabsorption (||-SA), since the dipole moments of all absorbers are parallel with each other. Using our two dipole angles, in this setup $\theta_{\text{zen}} = \pi/2$, and the choice of θ_{eq} is irrelevant. This choice maximises the collective optical dipole of the system, $\boldsymbol{D} = \sum_i^N \boldsymbol{d}_i$.

In Fig. 2.4 we show the eigenstates of an $N = 4$ ring (quadmer) in the ||-SA configuration. States linked by collectively-enhanced optical transitions, which overlap significantly with Dicke ladder states, are shown in the left-most column. For simplicity we still refer to these states as ladder states. The optical and vibrational processes which link the eigenstates are also depicted, with colour coding to indicate their relative strength. These strengths are the prefactor terms that affect both absorption and emission rates, including the cubic and ohmic frequency dependence of the free space spectral densities for optical and vibrational modes respectively, as discussed in Chapter 1 [66]. It can be seen that the ladder states in this setup each sit at the top of their respective excitation manifold. According to detailed balance one would therefore expect rapid vibrational relaxation to pull the system away from the optically enhanced transitions linking the ladder states [82, 83].

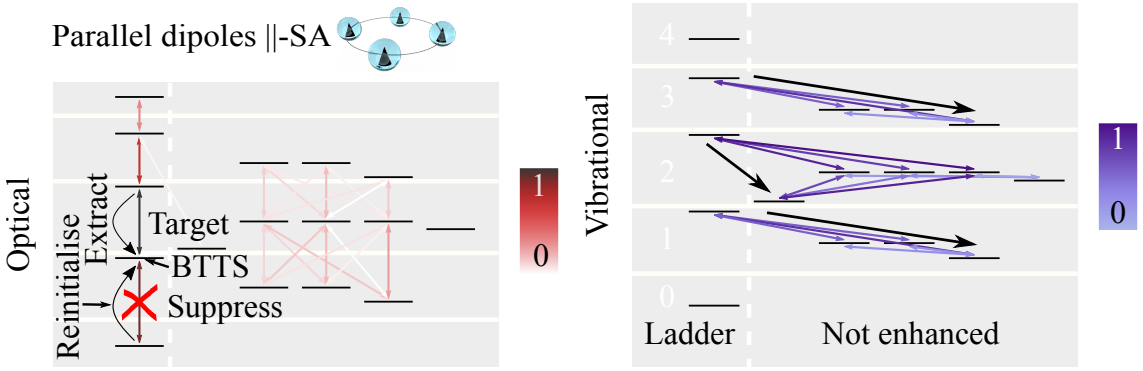

Figure 2.4: Process diagram showing optical (red, left) and vibrational (blue, right) processes linking the eigenstates for a quadmer in the ||-SA setup. Normalised colour on the arrows denotes relative strengths. The states are organised in manifolds corresponding to the number of excitations in the system; the manifolds are visually separated by gaps in the background shading. Optical processes link different manifolds whereas vibrational ones act 'sideways'. Energy separations between manifolds and states within manifolds are not to scale. Superabsorption relies on pairing a reinitialisation process with a suppression of optical decay below the collectively-enhanced 'target' transition to keep the system in a superabsorbing state, but black arrows show how vibrational relaxation will pull the system away from superabsorbing ladder states.

2.2.3 Guide-slide proposal

For our 'skewed' dipole arrangement we set $\theta_{\text{zen}} = \pi/4$, and $\theta_{\text{eq}} = \pi/2$. This set up is referred to as our guide-slide setup (GS-SA). This choice of geometry changes the sign of the nearest neighbour dipole coupling between dipoles (Eq. 2.1).

In Fig. 2.5 we show the eigenstates of a quadmer in the GS-SA configuration. The

ladder states now each sit at the bottom of their respective manifold, meaning vibrational relaxation pushes the system back towards the enhanced ladder behaviour if it departs from it. It should also be noted that the optical processes are only for the collective dipole, $\boldsymbol{D}$, and a full process heatmap for this system is shown in Fig. 2.6.

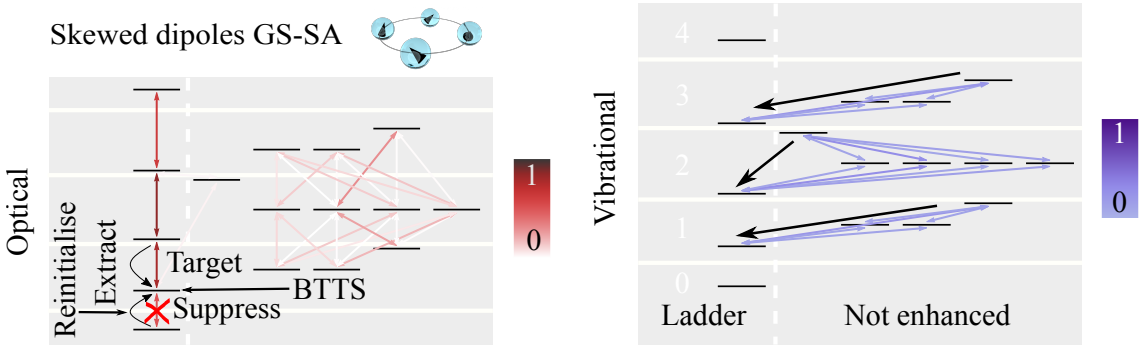

Figure 2.5: Process diagram for a quadmer in the GS-SA setup. The rules for setting up the panels are the same as are used in Fig. 2.4. Black arrows show how the superabsorbing behaviour is encouraged by vibrational relaxation.

As was mentioned above, the optical process map for GS-SA presented in Fig. 2.5 only accounts for the collective coupling (in the direction perpendicular to the plane of the ring), $\boldsymbol{D} = \sum_i^N \boldsymbol{d}_i$, which 71% of the overall dipole moment aligns with. The collective enhancement which we are primarily interested in can be sufficiently explained using just this shared direction, but our model also accounts for coupling in the plane of the ring. The overlap of optical dipole directions in the plane of the ring means that for GS-SA one no longer has the total optical separation of symmetric and non-symmetric states that is present in ||-SA (denoted by the vertical dashed line in the figure). A complete process map of all optical processes is given in Fig. 2.6. Analysing this complete optical process map we see that for GS-SA there are additional optical pathways, and each ladder state is optically connected to the non-ladder states in adjacent manifolds above as well as below.

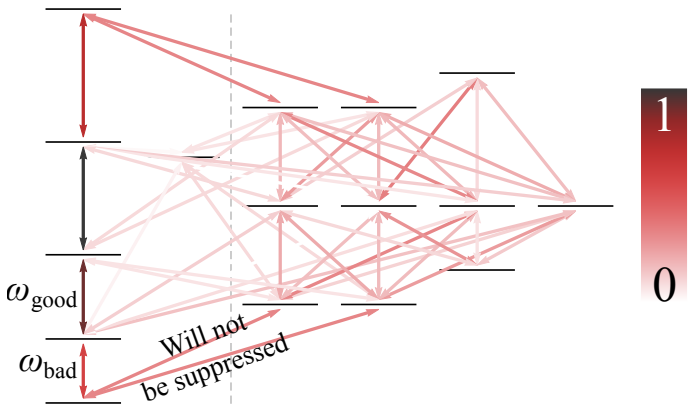

Figure 2.6: The optical process map for a GS-SA quadmer with the same parameters as those used in Fig. 2.5. All processes arising from the optical interaction Hamiltonian, which are all included in our numerical model, are shown. Notably, several processes now cross the dashed dividing line. The colouring of each line denotes the relative strength of each process, normalised against the strongest process on the map. For clarity, energy separations between the different states in this image are not to scale as intra-band spacings have been scaled up with respect to interband spacings.

The skewed GS-SA setup does maintain a significant proportion of the collective dipole strength, $\boldsymbol{D}$, but a sacrifice is made compared to ||-SA. To explore this further, in Fig. 2.7 we plot the dipole contribution to the optical rates of the central 'target' transition in the ladder as N is varied. We see that GS-SA displays superlinear scaling for $N > 3$ but trails behind ||-SA and the uncoupled Dicke model. Note that the gradient changes every two data points since the target transition lies at the centre of the ladder for a ring with an odd N, whereas for an even-sized ring it sits just below the middle. The disparity between the quadratic growth of the idealised uncoupled Dicke model and what is actually achievable has been observed experimentally in colour centres for diamond [84]. When we apply disorder to the GS-SA setup across all dipole parameters (energy splittings ω_A, natural lifetimes τ_L, positions $\boldsymbol{r}_i$, and dipole orientations), the pale distribution marks show the desired superlinear behaviour is maintained. Disorder is discussed in greater detail in a later section.

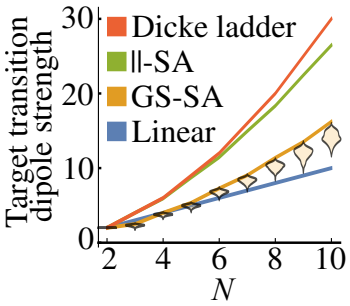

Figure 2.7: Scaling of oscillator strength of the light-havesting target-transition with system size for the different scenarios discussed. For GS-SA we also include the beige patches corresponding to distributions for 5% disorder introduced across model parameters (10 000 trials for up to $N = 7$, then 1 000, 500 and 50 trials for $N = 8, 9, 10$, respectively).

Having confirmed that our GS-SA setup should provide a superlinear scaling of optical coupling, we look at the components needed to take advantage of this scaling, as the target transitions sit at the centre of the excitation ladder and as such would not be expected to be very populated naturally. To be able to take advantage of the most enhanced transition, we need the system to naturally sit in the 'bottom-of-the-taget-transition-state', which we label as BTTS. We define the frequency of the target transition as ω_{good}, and the frequency of the ladder transition down from the BTTS as ω_{bad}. Following Ref [10], we use spectral selectivity to limit coupling to some optical modes. With sufficient separation between ω_{good} and ω_{bad}, the order of which is proportional to the magnitude of the nearest neighbour coupling, optical decay from the BTTS can be suppressed with a photonic band gap environment. In Fig. 2.8 we show that the ladder transitions above (green) and below (red) the BTTS are indeed well separated, meaning a single band of suppressed wavelengths will be effective. For GS-SA we suppress all modes with frequency $\omega < \omega_{cut}$, where $\omega_{cut} = (\omega_{\text{good}} + \omega_{\text{bad}})/2$.

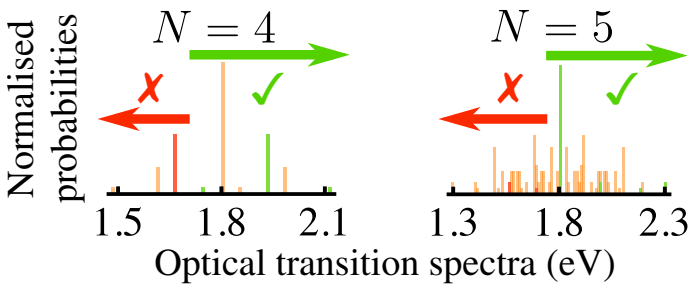

Figure 2.8: Histogram of transition frequencies for coupled dipoles using our proposed guide-slide superabsorber setup: there is no overlap between undesirable modes to be suppressed (red) and light-harvesting target modes (green) irrespective of ring size (discussed more in Fig. 2.9).

This cut-off frequency definition implies that all the collectively enhanced optical transitions will be suppressed beneath the target transition, as well as relaxation to any other (off-ladder) state in the manifold below. This relies on the fact that in GS-SA, the non-degenerate, enhanced optical transition frequencies increase as one moves up the ladder, as can be seen by the spacings of the states in Fig. 2.5, as well as Figs. 2.6 and 2.9. For the case of ||-SA, a similar process can be applied if instead one suppresses all modes above a certain threshold rather than below (see Fig. 2.4). We note that as well as suppressing undesirable optical modes, one could alternatively selectively enhance the transitions above the BTTS or a combination of the two [10].

As mentioned above, beneath the target transition in GS-SA the suppression covers all transitions from the ladder states to the entirety of the manifold below, and is thus effective for all possible decay pathways. By contrast, processes linking ladder states to higher energy off-ladder states in the manifold above are not necessarily suppressed: these transitions can potentially have a frequency larger than the cut-off, meaning optical excitation to the manifold above remains possible (see Fig. 2.6 and Fig. 2.9 for an example of such a transition). If such an excitation occurs, then rapid phonon relaxation takes the system down to the bottom of the new manifold, from where optical relaxation is suppressed, but excitation is once more still possible. This 'free' reinitialisation mechanism allows for the system to climb the ladder without any external reinitialisation.

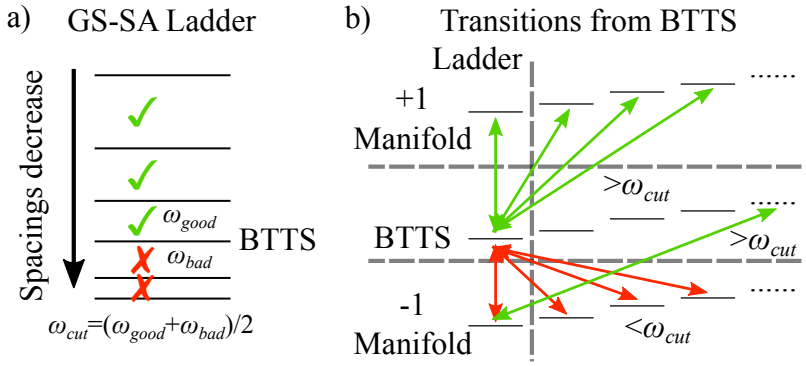

Figure 2.9: a) Demonstration of how the displaced ladder states in GS-SA are used to define a cut-off frequency, ω_{cut}. b) Schematic showing how our choice of ω_{cut} will cover all potential optical relaxation frequencies from BTTS, while still keeping relaxation pathways. An example 'free reinitialisation' pathway is also included. For clarity, energy separations between the different states in this image are not to scale: intra-band spacings have been scaled up with respect to interband spacings.

The effectiveness of this free reinitialisation depends on the strength of the suppression. As we conservatively do not assume perfect suppression of undesired modes, we also implement an active reinitialisation process to push the system back

up the ladder towards the target transition. We initially model this process in an idealised fashion, as incoherent pumping into the BTTS with rate γ_r from all ladder states below the BTTS. We call this 'ladder climbing' reinitialisation. Alternative active reinitialisation mechanisms are discussed later. It should be noted that active reinitialisation solutions have an energetic cost associated with them, which must be accounted for when benchmarking power output. The important parameter when looking for evidence of superabsorption is growth in the net power produced per absorber. By combining suppression as well as active or passive reinitialisation GS-SA systems can achieve a significant steady-state population in the BTTS.

To model the power output, we introduce a central trap that is equidistant from all absorbers, analogous to a photosynthetic reaction centre [75, 74]. Following the quantum heat engine model [17, 69, 85], the trap is modelled as a 2LS with energy $\omega_t = \omega_{\text{good}}$. The energy conversion process is represented by the incoherent decay of the trap to the ground state at rate γ_t. The decay of a single 2LS can qualitatively capture the behaviour of extraction via exciton transfer down a chain of sites in a tight-binding model [86, 87]. By defining the steady-state population of the trap's excited and ground states as $\langle\rho_\alpha\rangle_{SS}$ and $\langle\rho_\beta\rangle_{SS}$, respectively, we assign a hypothetical current and voltage [69, 85]

$$I = e\gamma_t \langle\rho_\alpha\rangle_{SS} \ , \tag{2.5}$$

$$eV = \omega_t + k_B T_{\text{vib}} \ln\left(\frac{\langle\rho_\alpha\rangle_{SS}}{\langle\rho_\beta\rangle_{SS}}\right) , \tag{2.6}$$

where k_B is Boltzmann's constant and $T_{\text{vib}} = 300$ K is the phonon environment temperature. The second term in the voltage expression ensures thermodynamic consistency. It should be noted that when quantifying input power for reinitialisation schemes which rely on eigenstates rather than site basis states, the correction term is dropped. This is a conservative choice, causing us to overestimate power input costs. This decision is made because this quantum heat engine formalism was derived to treat a 2LS as a trap, where the two steady state values in the argument of the logarithm sum to one. The populations of the initial and final state in a process moving population between eigenstates will not sum to one, and for this reason we drop the term. The choice of γ_t can optimise the current, and by extension the power output. For all our results γ_t is tuned to maximise the net power output.

We solve for the steady-state of our system using the Bloch-Redfield approach outlined in Chapter 1. This is appropriate for weakly-coupled environments, but strongly coupled vibrational environments in the polaron frame [56] will also be discussed later. We assume a free-space optical spectral density, aside from the suppression due to the photonic bandgap, and assume radiative equilibrium with the Sun $T_{\text{opt}} = 5800$ K [88, 19]. The phonon processes are based on an Ohmic room-temperature bath, with typical rates exceeding optical ones by three orders of

magnitude. Finally an idealised incoherent extraction dissipator, the rate of which (γ_x) roughly matches phonon timescales, relaxes the ring from the 'top-of-the-target-transition-state' (TTTS) to the BTTS while exciting the trap. A sketch of this extraction mechanism is presented in Fig. 2.10a, Alternative extraction mechanisms are discussed later.

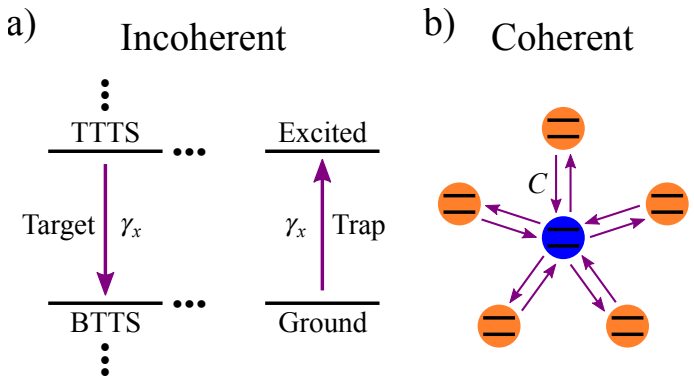

Figure 2.10: Sketches of the two extraction mechanisms we consider. a) Idealised incoherent extraction which targets the eigenstates of the ring while exciting the trap at rate γ_x. b) Coherent extraction achieved by coupling the trap to each of the ring sites with hopping strength $\mathcal{C}$. This method allows population to move from the trap back to the ring.

The overall master equation governing the dynamics of our ring antenna plus trap is ($\hbar = 1$)

$$\frac{d}{dt}\rho_S = -i[\hat{H}_S, \rho_S] + \mathcal{D}_{\text{opt}} + \mathcal{D}_{\text{vib}} + \mathcal{D}_x + \mathcal{D}_r + \mathcal{D}_t \ , \tag{2.7}$$

where $\hat{H}_S$ includes both the ring and the trap, and the dissipators are for the optical, vibrational, extraction, and trap decay processes, respectively. The steady state is found by calculating the eigenstates of the associated Liouvillian using the approach outlined in Chapter 1.

2.3 Results

2.3.1 GS Results

The first study we perform is on the interplay of our external mechanisms for influencing the system, namely suppression strength and active reinitialisation. The influence of varying these two parameters is seen in the top two panels of Fig. 2.11, which respectively show the net power produced and the fraction of expended input vs output power, both for the case of a pentamer. With poor suppression the system easily leaks down from the BTTS, potentially even resulting in a negative

overall power balance (white region) under faster reinitialisation. In an intermediate suppression regime, active reinitialisation becomes worthwhile, meaning faster reinitialisation improves performance further. We can see from Fig. 2.11b that the low fraction of power output that is needed to be reinvested as active reinitialisation indicates net power is not at risk of being easily overcome, even if the energetic cost for active reinitialisation proves to be somewhat more than we have assumed. Finally, for strong optical suppression the guide-slide effect successfully produces substantial net power, even in the absence of active reinitialisation, see Fig. 2.11d. This panel shows that larger rings require a higher degree of suppression to fully passively self-reinitialise. Conversely, Fig. 2.11c demonstrates that for a fixed degree of optical suppression (99%) in rings larger than $N = 3$, additional active reinitialisation will lead to a substantial increase of output power.

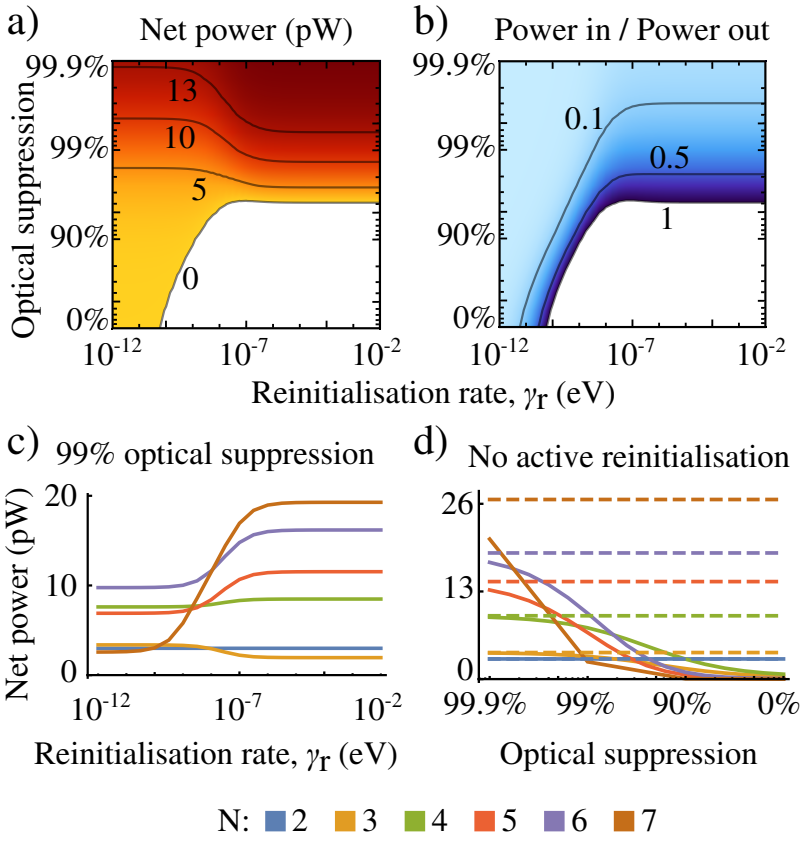

Figure 2.11: a) Net power produced by a pentamer as a function of decay suppression and reinitialisation rate. b) Ratio of the power in against the power out across the same parameter scan. c) A cross-section at 99% optical suppression for varying N. d) How different suppression strengths affect net power production without active reinitialisation. Dashed lines denote 100% suppression.

We now look specifically for the hallmark of superabsorption, namely a superlinear scaling of the net power produced with N, to align with the superlinear growth of the optical rate seen in Fig. 2.7. This superlinear growth of the net power with N

is confirmed by Fig. 2.12, which also gives a breakdown of input vs output power. We see that beyond $N > 3$, there is an increasing trend of GS-SA enabling quantum-enhanced photocell performance.

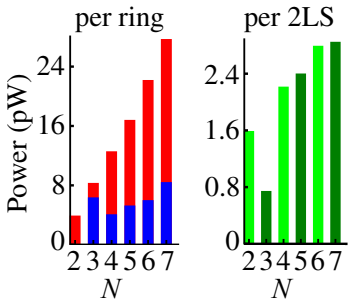

Figure 2.12: Output (red) and input (blue) power for different system sizes with 99% suppression of undesired optical modes, and superlinear growth of net power per site (green).

It is noteworthy that in Fig. 2.11c that the dimer does not require any active reinitialisation, and the trimer performs worse under active reinitialisation. The cost of active reinitialisation in the trimer does not make up for the increase in performance from the limited degree of collective enhancement of a small trimer system. Whilst larger rings clearly benefit from active reinitialisation at 99% suppression, it is interesting that free reinitialisation also works reasonably well for climbing up to two manifolds (i.e. up to the BTTS of a hexamer). The heptamer results show that larger systems rely on a higher degree of suppression for passive reinitialisation to be viable.

We now limit ourselves to a quadmer, and consider the effect of different phonon bath temperatures on the performance. For this scan we allow the dipole orientations to be optimised for each point on the parameter scan. In Fig. 2.13 we demonstrate how the power output varies over a full angular scan for a quadmer run with other 2LS parameters set to default. We see the default GS-SA position ($\theta_{\text{eq}} = \frac{\pi}{2}$ and $\theta_{\text{zen}} = \frac{\pi}{4}$) is close to the ideal angle, and also that the high performing region is large, a fact which proves beneficial when considering (angular) disorder.

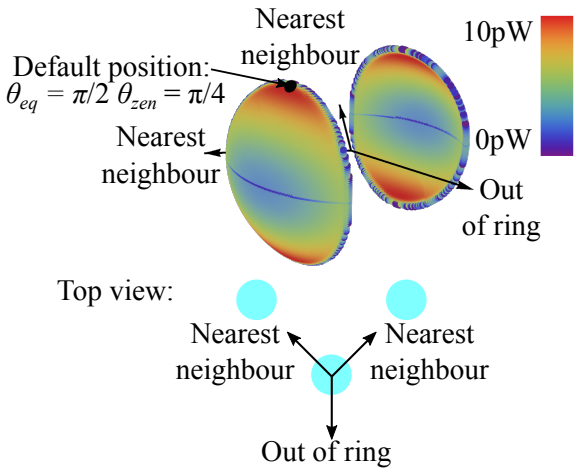

Figure 2.13: Representation of how net power production of a quadmer varies as different angles are chosen for the 2LSs. Only angles which produced a positive net power are plotted. A black spot is used to denote the default angular setup used in other runs. Also included is a plan view schematic to clarify the plotted axes arrows.

The main focus of this scan is to vary the 2LS spontaneous emission time τ_L and nearest neighbour separation $|\boldsymbol{r}_{i,i+1}|$, factors which affect the optical rates, and the Förster coupling strengths. The results in Fig. 2.14 show how the performance range expands at different vibrational temperatures. This is expected, as the performance of GS-SA can rely on either a cooler vibrational environment, or a larger separation of energies between eigenstates in the same manifold to encourage the 'guide-sliding' effect onto ladder states. This means cooler temperatures can work with smaller Förster coupling strengths.

To address the question of potential candidate systems suitable for exploring the GS-SA effect, we indicate regions and data-points referring to the properties of several state-of-the-art platforms for nanostructure photonics on Fig. 2.14. This demonstrates a broad range of credible building blocks for GS-SA antennae, though one would need to overcome the following design challenges:

- Assembling a ring of dipoles with adequate control over the orientation.
- Implementing a suitably engineered photonic bandgap.
- Setting up the ring with channels for both active reinitialisation and extraction [89, 90, 91].

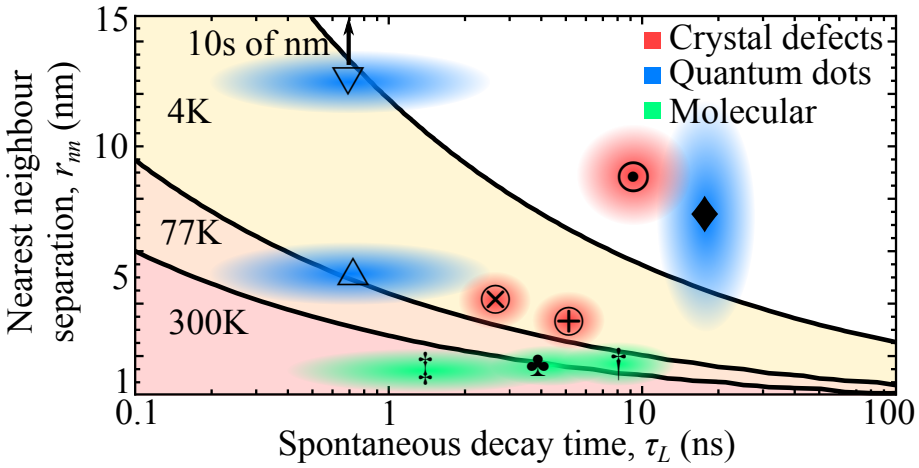

Figure 2.14: Map of where a quadmer produces positive net power as a function of 2LS natural lifetime and nearest neighbour separation. Regions typical of potential candidate systems are overlaid: Adjacent (▽) and stacked △) self-assembled InGaS quantum dots [92, 93]. ♢: Colloidal quantum dots [94, 95]. ⊙: Nitrogen vacancies [96, 97, 84]. ⊗: Silicon vacancy centres [98, 99, 100]. ⊕: Phosphorous defects [101, 102, 103]. ♣: BODIPY dye [104, 60, 105, 106]. †: Porphyrin rings [64, 65, 61]. ‡: Merocyanine dye (H-aggregate) and pseudoisocyanine chloride (J-aggregate) [107, 62, 108, 109]

2.3.2 Parallel breakdown

Having looked at the performance of the proposed GS-SA setup with our model, we now also look at the ||-SA setup proposed in Ref. [10]. Having all dipoles parallel maximises the total collective dipole of the system, so this would seem like the obvious choice for boosting the absorption of the system. However, as briefly mentioned in the main text, the inclusion of rapid phonon relaxation spoils the effect entirely. In the following, we show this breakdown explicitly.

Fig. 2.15 shows the net power produced by a quadmer and a pentamer for four different phonon rates:

1. $\kappa_{\text{vib}} = 0$, i.e. no phonons;
2. $\kappa_{\text{vib}} = 10^{-3} \times \gamma_{\text{opt}}(\omega_A)/\overline{\omega_{\text{vib}}}$ – 'slow';
3. $\kappa_{\text{vib}} = \gamma_{\text{opt}}(\omega_A)/\overline{\omega_{\text{vib}}}$ – 'match';
4. $\kappa_{\text{vib}} = 10^{3} \times \gamma_{\text{opt}}(\omega_A)/\overline{\omega_{\text{vib}}}$ – 'fast'.

Results for both ||-SA and GS-SA are shown with red and blue lines, respectively. Solid lines use fixed input parameters, while the dashed lines are averages from 100 trials with 1% disorder introduced over all input parameters (disorder discussed more later).

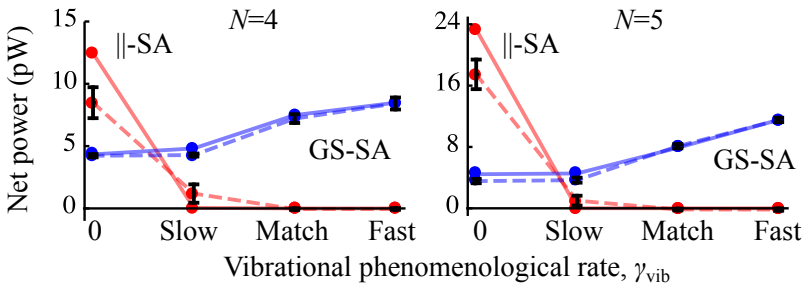

Figure 2.15: Plots showing the net power produced by a quadmer and pentamer in ||-SA and GS-SA setups for different phonon rates. Fixed parameters are plotted with the bold lines, while the dashed lines use 1% input disorder over 100 trials (standard deviation error bars included). ||-SA produces larger powers only for negligibly small phonon coupling. By contrast, the GS-SA setup always produces positive net power, and only increases in performance when phonons dominate over photon processes.

The ||-SA case produces large net power when there is either no phonon environment at all or if phonon rates are low compared to those of optical processes. In the presence of phonons, regardless of the phonon coupling strength, ||-SA requires some level of disorder, otherwise population gets trapped in off-ladder states from where it cannot decay. By not arriving back on the ladder it also will not be 'picked up' again by the ladder-climbing reinitialisation process. The steady-state of idealised ||-SA in the presence of any level of phonon coupling is therefore entirely on off-ladder states and away from enhanced optical transitions. For this reason the solid red line drops to zero as soon as phonons are included, whereas the dashed line (including a mild level of disorder) dips significantly but only hits zero once vibrational processes match optical ones. Both red lines tend towards zero for faster vibrational rates, demonstrating the breakdown of ||-SA. Overall, this suggests that ||-SA may be achievable for systems where no naturally prevalent phonon environment exists or where highly-tunable reinitialisation is available, for example in superconducting circuit-QED [110, 111].

Meanwhile for GS-SA the power produced increases in the presence of a dominant phonon environment, both in idealised and disordered cases. GS-SA also still performs adequately even in the absence of phonons or for low phonon rates, so unlike ||-SA it is not limited to a particular operating regime. However, as discussed earlier with Fig. 2.7, the tradeoff is that the maximum power produced from GS-SA cannot match that of ||-SA due to its reduced collective optical dipole. GS-SA's robustness to (and even benefitting from) vibrational relaxation suggests it may be suitable for implementation across a wide range of condensed-matter nanostructures, including in the solid state and for molecular systems.

2.4 Model extensions

We now carry out a variety of extensions on the reference GS-SA model described above and see how they affect the results.

2.4.1 Different phonon spectral densities

In the reference model, we chose an Ohmic phonon spectral density with no high-frequency cut-off. Since different systems will involve different phonon spectral densities, we shall here present results when substituting this with a superohmic spectral density including a cut-off.

We now consider phonon rates dependent on a spectral density in the usual way

$$\gamma(\omega) = J(\omega)\big(1 + n(\omega)\big) \ , \tag{2.8}$$

where $J(\omega)$ is the spectral density, which was previously $\omega\kappa_{\text{vib}}$ (see Chapter 1). There are a range of choices for $J(\omega)$ which could be picked depending on the choice of antenna. As long as the chosen phonon spectral density allows for relaxation processes to move population to the bottom of rungs, then the guide-slide concept still works. As an example we take the spectral density form

$$J(\omega) = \frac{\lambda\omega^3}{2\omega_{\text{crit}}^3} e^{-\frac{\omega}{\omega_{\text{crit}}}}, \tag{2.9}$$

where λ denotes the reorganisation energy, and ω_{crit} is the cut-off frequency. The bar charts in Fig. 2.16 show that the guide-slide states still display superabsorbing behaviour for two different choices of λ and ω_{crit} that are appropriate for molecular systems [112]. The right panel plots the spectral densities and a histogram of the different phonon transition frequencies in the quadmer and pentamer systems. The guide-slide effect requires some overlap of the spectral density with vibrational frequencies to allow phonon-assisted relaxation onto the ladder states. This criteria is met here and results in the net power output scaling super-linearly with ring size, as shown in left panel of Fig. 2.16.

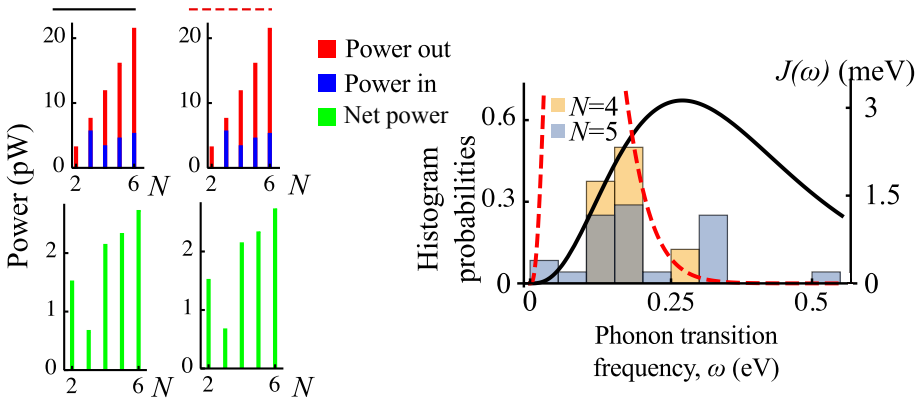

Figure 2.16: Left: power in, out, and net power per site found for various systems sizes using the the spectral density of Eq. (2.9). The parameters used in the spectral density were $\lambda = 5$ meV and $\omega_{\text{crit}} = 90$ meV (left column, black line) and $\lambda = 20$ meV and $\omega_{\text{crit}} = 25$ meV (right column, red dashed line). Right: spectral densities overlaid on normalised histograms of the different phonon transition frequencies arising with the quadmer (yellow) and pentamer (blue).

2.4.2 Alternative reinitialisation schemes

2.4.2.1 Lossy-ladder climbing

In this section we employ the 'lossy-ladder climbing' reinitialisation approach. Here, the system is over-excited in each of our reinitialisation steps, by pumping population to the top of the rung above, then allowing it to relax to the enhanced ladder state at the bottom of the rung. The repeated process of excitation followed by rapid vibrational relaxation is used to justify our assumption of 'one-way' excitation for the reinitialisation. This approach circumvents the possibility that the reinitialisation process could introduce a new loss process via detailed balance, with the tradeoff that over-excitation increases the energetic cost of reinitialising.

In Fig. 2.17 we show a comparison of this lossy reinitalisation method against the ladder-climbing one used in the reference model. We can see that the additional reinitialisation losses from using the lossy ladder climbing method do rescale the net power output, but importantly the qualitative behaviour is not affected and the superlinear scaling is maintained.

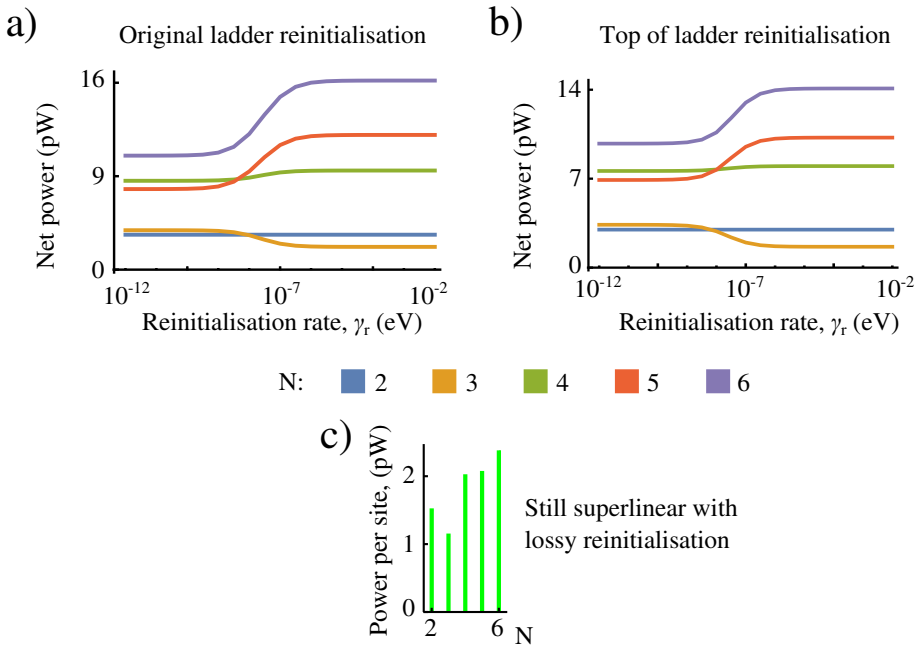

Figure 2.17: Comparison plot of the ladder-climbinging (a) and lossy ladder-climbing (b) reinitialisation methods, both at 99% suppression. Different system sizes are used, as well as varied reinitialisation rates. Power is slightly reduced, but the superlinear scaling of net power generation is unaffected by the change (c). Other parameters match those used in Fig. 3c of the main text.

2.4.2.2 Site-based

As another variation to the more idealised ladder-climbing reinitialisation, we also consider constant pumping across all of the absorbing sites on the ring. In this case, a rapid reinitialisation rate can lead to the system occupying the top half of the ladder, causing a waste of input power. For this method the reinitialisation rate needs to be optimised to produce the maximum net power output for each trial.

Fig. 2.18 qualitatively reproduces the features of Fig. 2.12 including the superlinear scaling of net power output. The inset in Fig. 2.18 shows the drop-off in net power when the system reinitialisation rate becomes too fast, causing substantial steady-state population above the BTTS). This figure also shows that the baseline performance from passive reinitialisation is only slightly improved upon by the introduction of stronger active reinitialisation before the active reinitialisation becomes a net cost that worsens performance.

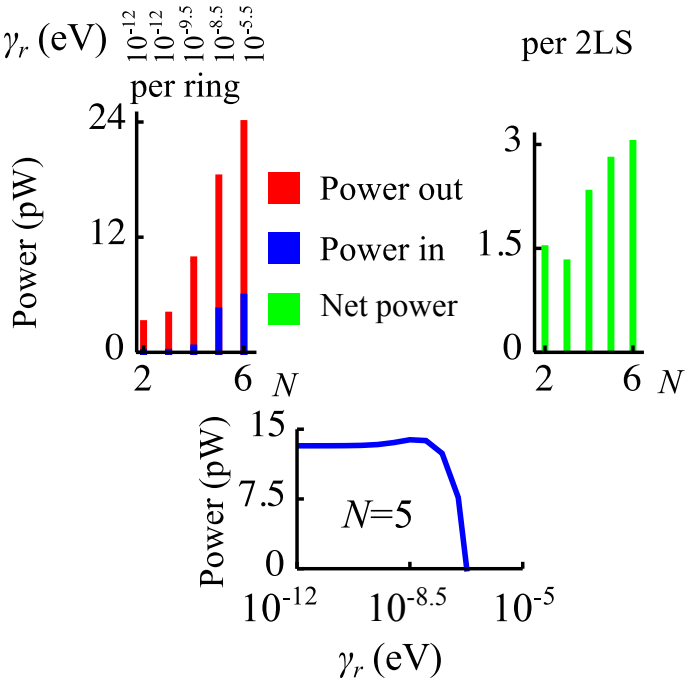

Figure 2.18: Power input, output, and net power per site for site-based reinitialisation. In each case the reinitialisation rate which provides the optimal net power is used, the reinitialisation rate, γ_r, is shown across the top. Superlinear behaviour is unaffected by this change. Other parameters are those of Fig. 2.12, except for an increased optical suppression of 99.9%. The lower panel shows how increasing the reinitialisation rate leads to an improvement in the power out for the pentamer before pushing the system into the top half of the ladder and wasting energy.

2.4.3 Coherent extraction

Our next extension is to consider site-based coherent coupling between the ring and the trap (Fig. 2.10b), rather than the idealised extraction which only links the eigenstates at the top and bottom of the target transition (Fig. 2.10a).

To implement coherent extraction, the extraction dissipator, $\mathcal{D}_x$, is removed from Eq. (2.7), and instead coupling terms for moving population between the ring sites and the trap are added to the system Hamiltonian. The strength of the coupling between the ring and the trap is $\mathcal{C}_x$. The trap site is kept degenerate with the target transition of the unperturbed ring eigenbasis (i.e. eigenbasis of the ring with no coupling to the trap, as is used in the reference model), $\omega_t = \omega_{\text{good}}$. The new system Hamiltonian for the ring and trap is therefore

$$\hat{H}_{\text{r\&t}} = \omega_A \sum_{i=1}^{N} \hat{\sigma}_i^z + \sum_{i,j=1}^{N} J_{i,j}(\boldsymbol{r}_{i,j})(\hat{\sigma}_i^+ \hat{\sigma}_j^- + \hat{\sigma}_i^- \hat{\sigma}_j^+) + \omega_t \hat{\sigma}_t^z + \sum_{i}^{N} \mathcal{C}_x(\hat{\sigma}_i^+ \hat{\sigma}_t^- + \hat{\sigma}_i^- \hat{\sigma}_t^+) \ . \tag{2.10}$$

Resonant coherent coupling between the target ring transition and the trap im-

plies that we no longer have unidirectional extraction and population can return from the trap back to the ring. However, for adequately fast trap decay rate, γ_t, this is suppressed and does not significantly affect the results.

For relatively small $\mathcal{C}_x$ compared to $J_{i,i+1}$, the presence of the trap in the Hamiltonian can be understood as a minor perturbation of the ring eigenstates, and the trap will only resonantly extract energy from the target transition, as adjacent ladder transitions are sufficiently far detuned due to the nearest neighbour couplings. However, as the coupling strength is increased, the trap and ring energy levels become hybridised. Strong coupling between the ring and trap could allow the trap to begin to also extract from other 'ladder transitions' . An important ramification of losing full extraction selectivity is that the trap can start to pull the the system down the ladder, undermining the suppression and reinitialisation processes keeping it operating around the target transition.

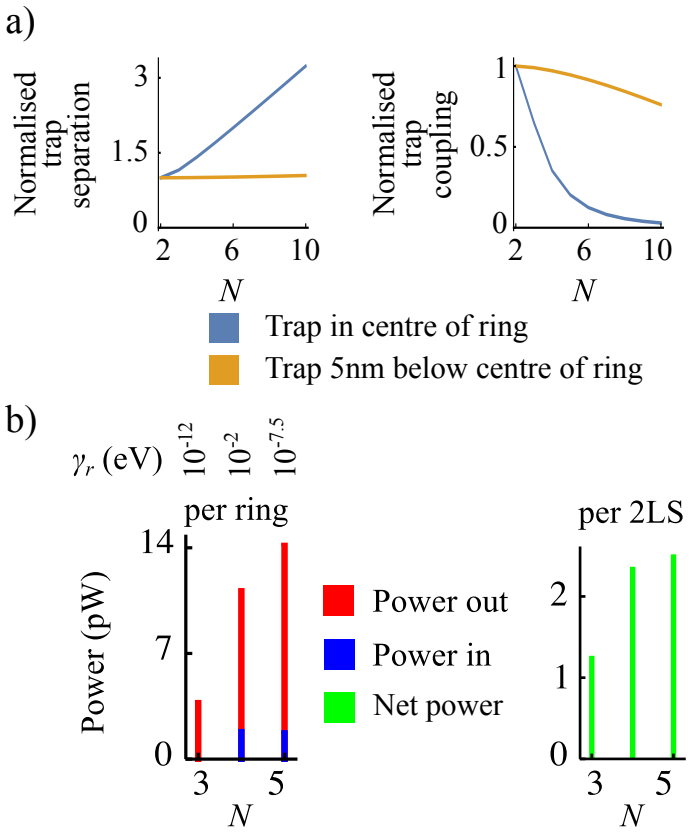

Figure 2.19: a) The N dependent scaling of ring-to-trap distance, and ring-to-trap coupling. (b) Power input, output, and net power per site for coherent extraction coupling to a trap in the centre of the ring. A slow base extraction rate of 10^{-4} eV is used to keep the extraction frequency selective, but is fast enough to overcome the drop off from the distant-dependent scaling. Super-linear behaviour similar to that seen in Fig. 2.12 with the reference model is observed in this case. For this plot different choices of γ_r were trialled, with selected rates as shown in the figure. The other parameters in these data runs are those used in Fig. 2.12 with the reference model, except for the optical suppression which is here increased to 99.9%.

If the coherent coupling was mediated by a dipole interaction in Eq. 2.1, then one would anticipate a reduction in the coupling strength as N is increased, assuming the nearest-neighbour separation along the ring is kept constant. Figure 2.19a demonstrates how separation and coupling scale with N. The coupling strength drop-off is seemingly dramatic if the trap is located in the centre of the ring, but positioning the trap out of the plane of the ring can reduce the drop-off. For these calculations, we define our extraction coupling, $\mathcal{C}_x$, as a base rate multiplied by the appropriate N dependent scaling factor.

In Fig. 2.19b we find that superabsorbing behaviour remains possible under coherent extraction with a trap positioned at the centre of the ring i.e. with stronger distance-dependent decay of $\mathcal{C}_x$. Here, the base extraction coupling strength of 10^{-4} eV is fast enough to extract most excitons absorbed by the system (for an

optical bath at the solar surface temperature), while not being so strong as to break the selectivity of extraction from the target transition. This graph stops with the pentamer due to the substantial computational demand of solving the master equation for the case of a hexamer. The power values are not quite as high as those observed when incoherent coupling is used, as is to be expected due to the extraction speed restriction which we applied. We note that calculations which did not include the distance-dependent scaling on the extraction coupling provided very similar results, implying the scaling is not introducing a new bottleneck to performance for the system sizes we consider.

Note that this plot also does not include the case of a dimer. The GS-SA setup has both dipoles pointing tangentially and inclined 45° out of the plane of the ring, leading to vanishing dipole-dipole coupling between the absorbers as the dipoles are then orthogonal. This means that for even arbitrarily weak extraction coupling the degenerate trap and dimer states are maximally hybridised, and the picture of viewing the trap as a perturbation to the ring antenna fails.

2.4.4 Coherent extraction and site-based reinitialisation

As a final variant of the model, we combine coherent extraction with site-based reinitialisation. In this setup, one needs to simultaneously ensure that the extraction coupling is not so strong that the trap starts extracting energy from other than the target transition, and that the reinitialisation proceeds fast enough to keep the system operating in the centre of the ladder, but not so fast as to push it further up.

The results of these data runs are shown in Fig. 2.20, and once more they display superabsorbing behaviour. Note that here we did not include an N-dependent scaling to the base extraction rate for these calculations, but our work in the dedicated coherent extraction section showed that for this base rate and system size there would be negligible effect on the performance by including the scaling.

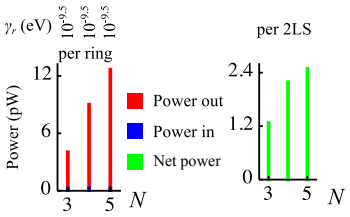

Figure 2.20: Power input, output, and net power per site for coherent extraction and site-based reinitialisation. In each case the reinitialisation rate γ_r was optimised to maximise net generated power. Notably, the small optimal values of γ_r mean that the input power is also rather small. The other parameters in these data runs are consistent with those used in Fig. 2.12 with the reference model, but again with optical suppression increased to 99.9%.

2.4.5 Non-radiative losses

To evaluate the robustness of GS-SA to non-radiative decay processes, which is particularly relevant for molecular systems, we add additional dissipator terms. For each of the N sites (indexed by i) we take an interaction matrix, $M_{\alpha,\mathrm{nr}} = \hat{\sigma}_i^-$ and form a Bloch-Redfield dissipator term following the steps laid out in Chapter 1. The rate for the non-radiative dissipators is defined as γ_{nr}.

In Fig. 2.21 we plot the optimised net power performance of GS-SA with $\mathcal{D}_{\mathrm{nr}}$ added to the calculation of the dynamics. The non-radiative rate, γ_{nr}, is expressed relative to the (bare) optical decay rate, γ_{opt}, which is defined as the rate associated with the 2LS spontaneous decay lifetime, τ_L. In Fig. 2.21a we first note that non-radiative loss has practically no effect on the dimer. For $N > 3$, we find that GS-SA performance is only marginally affected when the non-radiative loss rate is substantially smaller than the radiative one. However, once it exceeds roughly 10% we observe a rapid reduction in power output, which eventually erodes any net power output before parity is reached at 99% suppression. As shown in Fig. 2.21b this decline is less dramatic if stronger suppression is available. We conclude that GS-SA will perform best for systems in which non-radiative decay is not dominant. Whilst this may be a more challenging ask on the molecular platform, examples of bright organic dyes with small [113] or even negligible [114] non-radiative decay rates exist, whilst for others such as merocyanine the ratio between radiative and non-radiative decay can to an extent be controlled through the choice of solvent [115] and substrate [116].

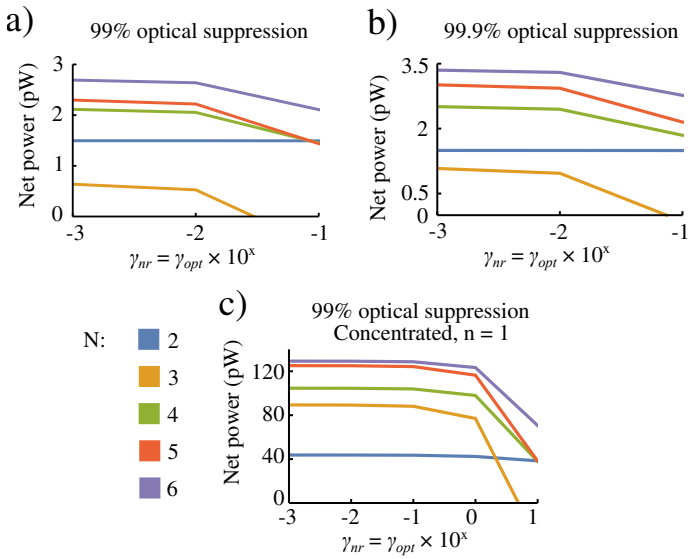

Figure 2.21: Comparison of how the increasing the non-radiative rate, γ_{nr} affects the net power performance of GS-SA with different system sizes. (a) and (b) All parameters match those used in Fig. 2.11c with the reference model, with ladder-climbing reinitialisation and two strengths of optical suppression being used. (c) the optical mode occupancy is set to 1, simulating concentrated sunlight and expanding the effective range to faster non-radiative rates.

Furthermore, it is worth noting that the effect of dominant non-radiative decay on the GS-SA performance can be limited in others ways. For example, any modification that increases the effective 'cycle time' of the GS-SA process while the non-radiative rate remains unaltered will prove effective. This would allow the system to rapidly return to where is was before a non-ratiative decay event. This could be achieved by using a cavity in the Purcell regime to enhance the light-matter coupling, or simply by choosing brighter optical dipoles. Alternatively an improvement can be obtained by coupling the system to a concentrated sunlight environment. Several related publications have taken this approach, choosing an optical mode occupancy $n = 60000$ [17, 72]. For our purposes this is an unnecessarily strong concentration, leading a large distibution of population throughout the Hilbert space. and not concentrated on the central ladder states as desired. We see an adequate a performance improvement at $n = 1$ enabling GS-SA with γ_{nr} exceeding γ_{opt}, as is typical for many organic dyes, see Fig. 2.21c.

Finally, we note that non-radiative loss, being proportional to the number of excitations, scales linearly with system size, whereas the optical absorption rate and associated power output features superlinear scaling with the GS-SA approach. This suggests that larger rings will be more robust to non-radiative decay, and our calculations do indeed suggest that the trimer is worst and the hexamer least affected (see Fig. 2.21).

2.4.6 Polaron coupled model

The coupling to vibrational modes, particularly in molecular systems, can go beyond the regime of the weak-coupling approach we have used so far. As a result we also develop a model that allows us to analyse the GS-SA effect in the polaron frame. We generally follow the approach laid out in Ref. [56], extended to considering an identical, strongly coupled phonon bath for each site. The derivation for a similar multi-site polaron transformation will also be written out more completely in Chapter 3. The transformation from the lab frame to the polaron frame (labelled with a prime) is given by

$$\hat{H}' = e^{\hat{S}} \hat{H} e^{-\hat{S}} \ , \tag{2.11}$$

where

$$\hat{S} = \sum_{i=1}^{N} \hat{\sigma}_i^z \otimes \sum_q \frac{g_{i,q}}{\omega_q} \big(\hat{b}_{i,q}^\dagger - \hat{b}_{i,q}\big) \ . \tag{2.12}$$

As the flat spectral phonon density primarily used in the basic model leads to divergent expressions in this formalism, we limit ourselves to the structured spectral densities used above with Eq. 2.9, as the polaron transformation generally only woks with superohmic spectral densities. Transformation to the polaron frame causes a renormalisation of the system Hamiltonian which reduces the effective dipole-dipole coupling between absorbing 2LSs. Diagonalisation of the polaron frame ring Hamiltonian now produces a ladder of eigenstates with shifted energies due to renormalisation terms.

The dynamics of the system in the polaron frame is governed by

$$\frac{d}{dt}\rho_S' = -i[\hat{H}_S', \rho_S'] + \mathcal{D}'_{\text{opt}} + \mathcal{D}'_{\text{coup}} + \mathcal{D}'_x + \mathcal{D}'_r + \mathcal{D}_t \ , \tag{2.13}$$

where the effects of the vibrational bath have been absorbed into the polaron frame system Hamiltonian $\hat{H}_S'$, which includes renormalised dipole-dipole coupling terms. The transformation has removed the original exciton-phonon-interaction Hamiltonian, at the cost of introducing additional phonon-dependent dipole-dipole interaction terms with the phonon bath of the form

$$\sum_{i\neq j}^{N} J_{i,j}(\boldsymbol{r}_{i,j})\big((\hat{B}_{+,i}\hat{B}_{-,j} - B^2)\hat{\sigma}_i^+\hat{\sigma}_j^- + \hat{\sigma}_i^-\hat{\sigma}_j^+(\hat{B}_{-,i}\hat{B}_{+,j} - B^2)\big). \tag{2.14}$$

This will give rise to the phonon dissipator $\mathcal{D}'_{\text{coup}}$ above, which takes the place of $\mathcal{D}_{\text{vib}}$ from the weak-coupling framework. Here, the $\hat{B}_{\pm\alpha}$ have the form [56]

$$\hat{B}_{\pm\alpha} = \prod_q e^{\pm(\frac{g_{\alpha,q}}{\omega_q}\hat{b}_{q,\alpha}^\dagger - \frac{g_{\alpha,q}^*}{\omega_q}\hat{b}_{q,\alpha})} \ , \tag{2.15}$$

and their expectation value in the continuum limit is given by

$$\langle \hat{B}_{\pm,\alpha} \rangle \equiv B = e^{-\frac{1}{2}\int_0^\infty \mathrm{d}\omega \frac{J(\omega)}{\omega^2} \coth(\frac{\beta\omega}{2})} \tag{2.16}$$

where $\beta = (k_B T_{\mathrm{vib}})^{-1}$ is the inverse thermal energy of the vibrational bath. After diagonalising the polaron transformed system Hamiltonian we proceed to create the new polaron frame vibration dissipator in the usual way seen in Chapter 1 [66], obtaining:

$$\begin{aligned}\mathcal{D}'_{\mathrm{coup}} = \sum_{n,m} w_n w_m \Big(& A_m(\omega_m)\rho_S(t)A_n^\dagger(\omega_n)\Gamma_{nm}(\omega_m) \\ & + A_n(\omega_n)\rho_S(t)A_m^\dagger(\omega_m)\Gamma_{nm}^\dagger(\omega_m) - \rho_S(t)A_m^\dagger(\omega_m)A_n(\omega_n)\Gamma_{nm}^\dagger(\omega_m) \\ & - A_n^\dagger(\omega_n)A_m(\omega_m)\rho_S(t)\Gamma_{nm}(\omega_m)\Big) \ . \end{aligned} \tag{2.17}$$

As in the weak-coupling case, the weighting terms $w_{n,m}$ arise from the transformation to the diagonal basis but now they additionally include polaron frame renormalisation. The rates for each term come from the environment correlation correlation operator, $\Gamma_{nm}(\omega_m)$, of the pair of relevant environment terms in the interaction. Every possible pair will result in one of three outcomes depending on whether the paired terms are linked to the same 2LS and whether they are both a raising or lowering type, or a mix. The four possible combinations evaluate to

$$\begin{aligned} \langle \hat{B}_{\pm,\alpha}(s)\hat{B}_{\pm,\alpha}(0)\rangle_\alpha &= B^2 e^{-\phi(s)} \ , \\ \langle \hat{B}_{\mp,\alpha}(s)\hat{B}_{\pm,\alpha}(0)\rangle_\alpha &= B^2 e^{+\phi(s)} \ , \\ \langle \hat{B}_{\pm,\alpha}(s)\rangle_\alpha \langle \hat{B}_{\pm,\beta}(0)\rangle_\beta &= B^2 \ , \\ \langle \hat{B}_{\mp,\alpha}(s)\rangle_\alpha \langle \hat{B}_{\pm,\beta}(0)\rangle_\beta &= B^2 \ , \end{aligned} \tag{2.18}$$

where

$$\phi(s) = \int_0^\infty \mathrm{d}\omega \frac{J(\omega)}{\omega^2}(\cos(\omega s)\coth(\beta\omega/2) - i\sin(\omega s)) \ . \tag{2.19}$$

To form the new optical dissipator, $\mathcal{D}'_{\mathrm{opt}}$ we note that the form of the optical interaction becomes $\hat{B}_{+,i}\hat{\sigma}_+^i + \hat{B}_{-,i}\hat{\sigma}_-^i$, so that the vibrational dependency needs to be accounted for when creating a Bloch-Redfield dissipator. We find that

$$\begin{aligned}\mathcal{D}'_{\mathrm{opt}} = \sum_{n,m} \boldsymbol{d}_n \cdot \boldsymbol{d}_m P_{\mathrm{vib}} \Big(& A_m(\omega_m)\rho_S(t)A_n^\dagger(\omega_n)\Gamma_{nm}(\omega_m) \\ & + A_n(\omega_n)\rho_S(t)A_m^\dagger(\omega_m)\Gamma_{nm}^\dagger(\omega_m) - \rho_S(t)A_m^\dagger(\omega_m)A_n(\omega_n)\Gamma_{nm}^\dagger(\omega_m) \\ & - A_n^\dagger(\omega_n)A_m(\omega_m)\rho_S(t)\Gamma_{nm}(\omega_m)\Big) \ , \end{aligned} \tag{2.20}$$

has the same form as the weak-coupling counterpart, except for the the inclusion of the P_{vib} weightings. Due to the difference in timescales between the vibrational

and optical processes, the effects of the two can be separated when calculating the rates [56, 117]. The calculation of $\Gamma_{nm}(\omega_m)$ is the same as was used in Chapter 1, though naturally it is now carried out between ladder states in the polaron frame. The value of P_{vib} varies depending on which two terms are involved: if both are for the same system and are a mixed combination or raising and lowering operators then $P_{\text{vib}} = 1$ or for equal operators $P_{\text{vib}} = B^4$; alternatively if they belong to different systems then regardless of operator combination $P_{\text{vib}} = B^2$.

The trap Hilbert space (tensored to the polaron frame ring) comes with a decay dissipator which is unaffected by the polaron frame, however, the trap energy, ω_t, is different as it is now tuned to the desired polaron frame ladder transition. An incoherent extraction process, like the one used in the main text, transfers population from the desired polaron frame ladder states to the excited state of the trap. The dissipator for the reinitialisation processes, $\mathcal{D}'_r$, uses the ladder-climbing approach described above, but now the ladder states are in the polaron frame, and as such have a slightly different energies.

As a consequence of moving to the polaron frame, collective optical effects are invariably reduced. This is due to the inclusion of the vibrationally dependent P_{vib} terms in the photon rates, and is consistent with recent results looking at a strongly-coupled dimer [117]. This somewhat reduces the 'brightness' of ladder states as well as the associated 'darkness' of certain off-ladder states, and as such we expect this will be detrimental to superabsorbing performance of the system.

Using our two phonon spectral densities we examined room temperature systems with 99% suppression of undesired optical modes. Due to computational constraints the maximal system size we investigated was a hexamer. In Fig. 2.22 we show the full power output data for the two cases, whilst also including results for each spectral density at cooler temperature, with stronger suppression of optical modes, and a reduced absorber lifetime of 2 ns, which provides a slightly stronger optical dipoles. The parameters for all the runs are summarised in Tab. 2.1.

Panel	Lifetime	$\lambda, \omega_{\text{crit}}$ (meV)	Suppression	Phonon temp	Superlinear to
a	2.5 ns	5,90	99%	300 K	6
b	2.5 ns	20,25	99%	300 K	2
c	2 ns	5,90	99.9%	77 K	6
d	2 ns	20,25	99.9%	77 K	4

Table 2.1: Parameters used for polaron transformed GS-SA model.

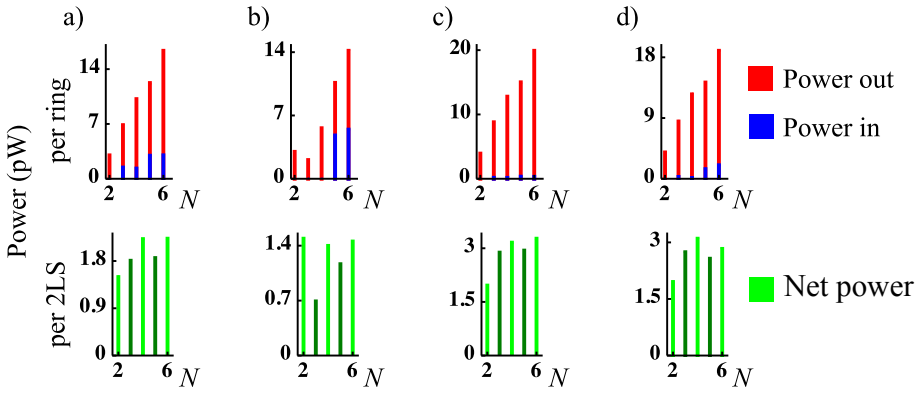

Figure 2.22: Power input, output, and net power per site for polaron transformed GS-SA model with two different spectral densities using both the parameters used with the reference model previously as as well as more favourable ones summarised in Tab. 2.1. The reinitialisation rate, γ_r, was optimised for net power production for each system size was used. Other parameters used in the calculations are consistent with those used to produce the results in Fig. 2.12 with the reference model.

We observe that the polaron transformation noticeably affects net power output of our antennae. Encouragingly, for weaker vibrational coupling ($\lambda = 5, \omega_{\text{crit}} = 20$ meV) the highest performing system was the hexamer, and there is a narrow superlinear trend when separately considering even and odd subspaces (but with the pentamer actually lying lower than the quadmer). By contrast, for the more strongly coupled vibrational environment, there was no advantage in adding more sites to a dimer based on the net power produced per site. The net power for the system did increase however in both cases as sites were added. This result contrasts with recently published results on the performance of collective light-harvesting systems in Ref. [118] which considered extraction tuned to the lowest rung of the excitation ladder (as opposed to the centre as we do here). In that work there was an optimal N beyond which the total power output decreases. With the more favourable conditions from the lower two lines of Tab. 2.1, the more strongly coupled $\lambda = 20$ meV case performed optimally with a quadmer, while the superlinear trends in the odd and even subspaces increased in the $\lambda = 5$ meV case.

In summary, in three of the four cases considered there was at least some superlinear collective advantage to be gained from adding more sites, and in all cases the total power produced per ring monotonically increased with N between trimer and hexamer, the largest studied system. Note that we did not vary the positions and orientations of the absorbers, as a full parameter scan would have been too computationally demanding, but such an investigation could have lead to a further optimisation of the results. Ideally, for intermediate vibrational coupling strengths one would adopt a Silbey-Harris variational polaron transformation approach rather than the full-blown polaron transformation. Previous variational studies have ex-

amined a single system [119], or multiple systems, but in both cases were limited to the single excitation subspace [120].

2.4.7 Disorder

Finally we investigate the robustness of the GS-SA model when disorder is introduced. We look at how randomising the 2LS parameters affects the guide-slide effect by applying a normal distribution to relevant input variables: the 2LS energy splitting ω_A, optical natural lifetime τ_L, the x, y, z components of the dipole positions $\boldsymbol{r}_i$, and the dipole orientation of each 2LS via θ_{eq} and θ_{zen}. In an individual trial, all of these parameters are drawn from a normal distribution centred around the means given in Tab. 2.3.

We have performed two types of disorder calculations:

- Simulations based on the full dynamic model, calculating the net power output of a disordered GS-SA (and ||-SA) photocell, the results of which are shown in Fig. 2.15.

- Analysing disorder in our candidate ring antennae with skewed dipoles with respect to the three criteria enabling GS-SA.

The former results have already been discussed, so in the following we focus on the second approach.

To address property 1 of the GS-SA conditions, Fig. 2.23 shows the level structure of the skewed ring antennae under the influence of different amounts of disorder. The lowest energy in each excitation manifold, i.e. the ladder rungs, are represented by black lines, whilst all other levels in the same excitation manifold are displayed in red (for clarity offset to the right). The overall ground and fully excited states are manifolds with only a single level and thus have no associated 'red boxes'. As before, the spacing between manifolds is not to scale.

The left panel shows how disorder causes a spreading of the black lines and red boxes. Keeping the ground state energy fixed, this spread amplifies in higher excited states. A key requirement for GS-SA is that the system will always be rapidly directed to the lowest energy (ladder) state in each excitation manifold, requiring a sufficiently steep energy gradient, with steps larger than thermal energy to prevent phonon absorption. Encouragingly, there remains a clear vertical separation between black and red subset for 1% disorder, but seemingly the lines begin to overlap for 5% disorder, which appears to undermine property 1. However, overlaying the entire ensemble is misleading in this regard: in the right panel of Fig. 2.23 we pin together the ladder states for each excitation manifold. Pinning the ladder states in this manner shows the criterion can be met individually for each member of the ensemble of trials. Meeting criteria 1 simultaneously across a disordered ensemble may be more difficult, but as shown in the next section ω_{good} and ω_{bad} remain

separated so that targeted suppression and extraction remain feasible. This shows that the separation between black lines and red boxes survives for larger amounts of disorder. The black dashed line is elevated by 25 meV above the BTTS, so gives an indication of how likely thermal excitation away from the ladder state is at room temperature. Only a small subset of the 10% disorder trials are prone to having the desired 'guide-sliding' interfered with by thermal excitation, and in these cases a colder ambient temperature would resolve this problem. We conclude that even under substantial 10% disorder our candidate for GS-SA continues to meet criterion 1.

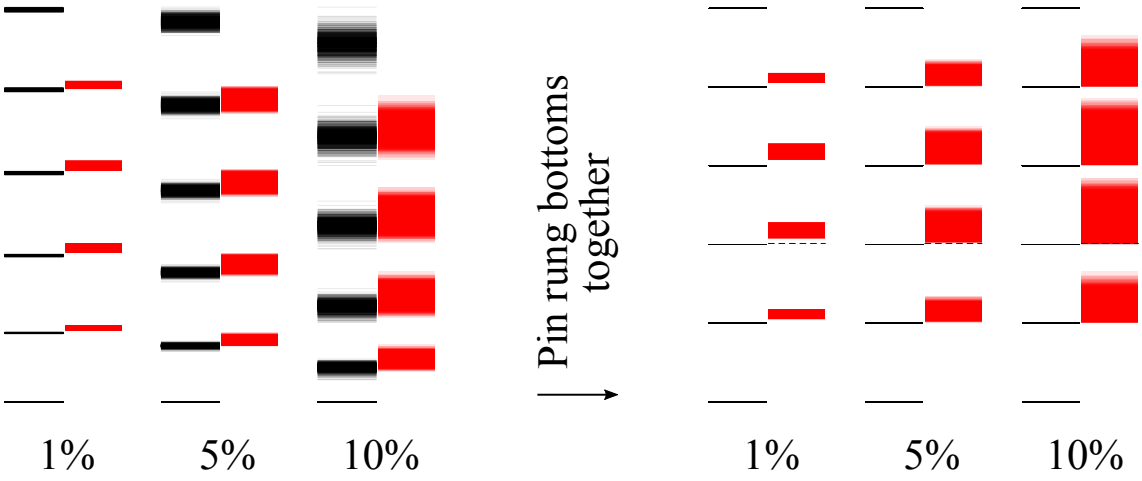

Figure 2.23: Level structure of a pentamer with 1%, 5% and 10% input disorder averaged over 1 000 trials. The top and bottom excitation manifolds are represented by single black lines, while the other manifolds feature single black lines for their lowest energy states, and a red box covering the energy range of the remaining states in the manifold. The spacing between manifolds is not to scale with the inter-manifold spacing. On the left, one sees the increased effect of disorder in higher up manifolds, due to the zero energy rung being the same position in all of the trials. To counteract this, on the right we pin together the black lines in each manifold, making the surviving separation between these and the red boxes more apparent. The dashed black line demonstrates the energetic step which could be overcome by room temperature thermal excitation.

Figure 2.7 includes disorder calculations regarding the dipole strength of the optical transitions covering the target transition in GS-SA. This involves summing the transition strengths of the transitions from BTTS to any state in the rung above the BTTS . Under the guide-slide mechanism any off-ladder population will rapidly relax back onto the ladder and be available for extraction from the TTTS. Figure 2.7 considers the total useful transition strengths for different system sizes. For $N = 2, \ldots, 7$, we averaged over 10 000 trials, while 1 000, 500, and 50 trials were

averaged to respectively give the data points for the octamer, nonamer, and decamer. For that figure all systems parameters are drawn from a normal distribution with 5% standard deviation.

In Fig. 2.24 we focus on case of a pentamer and extend the 5% disorder datapoint from Fig. 2.7a to 1% and 10% disorder. Based on 1 000 trials, the different coloured histograms show the total transition strengths normalised against the maximum transition strength which would be expected of a pentamer in the ideal non-interacting Dicke model. We see that it takes disorder across all 2LS parameters in excess of 5% to fully spoil the advantage of collective-enhancement. We have a further criterion for GS-SA to bear in mind: the most enhanced transition should indeed be the one linking the BTTS and TTTS: for 1%, 5% and 10% disorder, this is the case for, respectively, 100%, 99.7% and 76.8% of trials. Note that for small amounts of disorder a tiny fraction of trials exceeds the 'Fixed GS-SA' line. This is because the tilting angles of the dipoles are set at a fixed value and have not been optimised (unlike Fig. 2.14), so that introducing some randomness can occasionally beat the not disordered benchmark. Fig. 2.24 thus demonstrates that our candidate GS-SA system also displays robustness to substantial amounts of disorder with respect to criterion 2.

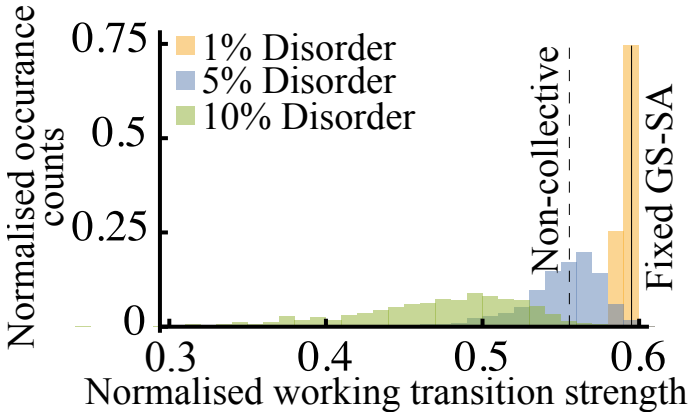

Figure 2.24: Histograms of the maximal absorption transition strength for a pentamer with 1%, 5% and 10% input disorder over 1 000 trials. The transition strengths are normalised against the unachievable transition strength found in the unperturbed Dicke model. Also indicated is the 'no disorder' GS-SA case (solid black line), and the value expected for independent absorbers which do not collectively absorb (dashed line). It is important to note from Fig. 2.7 that the gap between the solid line and dashed line increases with increasing N.

Property 3 for GS-SA, spectral selectivity, is required to suppress coupling to certain optical modes, while allowing access to those needed to the collectively enhanced target transition. To achieve this there needs to be sufficient separation between the desired target transition frequency, ω_{good}, and the largest undesirable

frequency that needs to be suppressed, ω_{bad}. Figure 2.25 shows the difference between these values for differing amounts of disorder. Whilst the distribution of this gap widens with increasing amounts of disorder, reassuringly, there is no overlap and typical differences are in excess of several 10's of meV, which provides the desired spectral selectivity and meets criterion 3.

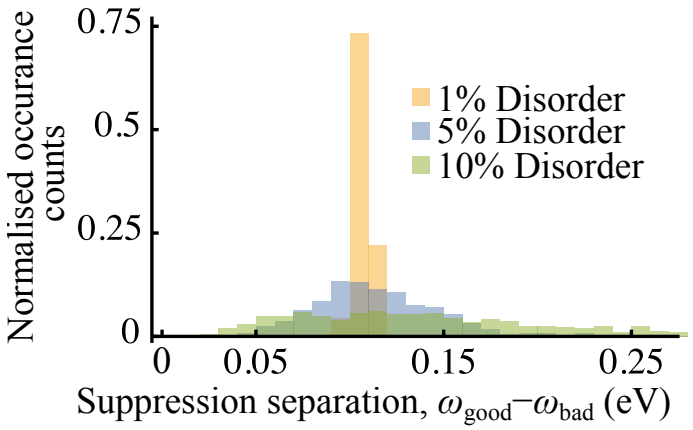

Figure 2.25: Histograms of the frequencies used to define the optical cutoff frequency, ω_{good} and ω_{bad}, for a pentamer with 1%, 5% and 10% input disorder over 1 000 trials. The optical cutoff frequency in GS-SA is defined as $\frac{\omega_{\text{good}}+\omega_{\text{bad}}}{2}$, so adequate separation is needed between these two frequencies.

In summary, this section has analysed the effect of up to 10% disorder for a pentamer ring antenna in the proposed GS-SA configuration. Criteria 1 and 3 have been found to be met for disorder up to 10%, and criterion 2 is robust to at least 5% disorder across all 2LS parameters simultaneously. Referring back to Fig. 2.15, we have observed that meeting the three criteria indeed translates into photocells with quantum-enhanced power generation performance. This confirms the potential of engineering and observing the GS-SA effect in real condensed-matter nanostructures.

2.5 Summary of all parameters

A complete set of model parameters used for the figures of the main text and this documents are printed in Tab. 2.5 and Tab. 2.3, respectively. Not shown is the trap decay rate γ_t as this is always numerically scanned over to find the value maximising the output power. For disorder calculations, the parameters are given by Gaussian distributions of varying widths (as stated in the relevant figures) around the indicated means.

Symbol	Fig. 2.11a & b	Fig. 2.11c	Fig. 2.11d	Fig. 2.7	Fig. 2.12	Fig. 2.14
N	5	Varied	Varied	Varied	Varied	4
ω_A	1.8 eV	1.8 eV	1.8 eV	1.8 eV	1.8 eV	1.8 eV
τ_L	2.5 ns	2.5 ns	2.5 ns	2.5 ns	2.5 ns	Varied
r_{nn}	1 nm	1 nm	1 nm	1 nm	1 nm	Varied
θ_{eq}	$\pi/2$	$\pi/2$	$\pi/2$	$\pi/2$	$\pi/2$	$\pi/2$
θ_{zen}	$\pi/4$	$\pi/4$	$\pi/4$	$\pi/4$	$\pi/4$	Optimised
s	Varied	99%	Varied	n/a	99%	99%
γ_x	10^{-2} eV	10^{-2} eV	10^{-2} eV	n/a	10^{-2} eV	10^{-2} eV
γ_r	Varied	Varied	n/a	n/a	10^{-2} eV	10^{-2} eV
T_{opt}	5800 K	5800 K	5800 K	5800 K	5800 K	5800 K
T_{vib}	300 K	300 K	300 K	300 K	300 K	300,77,4 K

Table 2.2: Full set of model parameters for main text figures of Ref. [23].

Symbol	Fig. 2.13	Fig. 2.15 GS	Fig. 2.15 ||	Fig. 2.23, 2.24 & 2.25
N	4	4, 5	4, 5	5
ω_A	1.8 eV	1.8 eV*	1.8 eV*	1.8 eV*
τ_L	2.5 ns	2.5 ns*	2.5 ns*	2.5 ns*
r_{nn}	1 nm	1 nm*	1 nm*	1 nm*
θ_{eq}	Varied	$\pi/2$*	$\pi/2$*	$\pi/2$*
θ_{zen}	Varied	$\pi/4$*	$\pi/2$*	$\pi/4$*
s	99%	99%	99.9%	n/a
γ_x	10^{-2} eV	10^{-2} eV	10^{-2} eV	n/a
γ_r	10^{-2} eV	10^{-2} eV	10^{-2} eV	n/a
T_{opt}	5800 K	5800 K	5800 K	n/a
T_{vib}	300 K	300 K	300 K	n/a

Table 2.3: Parameters for supplementary figures in Ref. [23]. Figures 2.16-2.22 used the same parameters as Fig. 2.12 with the basic model, other than the deviations mentioned in their respective captions. Asterisks denote values around which Gaussian distributions of varying widths were used in disorder trials.

2.6 Conclusions

We have proposed a set of conditions for a guide-slide superabsorber. With an adequate combination of passive reinitialisation induced by a photonic bandgap, and a means for actively reinitialising a system, one can design a collective system light-harvester, the performance of which scales superlinearly with system size. Starting

with the ||-SA configuration we examined how phonons in condensed matter nanostructure would prevent it from operating, and then altered the design, maintaining the biologically inspired ring foundation, and proposed a candidate GS-SA setup to study.

Such a system needs some degree of control over the dipole orientations when being synthesised, but we have shown the underlying concepts are robust to significant levels of disorder, with rapid vibrational relaxation always encouraging the system towards superabsorbing behaviour.

Encouragingly, experimental groups have shown they are able to synthesise molecular rings which display coherence effects [64, 121], and cooperative dipole behaviour, which we rely on, has been shown to remain attainable under strong dephasing [122]. The delocalised excitonic states of the kind necessary for the GS-SA proposal listed above may also occur in stacks of rings which self assemble into symmetric nanotubes [123, 124], opening the possibility for considering the effect in larger and more complex systems. Additionally if a superabsorbing system was designed using superconducting qubits then the limitations of vibrational interactions could be ignored, and one could study ||-SA without the risk of being pulled from the ladder states.

As well as the aforementioned experimental questions, a variational coupling model could be developed for modelling such systems, allowing the interface between the weak-coupling and polaron regimes to be studied. This work also opens some questions regarding using coherent coupling linking the antennae to the trap, and this will be looked at in greater detail in Chapter 3.

Chapter 3

Optical Ratcheting with Strongly-coupled Phonons and Coherent Extraction

3.1 Introduction

3.1.1 Existing work summary

Following on from the work looking at using collective optical effects in artificial light-harvesters in Chapter 2, this chapter focuses on designing light-harvesters which use 'optical ratcheting'. The motivation for this work therefore closely matches that of the work presented in Chapter 2. Ratcheting was originally proposed in a four site (quadmer), bio-inspired ring system [19], and further work applied an interpretation of the concept to both linear chains and rings of varying sizes while only considering the ground state and single excitation manifold [73]. This work makes a range of significant expansions upon the initial models. In particular it incorporates a much more realistic way of capturing the interaction with vibrations that is known to be strong in molecular systems. The outcomes of this work are currently being compiled in a manuscript for publication,

The guide-slide superabsorption proposal [23], which relied on rapid vibrational relaxation and coupling to a shared optical bath to achieve a 'greater than the sum of its parts' effect on the optical optical absorption rate (brightness), required additional processes like suppression of undesired optical modes and reinitialisation in order to operate. Optical ratcheting on the other hand, relies on rapid vibrational relaxation and coupling to a shared optical bath to achieve a reduced optical coupling [19]. The effect can rely just on the geometry of the absorbers as can be seen in the process maps for a quadmer in Fig. 3.1. This phenomenon relies on relaxation into vibrational modes after an absorption event to move the system to a state which is 'dark' with regards to optical emission. Previous photocell proposals had

suggested preventing optical recombination using either interference in multi-level systems [16, 69], or dark-state protection with multiple dipoles [17, 70, 18, 71, 72]. Ratcheting however, relies on moving the system to a state where darkness prevents optical relaxation of a single excitation, but from which further absorption is still possible, hence the name [19]. The time for extraction processes can act as a bottleneck in organic light harvesters [125, 25], and in such scenarios ratcheting was shown to be able to offer an improvement in light-harvesting performance [19].

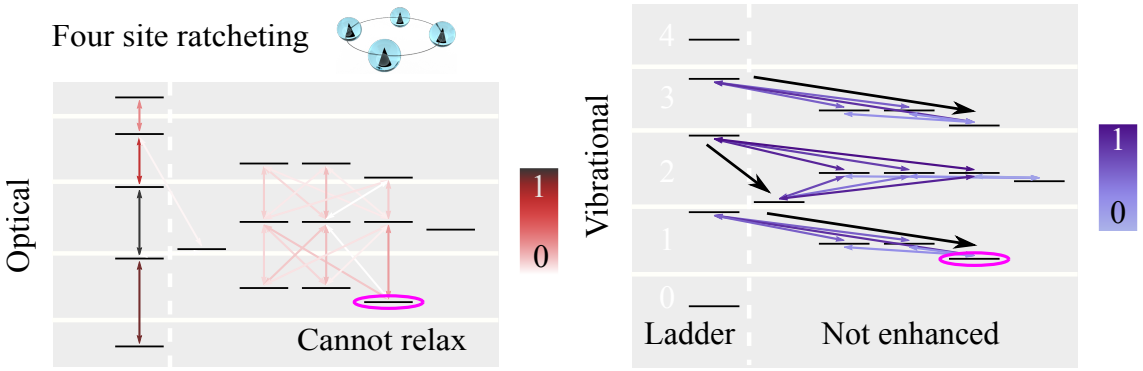

Figure 3.1: Process heatmap for optical (red) and vibrational (blue) transitions between eigenstates in a quadmer, as was considered in Ref. [19]. Normalised colour on the arrows denotes relative strengths. The states are organised in manifolds corresponding to the number of excitations in the system; the manifolds are visually separated by gaps in the background shading. Energy separations between manifolds and states within manifolds are not to scale. Black arrows show how vibrational relaxation pulls the system towards the circled pink state, from where it cannot emit a photon, but can absorb a second one.

3.1.2 New ideas summary

For this Chapter, we develop a more rigorous approach to investigating optical ratcheting. Building on the model used in Chapter 2, we develop an N site model, which allows us to benchmark the performance of ratcheting ($N > 2$) against a purely dark alternative ($N = 2$). We expand the model to consider strongly coupled phonons, and also introduce a trap site as an additional dipole, coupling it to the system with the dipole-dipole coupling determined by its optical brightness and position in 3D space relative to the absorbing ring. The use of a polaron transformation also means we will investigate structured phonon spectral densities, as the previous Ohmic coupling cannot be used with the polaron transformation approach.

Building on our approach, we look at the effect of scaling N, investigate the robustness against exciton-exciton annihilation, and explore the efficiency of exciton extraction when modelled as a physical process rather than phenomenologically.

3.2 Weakly-coupled incoherent extraction model

3.2.1 Model

3.2.1.1 Ring setup

The model starts with the same underlying components of the model used in Chapter 2. A ring of N identical absorbers are modelled as two level systems (2LSs) with energy splitting ω_A and spontaneous decay lifetime τ_L, with nearest neighbour separation $\boldsymbol{r}_{nn}$. The dipole moments are all directed perpendicular to the plane of the ring, as is the case in the ||-SA setup from Chapter 2, and shown in Fig. 3.1, and the magnitude of the dipole is given by $|\boldsymbol{d}| = \sqrt{3\pi\epsilon_0\tau_L^{-1}c^3/\omega_A^3}$ [80, 81]. The Hamiltonian for the ring is written as

$$\hat{H}_{\text{ring}} = \omega_A \sum_{i=1}^{N} \hat{\sigma}_i^z + \sum_{i,j=1}^{N} J_{i,j}(\boldsymbol{r}_{i,j})(\hat{\sigma}_i^+\hat{\sigma}_j^- + \hat{\sigma}_i^-\hat{\sigma}_j^+) \ , \tag{3.1}$$

where the Förster dipole-dipole coupling terms are given by [78, 79, 66]

$$J_{i,j}(\boldsymbol{r}_{i,j}) = \frac{1}{4\pi\epsilon_0|\boldsymbol{r}_{i,j}|^3}\left(\boldsymbol{d}_i\cdot\boldsymbol{d}_j - \frac{3(\boldsymbol{r}_{i,j}\cdot\boldsymbol{d}_i)(\boldsymbol{r}_{i,j}\cdot\boldsymbol{d}_j)}{|\boldsymbol{r}_{i,j}|^2}\right) . \tag{3.2}$$

The addition of non-nearest neighbour couplings is another extension beyond the work in Ref. [19].

3.2.1.2 Optical and vibrational environments

The small ring can collectively couple to a shared optical bath, using a multi-site quantum optical interaction Hamiltonian [66]

$$\hat{H}_{I,\text{opt}} = \sum_{i=1}^{N} \boldsymbol{d}_i\hat{\sigma}_i^x \otimes \sum_k f_k(\hat{a}_k + \hat{a}_k^\dagger) \ , \tag{3.3}$$

where f_k and $\hat{a}_k^{(\dagger)}$ are, respectively, the coupling strength and annihilation (creation) operator for the optical mode k. The vibrational behaviour in the system is modelled with local vibrational baths which are generically coupled to each 2LS with a spin-boson type coupling [68]:

$$\hat{H}_{I,\text{vib}} = \sum_{i=1}^{N} \hat{\sigma}_i^z \otimes \sum_q g_{i,q}(\hat{b}_{i,q} + \hat{b}_{i,q}^\dagger) \ , \tag{3.4}$$

where $g_{i,q}$ and $\hat{b}_{i,q}^{(\dagger)}$ are, respectively, the coupling strength and annihilation (creation) operator for the phonon mode q for the bath associated with site i [66, 19]. From these interaction Hamiltonians Bloch-Redfield dissipators are formed following the

steps in Chapter 1.

3.2.1.3 Incoherent trap

We begin with incoherent extraction, as was used in Ref. [19], the 'coherent' trap is discussed later. For now the trap is treated as a 2LS with energy splitting ω_t. A constant incoherent decay of the trap at rate γ_t models the irreversible conversion and extraction of energy. As was the case in Chapter 2, a quantum heat engine approach is used to benchmark the power produced from our system [17, 69, 85]. By solving for the steady state using the approach outlined in Chapter 1 we can define current and voltage as

$$I = e\gamma_t \langle \rho_\alpha \rangle_{SS} \ , \tag{3.5}$$

$$eV = \omega_t + k_B T_{\text{vib}} \ln \left(\frac{\langle \rho_\alpha \rangle_{SS}}{\langle \rho_\beta \rangle_{SS}} \right) , \tag{3.6}$$

where $\langle \rho_\alpha \rangle_{SS}$ and $\langle \rho_\beta \rangle_{SS}$ are ,respectively, the excited and ground steady state populations for the trap, k_B is Boltzmann's constant and $T_{\text{vib}} = 300$ K is the phonon environment temperature.

Rather than idealised targeted eigenbasis extraction, as was used in Chapter 2, we instead use the site basis and couple a single absorber to the trap. We assign an extraction rate to this process, denoted as γ_x.

3.2.2 Results

3.2.2.1 Trap decay optimisation

The first calculation we perform is to look at how the behaviour of the quantum heat engine varies as the trap decay rate is varied. In Fig. 3.2 the results for a trimer ($N = 3$) are plotted. The current (top) and power (bottom) are plotted against both the trap decay rate (left) and resulting voltage (right). Different extraction rates (γ_x) are used, and the plots show that the performance saturates once the extraction dominates over any optical radiative relaxation. Similarly the current performance saturates once the trap decay rate also passes a certain threshold, namely the rate which allows an excitation to have been processed before the next one is being extracted form the ring. While the current does saturate, the presence of the second term in Eq. 3.6 means that there is still a peak in the power-voltage curve.

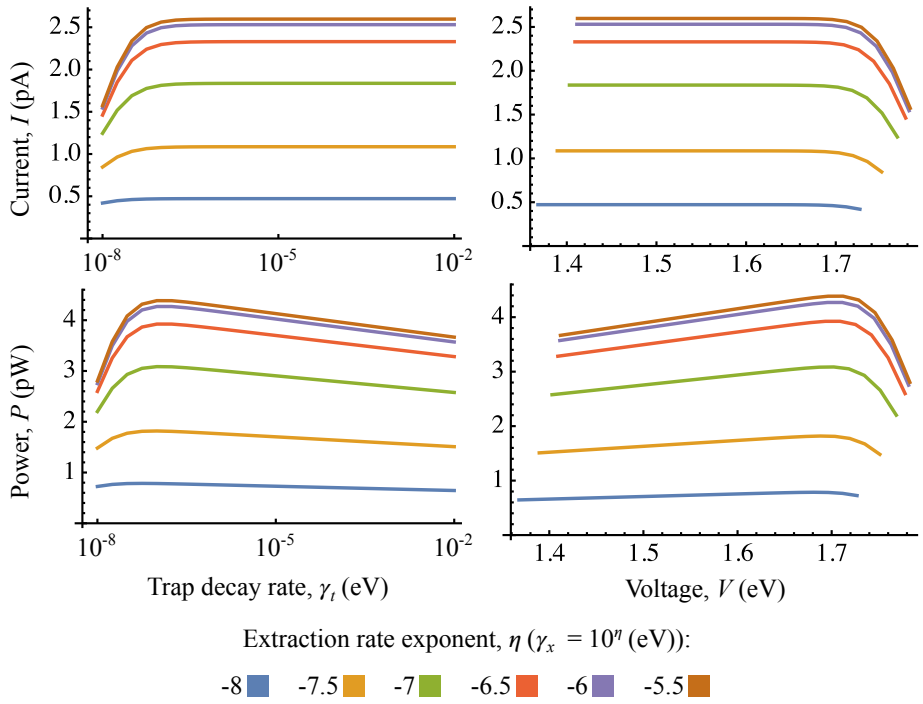

Figure 3.2: Steady state results for a trimer using both different extraction rates and trap decay rates to benchmark the current, voltage and power from the quantum heat engine.

3.2.2.2 N scaling

We now vary the size of the ring while plotting the P-V curve for both rapid and bottlenecked extraction rates. In the rapid extraction regime any excitation is rapidly extracted from the ring and moved to the trap, without the vibrational relaxation playing a major role. In Chapter 2 it was discussed that optical rates at the edges of the Dicke ladder are proportional to N (also known as single photon collective effects [5, 6]). With rapid extraction and trap decay one can take full advantage of the N proportionality, and this can be seen in the right hand panel of Fig. 3.3, where the power produced per site does not change. In the left hand panel the effect of ratcheting can be observed. The dimer, which can can take advantage of darkness but not ratcheting, is outperformed by the trimer, which can take advantage of ratcheting. The quadmer however, which was considered in the original ratcheting paper [19], drops down and does not perform as well as the trimer. The parameters for the results in this section are shown in Tab. 3.1.

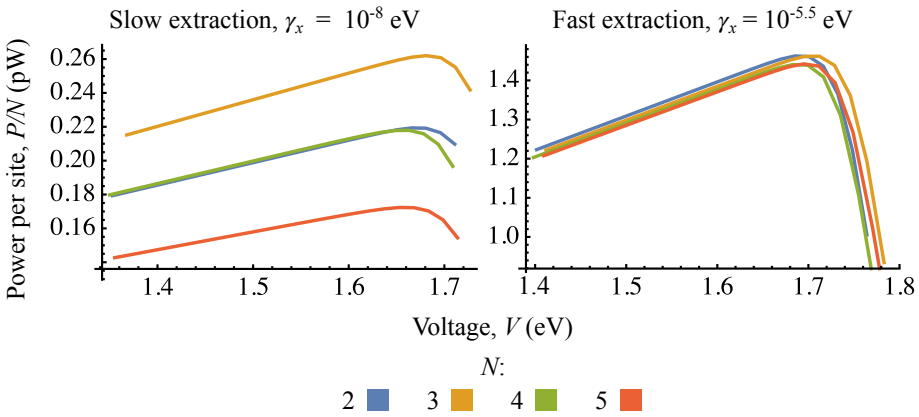

Figure 3.3: Plots comparing the power per site performance as the ring size is varied. For rapid extraction there is little difference as N changes, but for bottlenecked extraction one can see the effect of ratcheting. Plots of the total power per ring are included in Fig. 3.2.

N	ω_A	τ_L	r_{nn}	γ_x	γ_t	T_{opt}	T_{vib}
$2 \to 5$	1.8 eV	5 ns	2 nm	$10^{-8} \to 10^{-5.5}$ eV	$10^{-8} \to 10^{-2}$ eV	5800 K	300 K

Table 3.1: Parameters used for results in this section with the weakly-coupled, incoherent extraction model.

Having established the established the fundamental behaviour of optical ratcheting in this weakly-coupled model that uses incoherent extraction, we now investigate what occurs when we improve these elements.

3.3 Strongly-coupled phonons

3.3.1 Polaron-transformed model

In the following we carry out a multi-site polaron transformation for our model. This derivation follows the steps in Ref. [56], which only considered a single system. The result of this derivation was also used in Chapter 2.

3.3.1.1 Lab frame Hamiltonian

For an open quantum system we have a general Hamiltonian form

$$\hat{H} = \hat{H}_S + \hat{H}_I + \hat{H}_E \ , \tag{3.7}$$

respectively covering the system, interaction and environment, where only $\hat{H}_I$ terms have operators affecting both system and environment components of the combined

Hilbert space.

We define the system Hamiltonian with a different energy reference point compared to Eq. 3.1,

$$\hat{H}_S = \sum_i^N \omega_A \left|X_i\right\rangle \left\langle X_i\right| + \sum_{i\neq j}^N J_{i,j}(r_{i,j})\left(\hat{\sigma}_i^+\hat{\sigma}_j^- + \hat{\sigma}_i^-\hat{\sigma}_j^+\right) , \tag{3.8}$$

and the environment components as

$$\hat{H}_E = \sum_{i,k} \omega_{i,k} b_{i,k}^\dagger b_{i,k} + \sum_q \omega_q a_q^\dagger a_q , \tag{3.9}$$

respectively the individual phonon and shared photon contributions. Note that for the purpose of this derivation we use the outer product representation of the excited state, rather than a Pauli z spin matrix ($\sigma_z = \left|X\right\rangle \left\langle X\right| - \left|0\right\rangle \left\langle 0\right|$). This is just to make the cancelling of some terms more intuitive. The interactions are then taken to be

$$\hat{H}_I = \sum_i^N \left|X_i\right\rangle \left\langle X_i\right| \otimes \sum_k g_{i,k}\left(b_{i,k}^\dagger + b_{i,k}\right) + \sum_i^N \sigma_{x,i} \otimes \sum_q f_q\left(a_q^\dagger + a_q\right) . \tag{3.10}$$

3.3.1.2 Polaron transformation form

The transformation of the Hamiltonian to the polaron frame for a single site with only one vibrational bath to consider is given by

$$\hat{H}' = e^S \hat{H} e^{-S} , \tag{3.11}$$

where

$$S = \left|X\right\rangle \left\langle X\right| \otimes \sum_k \frac{g_k}{\omega_k}\left(b_k^\dagger - b_k\right) . \tag{3.12}$$

For multiple sites, one needs to implement a transformation for each strongly coupled vibrational bath:

$$\hat{H}' = e^{S_N} \ldots e^{S_2} e^{S_1} \hat{H} e^{-S_1} e^{-S_2} \ldots e^{-S_N} , \tag{3.13}$$

where

$$S_i = \left|X_i\right\rangle \left\langle X_i\right| \otimes \sum_k h_{i,k}\left(b_{i,k}^\dagger - b_{i,k}\right) , \tag{3.14}$$

in which

$$h_{i,k} = \frac{g_{i,k}}{\omega_{i,k}} . \tag{3.15}$$

This transformation now needs to be applied to each component of Eq. 3.7.

3.3.1.3 Transforming system Hamiltonian

The transformed system Hamiltonian is given by

$$\hat{H}'_S = e^{S_N} \dots e^{S_2} e^{S_1} \hat{H}_S e^{-S_1} e^{-S_2} \dots e^{-S_N} \ . \tag{3.16}$$

The diagonal contribution of the system Hamiltonian, $\sum_i^N \omega_A \left|X_i\right\rangle \left\langle X_i\right|$, is unaffected by the transformation, though they are renormalised by the transformation of another component. The coupling contribution, $\sum_{i\neq j}^N J_{i,j}(r_{i,j})\big(\hat{\sigma}_i^+\hat{\sigma}_j^- + \hat{\sigma}_i^-\hat{\sigma}_j^+\big)$, is affected by the transformation.

Can simplify this transformation by only considering $e^{S_k}\left|X_i\right\rangle\left\langle 0_j\right| e^{-S_k}$. There will only be an effect from the transformation if $k = i$. We know that

$$\begin{aligned} \left|X_k\right\rangle\left\langle X_k|X_i\right\rangle &= \delta_{i,k}\left|X_k\right\rangle \ , \\ \left|X_k\right\rangle\left\langle X_k|0_i\right\rangle &= 0 \ . \end{aligned} \tag{3.17}$$

We can combine this with the relationship $e^{\hat{A}}\left|\alpha\right\rangle = e^a\left|\alpha\right\rangle$, where $\hat{A}\left|\alpha\right\rangle = a\left|\alpha\right\rangle$. By separating the system and environment parts of the transformation, one can write $e^{S_k} = e^{\left|X_k\right\rangle\left\langle X_k\right|\kappa_k}$, and the transformed term will be given by

$$e^{S_i}\left|X_i\right\rangle\left\langle 0_j\right| e^{-S_i} = e^{\kappa_i}\left|X_i\right\rangle\left\langle 0_j\right| \ , \tag{3.18}$$

similarly

$$e^{S_j}\left|0_i\right\rangle\left\langle X_j\right| e^{-S_j} = \left|0_i\right\rangle\left\langle X_j\right| e^{-\kappa_j} \ . \tag{3.19}$$

The effect of all the transformations acting on the couplings will therefore be

$$\begin{aligned} &\prod_{k=N}^{1} e^{S_k} \sum_{i\neq j}^{N} J_{i,j}(r_{i,j})\big(\hat{\sigma}_i^+\hat{\sigma}_j^- + \hat{\sigma}_i^-\hat{\sigma}_j^+\big) \prod_{k=1}^{N} e^{-S_k} \\ &\qquad = \sum_{i\neq j}^{N} J_{i,j}(r_{i,j})\big(e^{\kappa_i}\hat{\sigma}_i^+\hat{\sigma}_j^- e^{-\kappa_j} + e^{-\kappa_i}\hat{\sigma}_i^-\hat{\sigma}_j^+ e^{\kappa_j}\big) \ . \end{aligned} \tag{3.20}$$

It should be noted that this can be rewritten in terms of displacement operators:

$$e^{\pm\kappa_\alpha} = B_{\pm\alpha} = \prod_k D\big(\pm h_{k,\alpha}\big) \ , \tag{3.21}$$

where

$$D\big(h_{k,\alpha}\big) = e^{h_{k,\alpha}b_{k,\alpha}^\dagger - h_{k,\alpha}^* b_{k,\alpha}} \ . \tag{3.22}$$

The system Hamiltonian in the polaron frame is therefore

$$\hat{H}'_S = \sum_i^N \omega_A \left|X_i\right\rangle\left\langle X_i\right| + \sum_{i\neq j}^{N} J_{i,j}(r_{i,j})\big(B_{+,i}B_{-,j}\hat{\sigma}_i^+\hat{\sigma}_j^- + \hat{\sigma}_i^-\hat{\sigma}_j^+ B_{-,i}B_{+,j}\big) \ . \tag{3.23}$$

3.3.1.4 Transforming environment Hamiltonian terms

The optical bath will be completely unaffected by the transformation to the polaron frame.

Phonon baths will not be affected by transformations which are not for that specific bath. The creation and annihilation operator in the bath can be separately transformed to have the form

$$\begin{aligned} b_{i,k}^{\dagger} &\to b_{i,k}^{\dagger} - |X_i\rangle \langle X_i| \, h_{i,k} \ , \\ b_{i,k} &\to b_{i,k} - |X_i\rangle \langle X_i| \, h_{i,k} \ . \end{aligned} \tag{3.24}$$

One can therefore write the transformed phonon baths as

$$\begin{aligned} \sum_{i,k} \omega_{i,k} b_{i,k}^{\dagger} b_{i,k} &\to \sum_{i,k} \omega_{i,k} \big(b_{i,k}^{\dagger} - |X_i\rangle \langle X_i| \, h_{i,k} \big) \big(b_{i,k} - |X_i\rangle \langle X_i| \, h_{i,k} \big) \ , \\ &\to \sum_{i,k} \omega_{i,k} \Big(b_{i,k}^{\dagger} b_{i,k} - |X_i\rangle \langle X_i| \, \big(h_{i,k} b_{i,k}^{\dagger} + h_{i,k} b_{i,k} - h_{i,k}^2 \big) \Big) \ . \end{aligned} \tag{3.25}$$

3.3.1.5 Transforming interaction Hamiltonian terms

Each phonon interaction will only be affected by its own polaron transformation. Each interaction is broken down into $|X_i\rangle \langle X_i| \, b_{i,k}^{(\dagger)}$ terms and then transformed individually. The transformation gives

$$\sum_{i}^{N} |X_i\rangle \langle X_i| \otimes \sum_{k} g_{i,k} \big(b_{i,k}^{\dagger} + b_{i,k} \big) \to \sum_{i}^{N} |X_i\rangle \langle X_i| \otimes \sum_{k} g_{i,k} \big(b_{i,k}^{\dagger} + b_{i,k} - 2h_{i,k} \big) \ . \tag{3.26}$$

The final step is to transform the optical interaction into the polaron frame. The transformation will commute with the optical operators, having no effect on the optical environment contribution, and therefore only changing the $\sigma_{x,i}$ contributions.

$$\begin{aligned} \sum_{i}^{N} \sigma_{x,i} \otimes \sum_{q} f_q \big(a_q^{\dagger} + a_q \big) &= \sum_{i}^{N} \big(\, |X_i\rangle \langle 0_i| + |0_i\rangle \langle X_i| \, \big) \otimes \sum_{q} f_q \big(a_q^{\dagger} + a_q \big) \ , \\ &\to \sum_{i}^{N} \big(B_{+,i} \, |X_i\rangle \langle 0_i| + |0_i\rangle \langle X_i| \, B_{-,i} \big) \otimes \sum_{q} f_q \big(a_q^{\dagger} + a_q \big) \ . \end{aligned} \tag{3.27}$$

3.3.1.6 Fully-transformed Hamiltonian

The new system Hamiltonian in the polaron frame can now be written as

$$\hat{H}_S' = \sum_{i}^{N} \omega_A' \, |X_i\rangle \langle X_i| + \sum_{i \neq j}^{N} J_{i,j}(r_{i,j}) \big(B_{+,i} B_{-,j} \hat{\sigma}_i^{+} \hat{\sigma}_j^{-} + \hat{\sigma}_i^{-} \hat{\sigma}_j^{+} B_{-,i} B_{+,j} \big) \ , \tag{3.28}$$

where

$$\omega'_A = \omega_A - \sum_k \frac{g_k^2}{\omega_k} \ . \tag{3.29}$$

In the continuum limit

$$\sum_k \frac{g_k^2}{\omega_k} \to \int_0^\infty \mathrm{d}\omega \frac{J(\omega)}{\omega} = \lambda \ , \tag{3.30}$$

where λ is the renormalisation energy and $J(\omega)$ is the phonon spectral density.

3.3.1.7 $B_{\pm,\alpha}$ terms in couplings

The transformed dipole-dipole couplings have the form

$$\sum_{i\neq j}^{N} J_{i,j}(r_{i,j})\big(B_{+,i}B_{-,j}\hat{\sigma}_i^+\hat{\sigma}_j^- + \hat{\sigma}_i^-\hat{\sigma}_j^+B_{-,i}B_{+,j}\big) \ , \tag{3.31}$$

which can be written as

$$\begin{aligned}\sum_{i\neq j}^{N} J_{i,j}(r_{i,j})\big(B^2\hat{\sigma}_i^+\hat{\sigma}_j^- + \hat{\sigma}_i^-\hat{\sigma}_j^+B^2\big) \\ + \sum_{i\neq j}^{N} J_{i,j}(r_{i,j})\big((B_{+,i}B_{-,j} - B^2)\hat{\sigma}_i^+\hat{\sigma}_j^- + \hat{\sigma}_i^-\hat{\sigma}_j^+(B_{-,i}B_{+,j} - B^2)\big) \ .\end{aligned} \tag{3.32}$$

Here $B_\alpha = \langle B_{\pm,\alpha}\rangle = B$, since all the phonon baths are identical.

The B term can be evaluated by starting with time evolution operator:

$$U(t) = e^{iH_It} = e^{-S}e^{iH'_It}e^S \ , \tag{3.33}$$

which is transformed back to the lab frame from the polaron frame. Alternatively one can write

$$U(t) = |0\rangle\langle 0| U_E(t) + e^{-i\omega'_At}|X\rangle\langle X| B_-U_E(t)B_+ \ , \tag{3.34}$$

where

$$U_E(t) = e^{-iH_Et} \ . \tag{3.35}$$

If we consider the single site independent boson model of Ref. [56], we have the density matrix

$$\begin{aligned}\rho_S(t) = \rho_{00}|0\rangle\langle 0| + \rho_{XX}|X\rangle\langle X| \\ + \rho_{0X}|0\rangle\langle X| e^{i\omega'_At}C^*_{-+}(t) \\ + \rho_{X0}|X\rangle\langle 0| e^{-i\omega'_At}C_{-+}(t) \ ,\end{aligned} \tag{3.36}$$

where $\rho_{ij} = \langle i| \rho_S(0) |j\rangle$ for $i, j = \{0, X\}$, and the correlation functions are

$$C_{-+}(t) = \mathrm{Tr}_E[\tilde{B}_-(t) B_+ \rho_E(0)] \ , \tag{3.37}$$

where $\tilde{B}_\pm(t) = U_E^\dagger(t) B_\pm U_E(t)$. For a thermal environment the correlation function becomes $C_{-+}(t) = \langle B \rangle^2 e^{\phi(t)}$. In this case

$$\phi(t) = \int_0^\infty \mathrm{d}\omega \frac{J_{ph}(\omega)}{\omega^2} (\cos(\omega t) \coth(\beta\omega/2) - i \sin(\omega t)) \ , \tag{3.38}$$

is the phonon propagator, and

$$\begin{aligned} B &= \langle B \rangle \ , \\ &= \mathrm{Tr}_E\big(B_\pm \rho_E(0)\big) \ , \\ &= e^{-\frac{1}{2}\int_0^\infty \mathrm{d}\omega \frac{J(\omega)}{\omega^2} \coth(\frac{\beta\omega}{2})} \ , \end{aligned} \tag{3.39}$$

which can be written as $\langle B \rangle = e^{-\frac{1}{2}\phi(0)}$.

Having undergone the derivation for the multi-site polaron transformed evolution, the process for solving it can be found in Chapter 2.

3.3.2 Results

3.3.2.1 Establishing consistent behaviour

The introduction of strongly coupled vibrational environments means that optical transitions which were previously totally dark will now allow optical processes, unless $B = 1$. This can potentially limit the performance of ratcheting, which relies on 'safely' storing an excitation for extraction whilst being able to absorb another one. As long as the relaxation process is still considerably less likely to occur than excitation then ratcheting is still achievable.

In Fig. 3.4 we plot the results for the same set of parameters that were used in Figs. 3.2 and 3.3. As a polaron transformation is used we need a structured spectral density, and we choose the one used in Chapter 2:

$$J(\omega) = \frac{\lambda \omega^3}{2\omega_{\mathrm{crit}}^3} e^{-\frac{\omega}{\omega_{\mathrm{crit}}}}, \tag{3.40}$$

where λ denotes the reorganisation energy, and ω_{crit} is the cut-off frequency [112]. The results in Fig. 3.4 use $\lambda = 5$ meV and $\omega_{\mathrm{crit}} = 90$ meV, and show similar behaviour to the weakly-coupled model, with the ratcheting trimer outperforming the dark dimer, but with performance still dropping for larger systems.

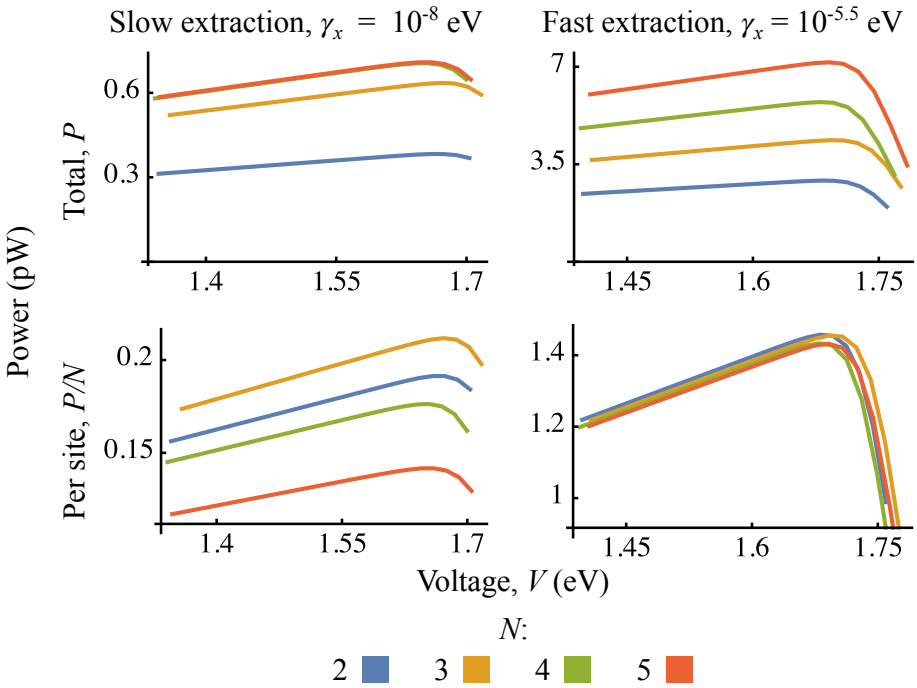

Figure 3.4: Plots comparing the total power and power per site performance using the strongly-coupled polaron model as the ring size is varied. The parameters used in the spectral density were $\lambda = 5$ meV and $\omega_{\text{crit}} = 90$ meV. For rapid extraction there is little difference as N changes, but for bottlenecked slow extraction one can see the effect of ratcheting.

In Fig. 3.5 we repeat the test using $\lambda = 20$ meV and $\omega_{\text{crit}} = 25$ meV. The power per site performance shows that the ratcheting behaviour stops occuring here, with the top performing system being the dimer. This is because the stronger coupling to the vibrational environment ends up having a stronger effect on the optical processes, preventing the rest state at the bottom of the single-excitation manifold from being completely dark. From hereon we will only consider the former phonon spectral density parameters ($\lambda = 5$ meV and $\omega_{\text{crit}} = 90$ meV) for results.

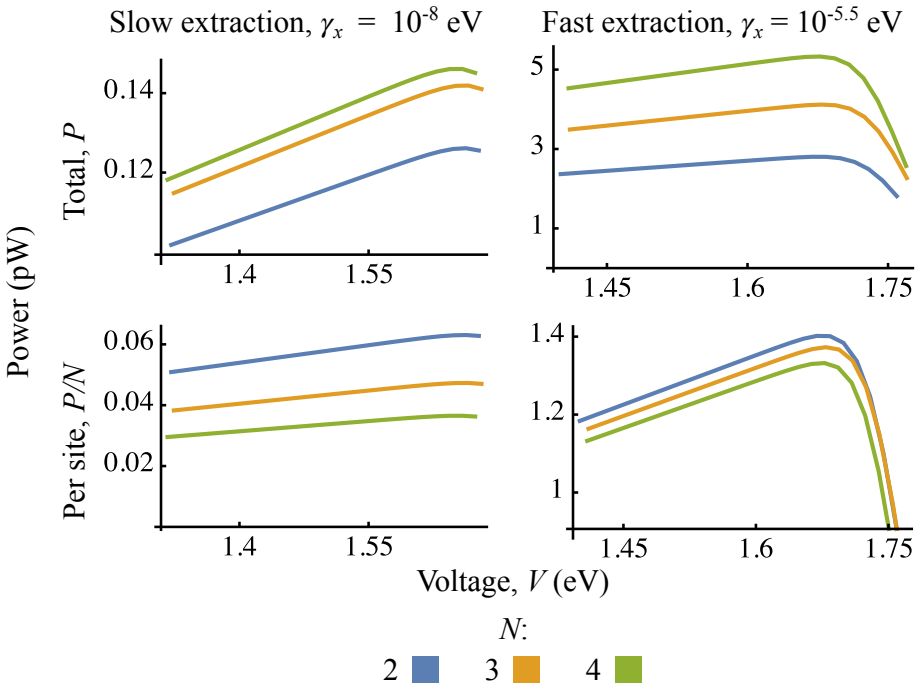

Figure 3.5: Plots comparing the total power and power per site performance using the strongly-coupled polaron model as the ring size is varied. The parameters used in the spectral density were $\lambda = 20$ meV and $\omega_{\text{crit}} = 25$ meV. For rapid extraction there is little difference as N changes, and with slow bottlenecked extraction one can see there is no benefit to increasing beyond a dimer.

3.3.2.2 Scaling extraction

We next consider scaling the extraction rate with the system size ($\gamma_x \to \gamma_x N$). This means a quadmer site ring extracts twice as fast as a dimer. This scenario effectively considers the idea that the more absorbers in are in the ring, the stronger the coupling to the trap should be. One can also consider the case where a trap has an upper limit on how much energy it can handle, and one wants to determine if it is more beneficial to connect it to a single system of absorbing antennae, or multiple smaller collective systems. The results in Fig. 3.6 show that once this change is made all measured larger systems can outperform the dimer on power produced per site. It should be noted that the scaling of the extraction is carried out on the extraction rate from a single site to the trap. One could alternative method to account for this scaling would be to have a dissipator from each site to the ring, instead however we will extend the idea further using coherent coupling later on.

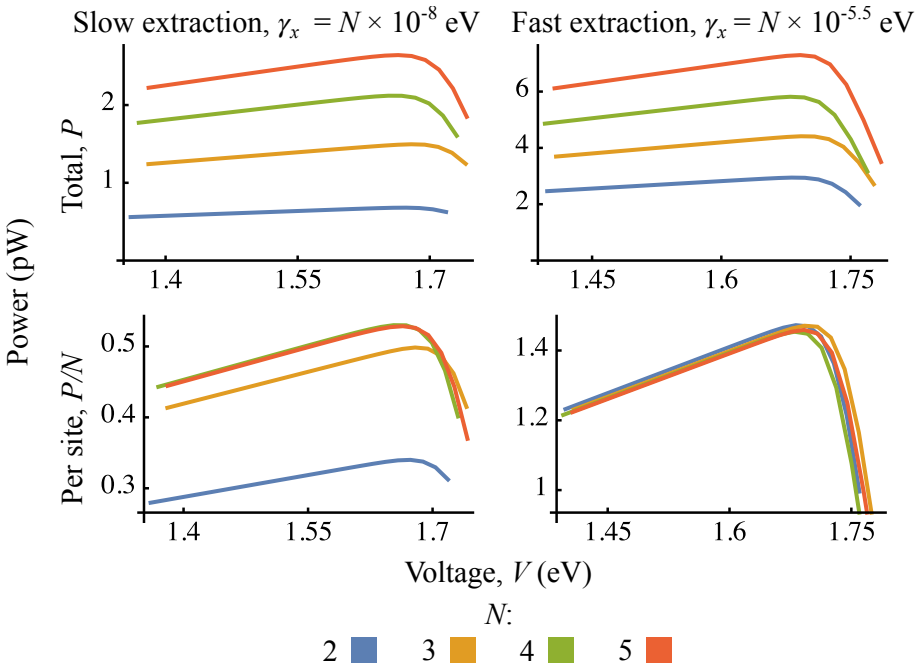

Figure 3.6: Plots comparing the total power and power per site performance using the strongly-coupled polaron model as the ring size is varied. The parameters used in the spectral density were $\lambda = 5$ meV and $\omega_{\text{crit}} = 90$ meV. The extraction rate is scaled with N. For rapid extraction there is little difference as N changes, but for bottlenecked extraction one can see the effect of ratcheting, as all systems outperform the dimer on 'per site' performance.

3.3.2.3 Varying sunlight concentration

Our photon bath is modelled such that the system is in equilibrium with a 5800 K bath. At this temperature and a transition frequency of 1.8 eV the mode occupation number is roughly 0.03. For realistic solar illumination the Sun would only take up a small component of the solid angle viewed by the system. Previous work looking specifically at dark state protection also considered the effect of the system under concentrated illumination, this was achieved by setting the thermal occupation number to a very large, constant value ($n = 60000$) (this is equivalent to photon bath at roughly 2×10^9 K). In light of this we introduced a photon concentration factor, α, which we applied to the rates such that excitation and relaxation rates respectively became

$$\begin{aligned} \gamma_{\text{opt,up}} &= \kappa_{\text{opt}} \omega^3 \alpha n(\omega) \ , \\ \gamma_{\text{opt,down}} &= \kappa_{\text{opt}} \omega^3 \big(1 + \alpha n(\omega)\big) \ , \end{aligned} \tag{3.41}$$

where α was varied from 10^{-4} to 10^8 to consider both of these extreme scenarios. With larger optical concentrations, we are interested in the ability for a large enough system with enough excitation manifolds to access a second tier of ratcheting, i.e. a

manifold beyond the single-excitation manifold where the lowest energy state is completely optically decoupled from the manifold below, but not above, allowing more excitations in the system to be stored for extraction.

In Fig 3.7 we plot the results from a using a scan from the minimum to maximum α. We use both a bottlenecked and rapid extraction speed, as well as both the fixed and N scaled versions. For each value α and extraction rate, a scan of trap decay rates is performed, and the power produced by the optimal rate is used. For each size system the power per site is plotted, and a logarithmic scale is used to clearly make out the behaviour both at large and small optical concentrations. One can see that with N-scaled extraction the power per site is the same for all systems for high solar concentrations. Under rapid extraction there is also no difference between the performance of different sized systems for lower concentrations. Under weak extraction the blue dimer line is always the poorest performing for low solar concentrations, but for $\alpha > 10$ the dimer is either equivalent to or better than larger systems.

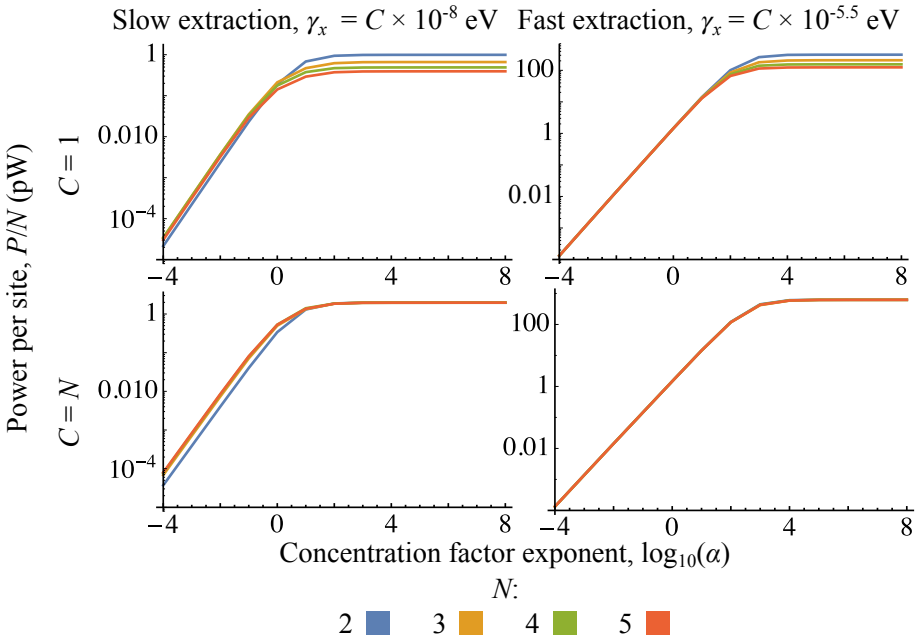

Figure 3.7: Plots comparing the power per site performance using the strongly-coupled polaron model as the ring size is varied and the photon concentration factor is changed. The parameters used in the spectral density were $\lambda = 5$ meV and $\omega_{\text{crit}} = 90$ meV. The extraction rate is scaled with N in the lower panels. For weak extraction the dimer is the lowest performing for lower values of α, suggesting ratcheting is giving an advantage to larger systems.

There is an important point to consider regarding extraction when α grows and relaxation processes lose dominance over excitation terms ($\gamma_{\text{opt,up}} \approx \gamma_{\text{opt,down}}$). In this case one cannot assume the population will gather at the bottom of the first excited manifold, instead population will become spread throughout the Hilbert

space. The incoherent extraction from a single site to a trap which is degenerate with the energy of the bottom state in the first excited manifold will end up extracting from a range of states in the energy basis, but realistically the extraction should be influenced by the overlap of the transition frequencies also. This is an area where a coherent extraction model could offer more information, as ω_t can be varied to find what is most effective under concentrated illumination. This model could then be used to answer further questions about the feasibility of higher level ratcheting.

3.3.2.4 Exciton-exciton annihilation

Our next consideration for the model is exciton-exciton annihilation (EEA) [118, 19]. Once there is more than one excitation in the ring there is the possibility that the two could interact and annihilate without being extracted. Since ratcheting is a multi-excitation phenomena, there is a risk that the performance could be impeded by such an effect.

To test this we introduce new one-way incoherent Lindblad dissipators. For the second excitation manifold and above, every state in a manifold is connected to the lowest energy state in the adjacent manifold below. The rate for these dissipators, γ_{EEA}, is set to vary from sub optical process rates ($\gamma_{EEA} = 10^{-2} \times \gamma_{\text{opt}}$), up to dominating phonon process rates ($\gamma_{EEA} = 10^{5} \times \gamma_{\text{opt}}$). It should be noted that while this approach is a good initial way to gauge the effectiveness of EEA, a more rigorous approach would scale the dissipative rates with the number of excitations in the system, i.e. two excitons are more likely to encounter each other triggering annihilation event when there are three in the system rather than when there are only two.

In Fig. 3.8 the results including these EEA dissipators are shown. The results without dissipators are displayed as faded dashed lines. While increasing the EEA rate can reduce the power per site for all systems larger than a dimer, it does not change the ordering of performance between the different system sizes. The decreases are also rather small, this is because ratcheting relies on mainly being in the single-excitation manifold, and only occasionally benefiting from occupying the second manifold. More noticeable shifts may come from including a dissipator for non-radiative processes, as was used in Chapter 2, which would allow for loss from the single-excitation manifold.

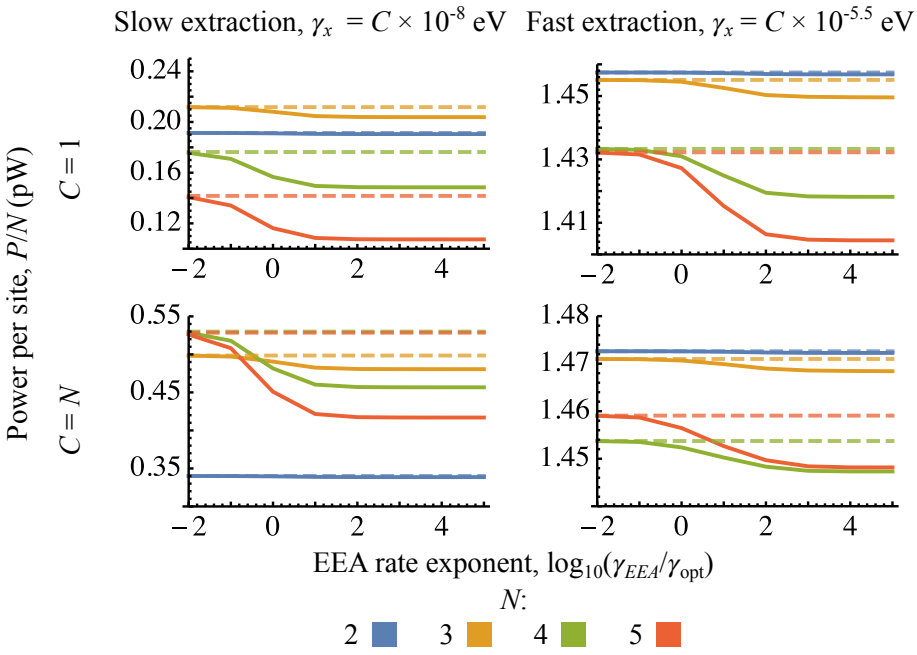

Figure 3.8: Plots comparing the power per site performance using the strongly-coupled polaron model as the ring size is varied and the EEA rate is varied. The parameters used in the spectral density were $\lambda = 5$ meV and $\omega_{\text{crit}} = 90$ meV. The extraction rate is scaled with N in the lower panels. The dashed lines show the value when the EEA dissipators are not included.

3.4 Coherent extraction model

3.4.1 Model – Coherently coupling a trap

3.4.1.1 Modelling the trap as an additional dipole

Having established that strong phonon coupling regimes exist that don't fundamentally change ratcheting behaviour, in the following we revert to the weak-coupling approximation for vibrations.

For our next extension we considered a more realistic treatment of the trap. In Chapter 2 one of the extensions was to consider a coherently coupled trap, though the coherent treatment in this project is more rigorous in the following ways:

- We now include the trap as an additional 2LS, modelled in 3-D space with position and dipole orientation which can be moved around the absorbing ring.

- We can assign the trap dipole both a unique energy splitting, ω_t, and decay lifetime, $\tau_{L,t}$, producing a dipole moment, $\boldsymbol{d}_t$, which alongside the position and orientation information is used to calculate dipole-dipole couplings to the absorbers in the ring with Eq. 3.2.

- We can also choose to include the trap as an additional optical dipole coupled to the shared bath, and also can couple it to another local vibrational bath.

In Chapter 2 the strength of the coherent coupling between the trap and the absorbers was assigned by looking for a strength which was not so strong that the system could not reach a steady state near the middle of the excitation ladder, where the optical transitions were most enhanced. The coupling was also small enough that the effect of the trap being included in the system Hamiltonian could be considered as a perturbation of the picture seen with incoherent extraction, upon which the choice of ω_t was made to be degenerate with the transition of interest in the unperturbed picture.

Finally, whilst the goal of the extraction in Chapter 2 was primarily concerned with absorbing as much of the absorption from the desired target transition as possible, for ratcheting there are additional concerns we can investigate with this more realistic approach to modelling the trap:

- Ratcheting and dark state behaviour are primarily concerned with improving performance when in a bottlenecked extraction regime, where population needs to be moved away from optically bright states.

- The extraction must therefore be targeted to primarily work on the dark states of the system.

For simplicity we alway choose $\boldsymbol{d}_t$ to be parallel with the dipole moments of the absorbing antennae of the ring, perpendicular to the plane of the ring. The symmetry of the ring allows us to place the trap on one of three principal axes (Fig. 3.9):

1. The axis through the centre of the ring and perpendicular to the plane of the ring.

2. The axis through the centre of the ring and through one absorber on the ring.

3. The axis through the centre of the ring and through the mid point between to neighbouring absorbers on the ring.

We define a trap separation, s_t, which is the distance from the trap to the closest absorber, and this is used to determine the position that the trap sits along one of these axes. By moving the trap further from the ring we can reduce the coupling strength and see how behaviour changes as we change from an aggressive to a bottlenecked extraction rate.

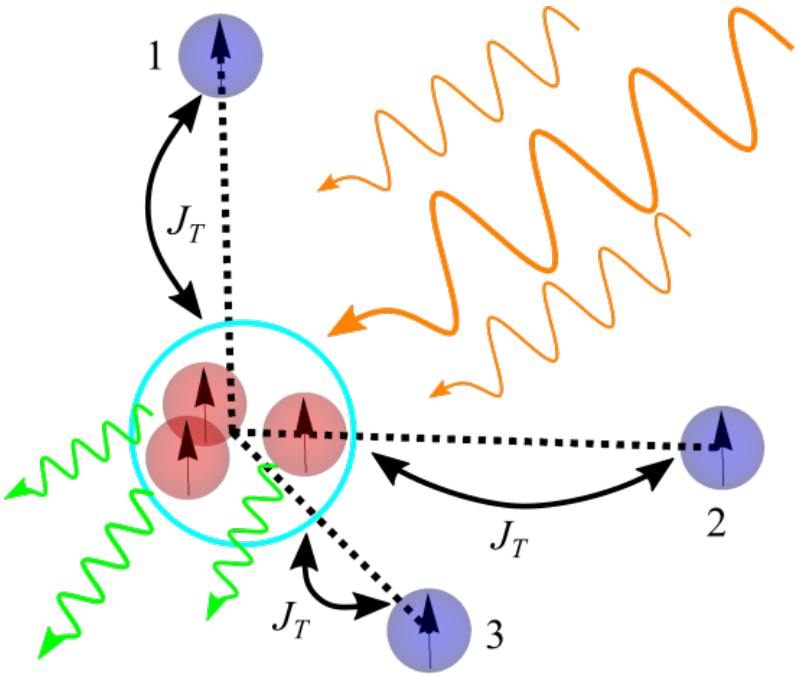

Figure 3.9: Schematic of a trimer set up for ratcheting with the three different axes for the trap 2LS (blue).

The inclusion of the trap in the system Hamiltonian means the calculation of the system eigenbasis for the dissipative processes needs to include the trap from the start, rather than only the ring and then taking a tensor product with an identity matrix to increase the Hilbert space to include the trap.

3.4.1.2 Coupling the trap to environments

The trap dipole moment, which is used to determine the dipole-dipole coupling to other antennae for extraction, can also be used to make the trap optically active. This is a relatively straightforward extension if the trap is identical to the other 2LSs, with the same energy splitting and decay lifetime. In this scenario, since the trap is still considered close to the ring, relative to optical wavelengths, one can simply add another term to the sum in the optical interaction Hamiltonian, Eq. 3.3.

The process for calculating optical Bloch-Redfield terms needs to change if the trap has a unique dipole moment. Originally, the dipole weighting contribution to interaction terms could be calculated by transforming a shared optical interaction matrix for system components, $\sum_i^N \hat{\sigma}_i^x \boldsymbol{d}_i/|\boldsymbol{d}_i|$, to the system eigenbasis and then applying the optical prefactor term, κ_{opt}, defined in Chapter 1 as a term derived from the spontaneous optical decay rate for the antennae, τ_L. Now that one of the terms in the summation of shared optical interaction matrix for system components represents an absorber with a different dipole strength, that needs to be accounted

for initially by absorbing κ_{opt} into the interaction matrix:

$$\sum_i^N \hat{\sigma}_i^x \boldsymbol{d}_i/|\boldsymbol{d}_i| \rightarrow \sum_i^N \hat{\sigma}_i^x \sqrt{\kappa_{\text{opt},i}}\boldsymbol{d}_i/|\boldsymbol{d}_i| \ , \tag{3.42}$$

where $\kappa_{\text{opt},i} = \gamma_{\text{opt},i}/\omega_i^3$, and $\gamma_{\text{opt},i}$ is the decay rate in eV for the lifetime, $\tau_{L,i}$ for the absorber i. The square root accounts for the fact that pairwise combinations of terms from the interaction matrix in the eigenbasis are used to generate the Bloch-Redfield dissipator.

The trap can be made vibrationally active by adding a new local phonon interaction term to Eq. 3.4 to make the vibrational interaction Hamiltonian [68]. The process for generating the phonon Bloch-Redfield dissipator with a coherently coupled trap is otherwise the same as was introduced in Chapter 1.

3.4.2 Results

3.4.2.1 Fine tuning trap parameters

To test our new trap model, we want to investigate the effect of varying the trap splitting, ω_t, the separation from the ring, s_t, and the choice of axis on which the trap would sit. We allow the trap to be vibrationally active, but do not couple it to the shared optical bath, so as to not introduce too many changes in one step. As we vary the parameters in this model there is some behaviour we expect to observe:

- As s_t is increased, extraction rate should decrease and power output should drop.
- As ω_t becomes degenerate with the lowest energy eigenstates in the single excitation manifold, we expect to see improved performance.

In Fig. 3.10 we plot a stack of P-V curves, each taken with ω_t is varied from 1.7 eV to 1.9 eV, while s_t moves from 5 nm to 15 nm. From left to right the panels change through the three trap axes, while top and bottom panels offer different views of the 3-D dataset. In each chart the top dataset (blue, green and yellow) represent the dataset with a close trap where $s_t = 5$ nm, whilst the bottom set (yellow, red and pink) uses a trap separation of 15 nm. It is possible to see that the when the trap is close the choice of ω_t is much less important to the performance of the dimer, however, when far away it is greatly beneficial for the trap to be degenerate with the dimer eigenstate. When this occurs the trap is still able to harvest a significant fraction of the power that it can when close. It is interesting to note that the peak performance with a distant trap occurs for $\omega_t > \omega_A$. One might assume that since ratcheting relies on relaxation to the lower eigenstate that a trap degenerate with the dimer antisymmetric state would be more beneficial.

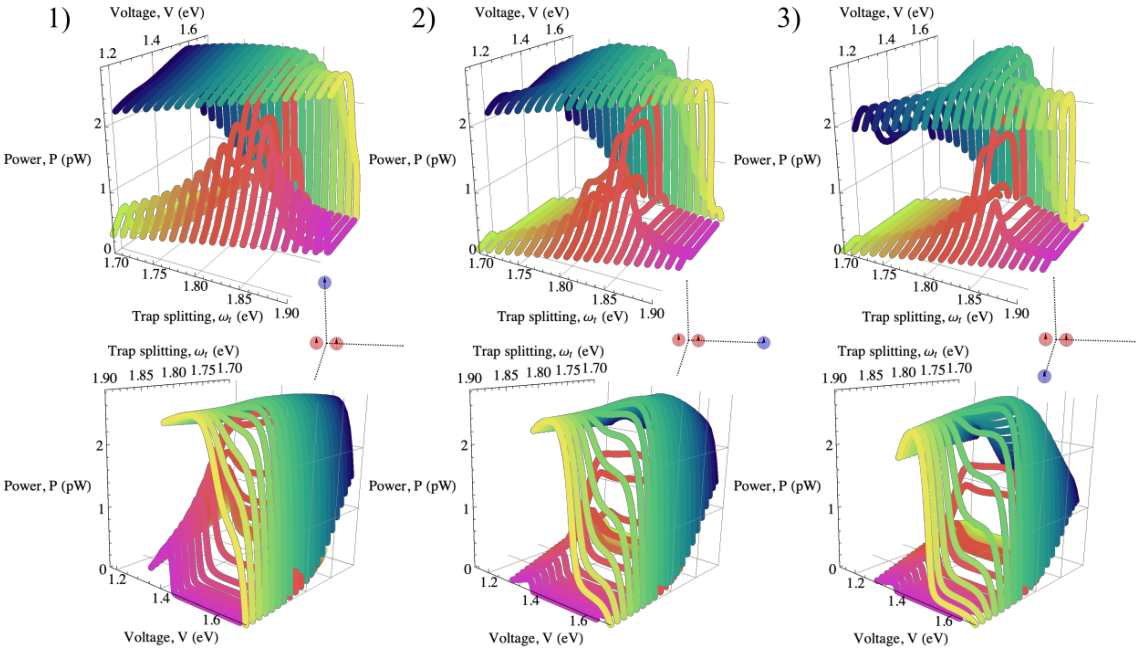

Figure 3.10: Plots of P-V curve stacks with a dimer using the coherent trap model. All three axes for the trap are used (shown in inset schematics), and in each case there is a near (blue, green and yellow) and far (yellow, red and pink) scenario. The trap frequency is much more important when the trap is far from the dimer.

In Fig. 3.11 we repeat this calculation, but increase the dipole moments of the absorbers by changing the 2LS parameters (see Tab. 3.2). The stronger dipole increases the dipole-dipole coupling, and hence causes a larger energetic separation between the two single excitation states of the dimer. This should make vibrational relaxation even more efficient. The overall power values achieved are higher with the stronger dipoles as well. When the trap is positioned close to the dimer antennae, the power extracted still does not depend much on the choice of ω_t. Performance for larger s_t however once again allows the dimer eigenstate energies to be identified. This is because the performance peaks when the trap is degenerate with them. We can now see the lower energy eigenstate provides the optimal performance for the trap on principal axis 2, but is not observable in axis 1 and 3 however, which only have peaks around the higher energy eigenstate. For a dimer, axis 1 and 3 are both symmetric, as there is the same amount of distance between the trap and both absorbers. This will not be the case for larger rings, then only axis 1 through the centre of the ring with be equidistant to all 2LSs. This symmetric setup completely prevents coupling to the antisymmetric state.

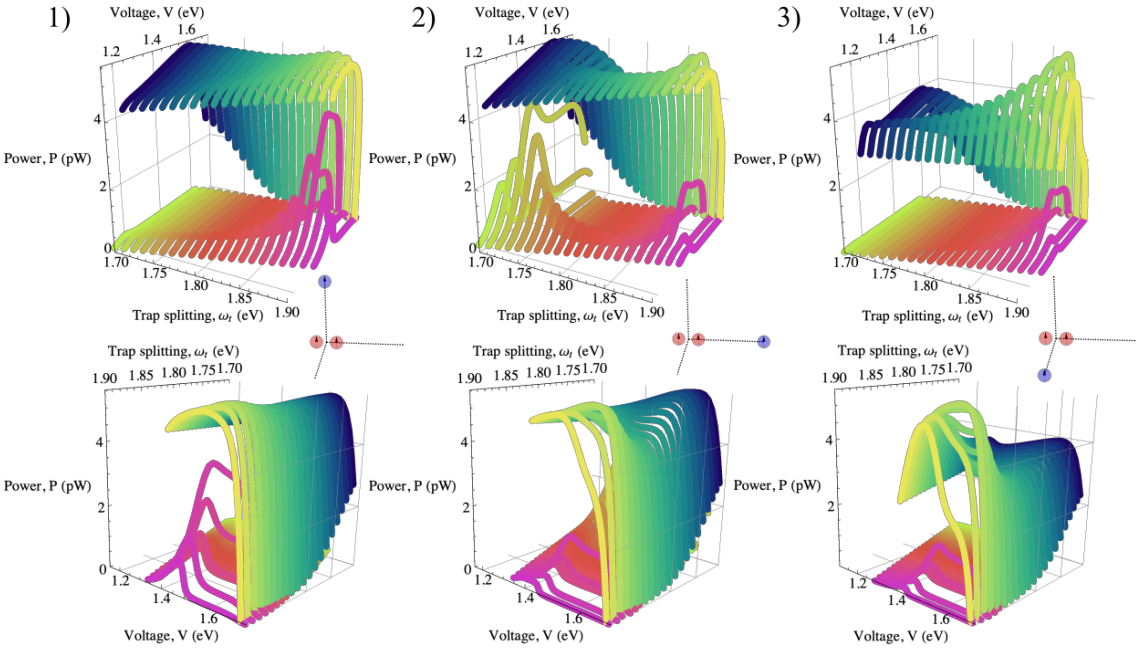

Figure 3.11: Plots of P-V curve stacks with a dimer using the coherent trap model. The dipole parameters have been adjusted to provide a stronger dipole moment. The format matches that of Fig. 3.10.

ω_A	τ_L	r_{nn}
1.8 eV	2.5 ns	1.5 nm

Table 3.2: Parameters used for stronger dipoles.

We also note that additional features in the individual P-V curves which were not present in incoherent examples in Fig. 3.2. For example, in the large trap separation case we can see that performance drops one voltage gets too low, which Fig. 3.2 showed corresponds to more aggressive trap decay rates. This implies we see Zeno behaviour preventing extraction [126]. We can also see that for larger trap splitting values, faster trap decay is needed to improve the performance when the trap separation is small. This implies that population is readily flowing back to the lower energy antenna 2LS, but that this can be countered by processing population soon after it arrives at the trap.

We now revert to the weaker dipole 2LS parameters and repeat the scan with a trimer (Fig. 3.12). We can see in this principal axis 1, which still symmetrically couples to the 2LSs, that when $s_t = 15$ nm the peak performance occurs when the trap is resonant with the higher energy eigenstate ($\omega_t > 1.8$ eV). This is also the case in the other two axes, but they do show secondary-peaks at a second point overlapping with the lower energy eigenstate. No such peak occurs in axis 1.

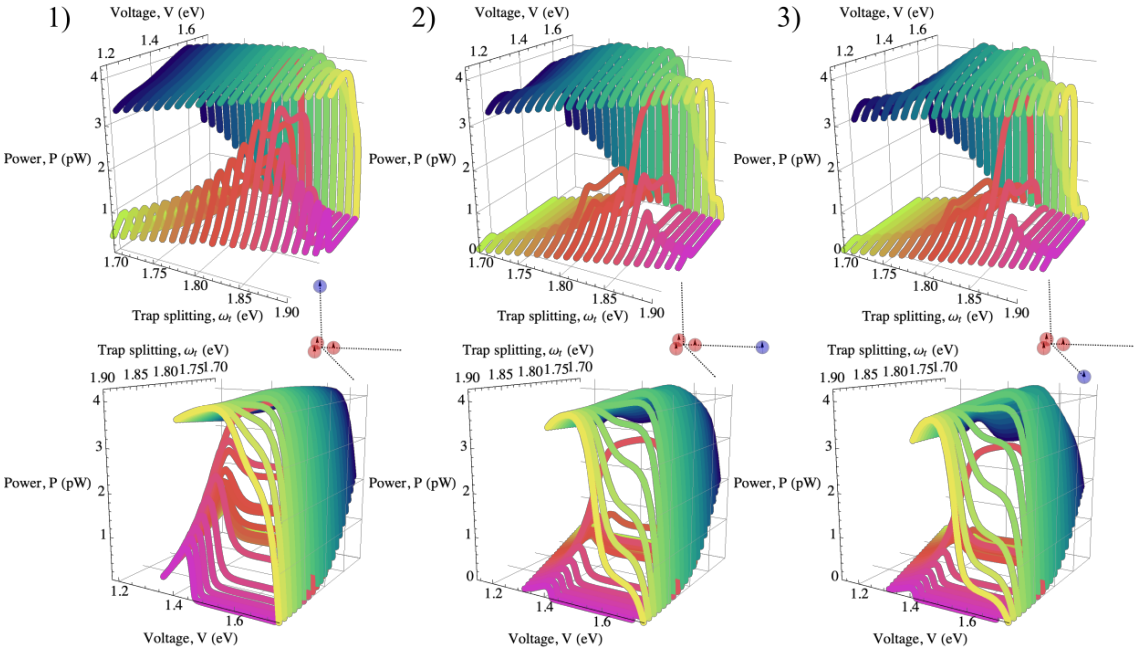

Figure 3.12: Plots of P-V curve stacks with a trimer using the coherent trap model. The format matches that of Fig. 3.10.

Finally we use the strong dipole parameters from Tab. 3.2 with the trimer in Fig. 3.13. In this case it is possible to see that the optimal performance for distant traps on the second and third axes does occur when the trap is resonant with the lower energy eigenstate. The stronger coupling from the enhanced dipole parameters means that for $s_t = 5$ nm the system performs better with a lower energy trap spitting. Small ω_t values avoid the need for fast trap decay to prevent population transferring back off the trap. With a trimer it is even more apparent than in Fig. 3.11 that with stronger dipole parameters a distant trap cannot get as close to the performance of a close trap simply by being resonant with the system eigenstates.

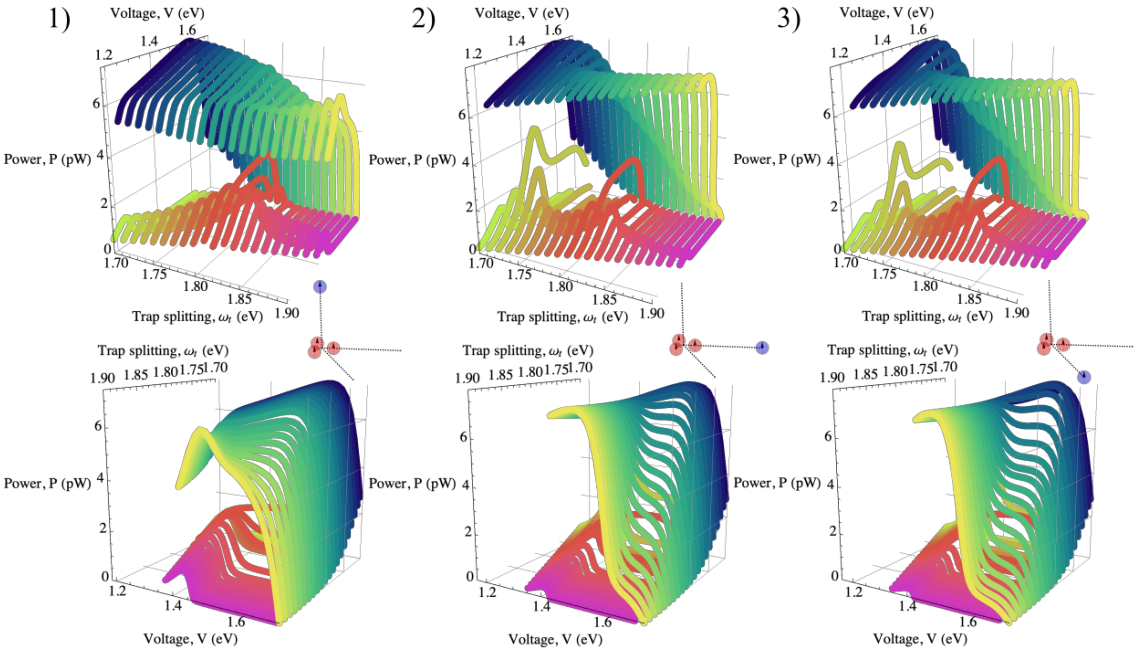

Figure 3.13: Plots of P-V curve stacks with a trimer using the coherent trap model. The dipole parameters have been adjusted to provide a stronger dipole moment. The format matches that of Fig. 3.10.

3.5 Conclusions

We have developed an extended model for looking at the effects of optical ratcheting. Having identified the key elements of optical ratcheting using weak-coupled phonons and idealised incoherent extraction we made two main changes.

The first change was to strongly couple the phonons, requiring a multi-site polaron transformation. After implementing this we confirmed if the optical dissipators in the polaron frame were still able to produce ratcheting. As was the case in Chapter 2, we found that stronger spectral densities interfere with the desired collective effects, but one of our parameter choices could still produce ratcheting. We used this spectral density in the following tests.

By varying optical concentrations, we found that ratcheting could work not only when using an idealised 5800 K optical bath, but also when accounting for the limited solid angle of the sun as viewed from the Earth. The benefits of ratcheting vanished when stronger concentrations, as have been considered in other work, are introduced. In these enhanced optical concentration scenarios we find the dimer to be either the top, or equal best performer. When we tested against robustness towards exciton-exciton annihilation, finding that ratcheting performance was affected very little, even when aggressive rates for the additional dissipative processes were introduced.

The next addition looked at the trap in greater detail, modelling it as an in-

dependent 2LS in with the geometry of the ring. Such an approach allows us to confirm the validity of results made with the incoherent extraction mechanisms. The peaking performance around the higher energy eigenstate as well as the inability to couple to eigenstates depending on geometry are factors that would need to be accounted for in an attempt to synthesise such a system.

Having independently developed the stongly-coupled polaron approach, as well as the coherent trap model, it would be interesting to combine these two approaches into one model for further insights into the potential for ratcheting systems. This model also lends itself to the kind of disorder testing which was used in Chapter 2. The combination of disorder and polaron transformation, both of which can interfere with the collective darkness of a state, might be able to aid with coherent extraction not coupling to desired eigenstates.

While the systems in both this chapter and Chapter. 2 take inspiration from biologically in their designs, the resulting multi-excitation effects would not be expected to play a role in actual photosynthetic complexes. This is because unlike the precise arrangements of absorbers we consider for idealised artificial light-harvesters, biological systems can have hundreds of components that would be very challenging to arrange perfectly. This doesn't mean Nature can't take advantage of collective effects however, as will be seen in Chapter. 4.

Chapter 4

Robust Optically Dark Behaviour in IsiA

4.1 Introduction

4.1.1 Specific contributions

The primary results of this collaboration have been compiled into a manuscript that is currently being reviewed for publication [127], on which I am co-first author. This chapter however, other than the summary of the wider scope of the work given in the previous section, will be solely focused on my contributions.

I was responsible for developing the framework that would allow us to analyse the large structures of interest for biologists as a Hamiltonian using our collective optical dipole approach, and implementing the various computational tests we wanted to carry out on the structure. This included defining a methodology for measuring the collective advantage being gained by a system, as well as how said advantage varied as chromophores were shifted or removed in order to identify key components, and give insights into the structure.

4.1.2 Project summary

This collaborative project with biological physicists focused on applying the techniques used in Chapters 2 and 3 to actual biological systems. While the proposals for man-made light-harvesters which utilise optical-ratcheting and guide-slide superabsorption rely on a very ordered and symmetric arrangement of optical dipoles in a biologically-inspired ring configuration, photosynthetic molecules in nature are considerably more complex, with potentially hundreds or thousands of components. This project focused on whether photosynthetic complexes comprised of a collection of emitters, which have evolved to operate at room temperature, could utilise collective effects to hold onto excitations for longer than would be classically expected.

The molecule that was chosen as the focus of this project is the iron stress-induced protein A (IsiA) complex, a pigment protein complex common in many fresh water cyanobacteria under iron limitation [128, 129]. Rings of IsiA, involving more than two hundred chlorophyll molecules as well as several hundred other protein pigments and carotenoids, form around photosystem I (PSI). The role of IsiA has been the topic of interesting debate in the biophysics community for the past 30 years [130, 131, 132, 133, 134, 135, 136, 58, 137, 138, 139]. The leading suggestions are:

1. An antenna for PSI, increasing the absorption cross-section, compensating for the fact that PSI subunits require more iron as a resource.

2. Protecting PSI from damage by energy quenching, whereby excess energy is not transferred to PSI, which would otherwise cause the production of damaging reactive species.

There is evidence for both of these roles, and it has been suggested that IsiA could possess dual-functionality by varying cell-physiology [139]. It is therefore interesting to develop a model that allows us to investigate how excitation properties are affected by structural perturbation.

At the conception of this work the structure of IsiA was not known, and we intended to work off of a proposed structure suggested by our collaborators. Over the course of our work however, the structure of an IsiA-PSI ring (see Fig. 4.1) was resolved to 3.48 Å using cryogenic-electron microscopy (cryo-EM) [57]. We were able to use this structure as the starting point for our own studies of IsiA. Testing the robustness of the design settled upon over the evolutionary process against various sources of noise and disorder is a challenge that lends itself to a theoretical approach, where one can adjust adjust the parameters of a chlorophyll in a complex without needing to synthesise a new molecule. A similar approach was used in work which looked at the optimal efficiency of the Fenna-Matthews-Olson complex (FMO [33]) as disorder was introduced [140], which inspired this study.

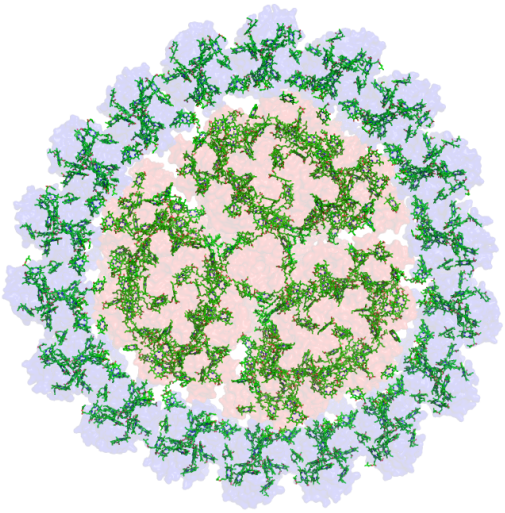

Figure 4.1: The full IsiA-PSI ring from the results of Toporik et al [57]. Chlorophyll A molecules are shown in green, while the full structures (including pigments) of IsiA and PSI are respectively shown in blue and red.

Our tests for the IsiA monomer were:

1. Examining the structure as measured by Toporik et al [57].
2. Removing a single chromophore at a time.
3. Introducing position and orientation disorder to single chromophores one at a time.
4. Introducing position and orientation disorder to all chromophores simultaneously.

As different geometries for the monomer were produced from the randomised trials we could also look at the effect on the Förster Resonant Energy Transfer (FRET) terms between the chlorophyll A molecules. By running these tests we could establish how robust the behaviour of the overall monomer is both at room temperature and cryogenic temperatures and how susceptible that robustness is to specific components within the IsiA monomer. These results supported the conclusion that IsiA has evolved to operate effectively even when influenced by thermal noise and fluid motion, but small changes can have a large effect on the functionality of the molecule, supporting the notion of dual functionality.

4.2 Model

4.2.1 Dipole geometry

The first panel of Fig. 4.2 shows the initial structure resolved with experimental data [57], and the following panels show the steps taken to extract a tractable geometrical dipole model from that starting point. First, we drop the central PSI and only consider the ring of IsiA surrounding it. Secondly, we drop all pigments and proteins, leaving only the chlorophyll A molecules from a single monomer. While carotenoid pigments can play an important role in photosynthetic systems like IsiA, they are often not included in modelling efforts due to their complicated excitonic structure [141, 142]. Finally, a disk-shaped exclusion zone is applied to each chlorophyll A molecule. These steps will now be explained in more detail in the following.

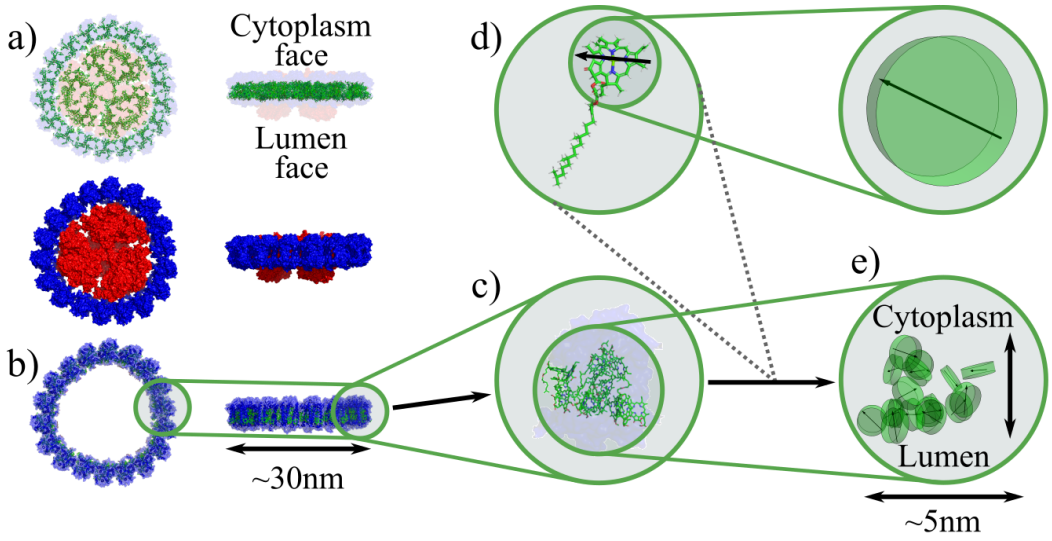

Figure 4.2: A schematic of how we move from the complicated experimental data for the full IsiA-PSI structure complete with protein pigments down to something more manageable for us to model with our dipole approach. a) The full ring from Fig. 4.1 with chlorophylls highlighted in green in the top two panels and the PSI and IsiA components highlighted more vividly in red and blue, respectively, in the bottom two images. b) IsiA structure with central PSI removed. c) We consider the chlorophyll A molecules of a single IsiA monomer subunit, ignoring other pigments. d) We disregard the chlorophyll A tails and model the chromophores as cylindrical disks to produce the model structure in panel e). When looking at single IsiA monomers we always orient the molecules so the planes defined in panel a) sit and the top and bottom of the image.

Three identical groups of six IsiA monomers repeat to produce the ring around PSI in Fig. 4.2. While we could model the full ring system, the closer separations in

one monomer lead to stronger coupling terms, and therefore have the most significant impact on the results. Considering the large number of chlorophyll A molecules in the whole ring would also dramatically increase the dimensions of the Hilbert space we need to consider. Therefore, in order to reduce the demand of computational resources, and to allow for easier readability of results, we limit ourselves to a single monomer comprised of 17 chlorophyll A molecules.

As mentioned above, we take our molecular positions and orientations of the dipoles from the cryo-EM results measured by Toporik et al [57]. From hereon, we refer to these reference positions as our 'master' configuration. The individual chlorophylls are numerically labelled and their positions within the IsiA monomer are shown in Fig. 4.3. As we wish to shift our chromophore positions and orientations from our master configuration to introduce disorder, we need a way to stop any two emitters from being too close. Computationally, the simplest check would be a spherical exclusion zone around each emitter, but by considering the actual structure of chlorophyll A (Fig. 4.3), we assign a more accurate 'disk'. We ignore the potential complexity of accounting for the attached 'tail' of atoms, as the results from Toporik et al have shown that this is not rigid and instead moves to fill available space, as seen in Fig. 4.3 [57]. We approximate the orientation of the Qy electronic transition dipole using the axis linking two nitrogen molecules on opposite sides of the disk depicted with an arrow in Fig. 4.2d [143].

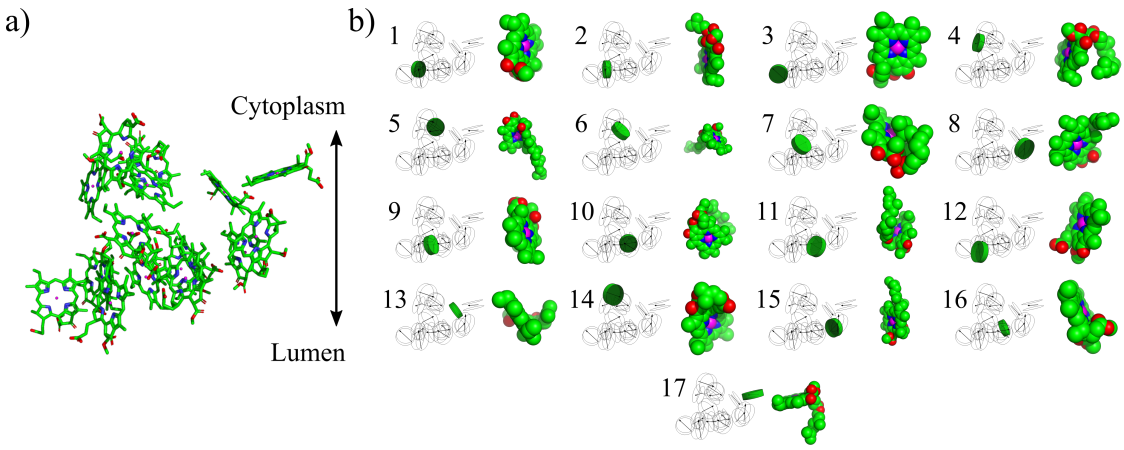

Figure 4.3: The positions of the different chlorophyll A molecules in the IsiA monomer. a) gives a 'master view' of our structure including its orientation in the organism (orientation defined in Fig. 4.2). b) Each of the 17 subpanels highlights the position of a single chlorophyll A molecule (represented as a disk) in the monomer on the left. A uniform molecular ball representation of the molecules is shown on the right of each panel, in the orientation as seen from the PSI at the centre of the IsiA ring. From these we conclude that the 'tail' is malleable, and will move to fit available space. The reference atoms for the disk approximation of the structure (see text) are magnesium (pink), and nitrogen (blue). The assignment of numerical labels of each site within the IsiA monomer follows that of Ref [57].

For the disk dimensions, if we set the thickness as the Van-der-Waals radius of the central magnesium atom (0.173 nm), and the diameter, from Toporik et al [57], as 1.23 nm then we see overlap of emitters using our master positions. The left panel of Fig. 4.4 highlights the overlapping chlorophylls (6, 7, 10, 11, 12, 14, and 16) in red. In order to avoid overlap in our master positions we could use a more complicated volume profile for the disks, for example having a reduced disk thickness further away from the centre, to account for other atoms having smaller Van-der-Waals radii. Instead we decrease the disk dimensions by 10%, allowing us to maintain the simpler shape profile. On the right hand side of Fig. 4.4 we can see the instances of cholorophyll A overlap in the monomer master positions are removed with the rescaled disk dimensions.

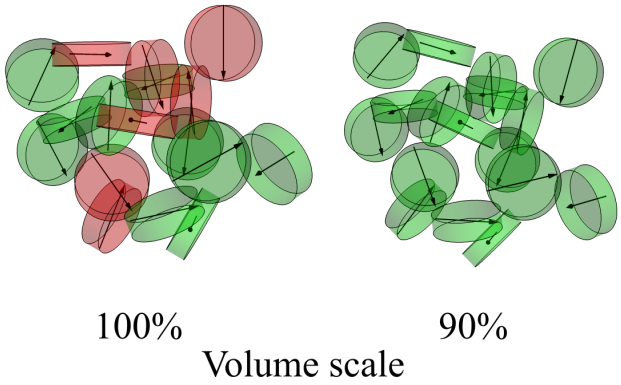

Figure 4.4: An IsiA monomer with two different scales for approximated volume profiles. Chlorophyll A molecules which intersect with the volume of another are highlighted red. The dipole directions of each chromophore are denoted by black arrows.

4.2.2 System Hamiltonian and effective model

We wish to model the chlorophyll A molecules in IsiA as a collection of optical dipoles, each represented as a two level system (2LS). Each 2LS has an energy splitting, ω_α as well as a dipole moment, $\boldsymbol{d}_\alpha$. The radiative lifetime for chlorophyll A, $\tau_\alpha = 15$ ns [144, 145], is used alongside $\omega_\alpha = 1.85$ eV to determine the magnitude of the dipole moment, $|\boldsymbol{d}_\alpha| = \sqrt{3\pi\epsilon_0\tau_\alpha^{-1}c^3/\omega_\alpha^3}$ [80, 81]. Since the distances between absorbers are on the order of single nanometres [57], they are small relative to the optical wavelengths, meaning the system couples collectively to an optical field [66]. The shared photon environment also induces resonant dipole-dipole Förster-type couplings between chromophores [78, 79]. The coupling, $J_{\alpha,\beta}$, between two emitters depends on both the dipole moments, and separation vector, $\boldsymbol{r}_{\alpha,\beta}$, taking the form

$$J_{\alpha,\beta}(\boldsymbol{r}_{\alpha,\beta}) = \frac{1}{4\pi\epsilon_0|\boldsymbol{r}_{\alpha,\beta}|^3}\left(\boldsymbol{d}_\alpha\cdot\boldsymbol{d}_\beta - \frac{3(\boldsymbol{r}_{\alpha,\beta}\cdot\boldsymbol{d}_\alpha)(\boldsymbol{r}_{\alpha,\beta}\cdot\boldsymbol{d}_\beta)}{|\boldsymbol{r}_{\alpha,\beta}|^2}\right). \tag{4.1}$$

This expression for the dipole-dipole couplings is effective for point dipoles, so for it to be accurate for our molecular dipoles there needs to be adequate separation between the absorbers for the approximation to hold, alternatively a fractional charges approach can be used which considers the distribution of charge across each molecule when calculating the coupling [79]. The minimum separation in the master configuration is on the order of a nanometre, and exclusion zones also ensure dipoles do not get too close together. We do not discount any dipole-dipole interactions in our calculations for an IsiA monomer, but if one were to consider the larger IsiA ring, which can have separations on the order of tens of nanometres between chromophores, then one might want to consider ignoring some due to the dielectric screening effect since the dipole moments should not be perceivable at long range.

In order to model the optical processes, we use the collective quantum optical interaction [66],

$$\hat{H}_{I,\text{opt}} = \sum_{i=1}^{N} \boldsymbol{d}_i \hat{\sigma}_i^x \otimes \sum_k f_k(\hat{a}_k + \hat{a}_k^\dagger) \ , \tag{4.2}$$

where $\hat{\sigma}_i^x$ is the standard Pauli operator for site i, and f_k and $\hat{a}_k^{(\dagger)}$ are, respectively, the coupling strength, and annihilation (creation) operator for the optical mode k. As we lack detailed vibrational information, we do not include a microscopically derived model for the phonon processes, but we do capture the general behaviour that spin-boson type interactions induce, namely transitions that link system eigenstates in the same excitation manifold [146, 19, 23]. For reference, the multi-site spin-boson interaction Hamiltonian is

$$\hat{H}_{I,\text{vib}} = \sum_{i=1}^{N} \hat{\sigma}_i^z \otimes \sum_q g_{i,q}(\hat{b}_{i,q} + \hat{b}_{i,q}^\dagger) \ , \tag{4.3}$$

where $g_{i,q}$ and $\hat{b}_{i,q}^{(\dagger)}$ are, respectively, the coupling strength, and annihilation (creation) operator for the vibrational mode q for the bath linked to site i. Since the nanometre scale systems we consider are large relative to the characteristic length scales of phonons we treat them as separate baths. We note that if we considered a shared phonon bath with appropriate position-dependent phase factors [147, 148] we would not observe a qualitative difference in results [149]. We write our environment Hamiltonian terms as baths of oscillators for our shared photon, and local phonon environments, respectively, as $\hat{H}_{B,\text{opt}}$ and $\hat{H}_{B,\text{vib}}$. Our total Hamiltonian now becomes

$$\begin{aligned} \hat{H}_{\text{total}} = \omega_\alpha \sum_{i=1}^{N} \hat{\sigma}_i^z + \sum_{i \neq j}^{N} J_{i,j} \left(\hat{\sigma}_i^+ \hat{\sigma}_j^- + \hat{\sigma}_i^- \hat{\sigma}_j^+ \right) \\ + \hat{H}_{I,\text{opt}} + \hat{H}_{I,\text{vib}} + \hat{H}_{B,\text{opt}} + \hat{H}_{B,\text{vib}} \ , \end{aligned} \tag{4.4}$$

in which we define the system Hamiltonian as

$$\hat{H}_{\text{sys}} = \omega_\alpha \sum_{i=1}^{N} \hat{\sigma}_i^z + \sum_{i \neq j}^{N} J_{i,j} \left(\hat{\sigma}_i^+ \hat{\sigma}_j^- + \hat{\sigma}_i^- \hat{\sigma}_j^+ \right) \ . \tag{4.5}$$

As seen in Chapters 2 and 3, for a small number of sites the dynamics of our system can be determined to second order based on a Born-Markov approximations in the Redfield formalism [66, 23]. For the large number of emitters needed to model biological systems it is computationally challenging to produce full dynamics due to the growth of the Hilbert space. By limiting ourselves to the ground state and single excitation subspace we reduce our Hilbert space for N 2LSs from 2^N states to $1 + N$ states (Fig. 4.5). While multi-excitation effects could boost the performance

of man-made absorbing systems [19, 150, 23], for the low intensity of light typically incident at the surface of the Earth, we do not commonly expect biological light-harvesters to have more than one excitation at any time [1]. This simplification also means we do not need to consider effects like exciton-exciton annihilation [151, 152].

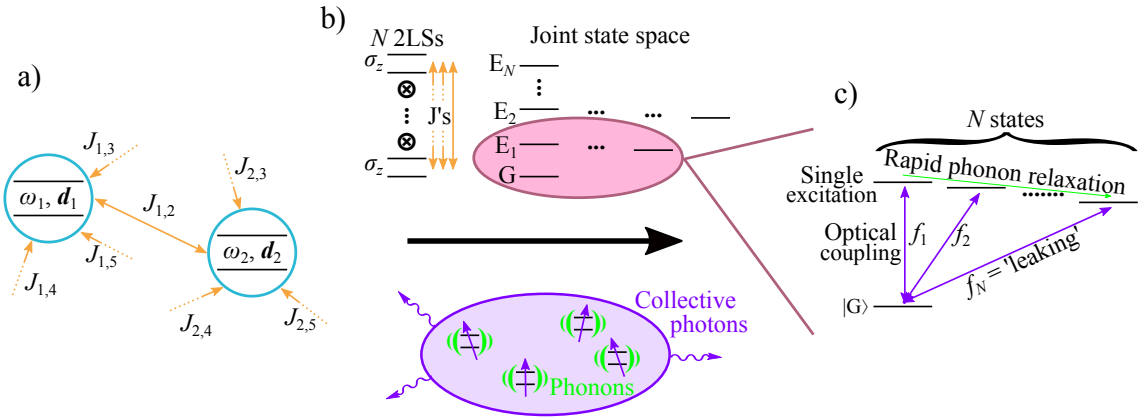

Figure 4.5: Schematic of the reduced system Hamiltonian we are considering. a) Our collection of N dipoles is represented as 2LSs linked by distance and relative orientation dependent coupling terms. b) The site energies and couplings are used to find the eigenbasis, from which we take the eigenstates for the ground state as well as single excitation states. Each 2LS interacts with a collective optical field dependent on its dipole moment. Individual vibrational baths effect each 2LS identically. c) The optical transition strengths and effect of phonon relaxation are then calculated for our chosen eigenstates, allowing us to calculate a leaking value.

In Fig. 4.5 we present a schematic of our approach to reducing the Hamiltonian and Hilbert space. For an N absorber system we calculate the energies of the N eigenstates of the single excitation manifold by finding the diagonal basis for our system Hamiltonian. We then calculate the dipole contribution for each of the transitions linking single excitation eigenstates to the ground state following the same procedure used in Chapters 2 and 3. We assume rapid relaxation into phonon modes means that any population in the single excitation manifold will be rapidly redistributed. A common assumption in chemistry as Kasha's rule [153], which assumes all population will be moved to the lowest energy single excitation state. Explicit modelling of phonon transitions in similar systems supports the assumption of redistribution of nearly all population in the single excitation manifold to the lowest energy eigenstate with adequate energetic separation of states [23, 117].

[1] If we assume solar irradiance of 1 kW/m^2 with monochromatic monochromatic light of 500 nm, the interval between incident photons on a cross-section with radius 15 nm would be 0.6 μs, considerably longer than the radiative lifetimes of the emitters.

4.2.3 Defining a leaking value

In order to benchmark the performance of our systems, we take the dipole contribution for the transition linking the lowest energy excited state to the ground state and define it as the 'lowest-energy leaking value', L. If the leaking value is greater (less) than one, then the system is exhibiting brightness (darkness), and the system will emit an excitation faster (slower) than an isolated absorber. We are primarily interested in darkness, as this implies collective quantum effects are being used to hold onto excitations for longer than would be classically expected.

Since all the emitters we consider in IsiA are identical chlorophyll A molecules, we can normalise L such that $L > 1$ is bright, and $L < 1$ is dark. Using the radiative lifetime of the emitters, τ_α, one can get an indication of the lifetime of an excitation in such a collective system made up of identical chromophores by calculating τ_α/L. If a collection of chromophores has components with differing lifetimes then the choice for normalisation becomes less clear; one could benchmark against the darkest contributing dipole, which will have the longest lifetime, or alternatively use the most common emitter or a weighted average based on the count of each type of molecule present [2].

The optical rates for transitions linking two eigenstates when calculated with a flat spectral density for the photons also depend on the transition frequency between the two states[66, 23]. Since all of the absorbers in IsiA are identical, all of the eigenstate energies are of the same order as the absorber energy (ω_α), with deviations on the order of the couplings between the absorbers ($J_{\alpha,\beta}$). Provided the coupling energy scales are much smaller than the site energy, one can ignore the effect of the transition frequency on the rate, as it can be approximated to be the same as the site energy. Note that this cannot be done if either absorbers are not identical and have significantly different site energies, or if large couplings between sites cause eigenstate energies to be significantly shifted from site energy.

For energy splittings between eigenstates from the induced Förster couplings that are relatively small the assumption that all population will fall to the lowest energy state in the single excitation manifold becomes invalid. If, for example, the lowest energy eigenstate has a very small leaking value, but a state with an eigenenergy just a few meV higher has a strong contribution, then one would still expect the higher energy state to be populated at room temperature ($k_B \times 300$ K ≈ 25 meV). To account for this we use a 'Boltzmann-corrected leaking value', L_{boltz}, where we look at the dipole contributions of every transition linking a single energy excitation

[2]Note that the focus on the collective effect of the dipole contribution affects both radiative absorption and emission processes. Non-radiative decay could introduce another loss channel for excitations [151], but unless such effects were modelled to depend on the system geometry it would be a constant contribution, and as such would not effect the discussion on relative brightness and darkness being introduced by modelling chromophores collectively

eigenstate to the ground state, and sum them with a Boltzmann weighting,

$$w_i = \frac{e^{-E_i\beta}}{\sum_k e^{-E_k\beta}} \ , \tag{4.6}$$

where i is the single energy eigenstate, E_i is the eigenstate energy, and $\beta = 1/k_BT$ at the temperature of the local environment. The Boltzmann weighted leaking value is therefore defined as

$$L_{\text{boltz}} = \sum_i w_i |\boldsymbol{d}_i|^2 \ . \tag{4.7}$$

Note that the i index is being used to label in the energy basis rather than the site basis.

After having found either a single lowest-energy eigenstate, or a Boltzmann-weighted combination of eigenstates, we can transform from the eigenbasis back to the site basis. This allows us to determine the weightings of different chromophores that contribute to the radiative decay of the system in a thermalised state. In Fig. 4.6 we can see the distribution of population in the IsiA monomer for the both the minimum energy eigenstate leaking value (left), and the Boltzmann leaking value at room temperature (right). We can see that the ninth chlorophyll A molecule takes most of the population in both scenarios, but the Boltzmann approach flattens out the distribution slightly, as would be expected when more optical pathways are contributing.

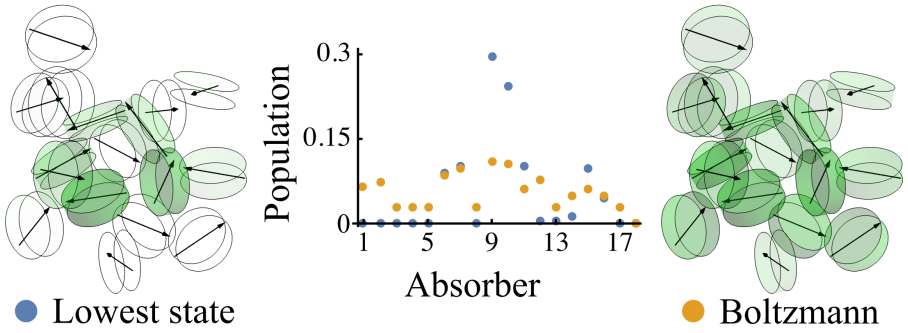

Figure 4.6: The population localisation on the IsiA monomer sites for the steady state found with both the lowest state leaking value and the Boltzmann leaking value at $T = 300$ K.

4.2.4 Introducing disorder

The nature of our model allows us to introduce disorder to both the optical properties, and geometric positions of our chromophores. If one were to vary the absorption properties of each emitter then the dipole moments of each absorber would change, in turn affecting the dipole-dipole coupling strengths and similarly leading to a new leaking value. Having a series of dipoles with slightly disordered optical properties

would also affect the normalisation process of leaking values, since there would no longer be a single dipole strength to benchmark against. Changing the absorber geometry alters the position and orientation dependent couplings terms between the dipoles, which in turn would affect the eigenstates for the system, and the optical connectivity of those states.

For the results in the IsiA study we only considered introducing geometric disorder to the 2LSs, since each dipole represents an identical chlorophyll A molecule. Varying the optical properties could potentially be used as a method of accounting for the influence of the other proteins present in the system which are not included in our IsiA model. Rather than simply applying disorder to the 3-D position and angle for each 2LS dipole, we instead utilised the disk volume profile described above. This ensured we only considered plausible disordered setups, where the chlorophyll molecules were not overlapping.

We shall refer to our introduced disorder levels in terms of percentages. The percentages represent the standard deviation of the normal distribution used to vary the parameters in each trial. For the position and angle of each 2LS we need to vary 6 parameters, displacements in three Cartesian directions as well as pitch, roll and yaw for the dipole moment. Each parameter needs a characteristic value to take a percentage of to define the standard deviation. Angular disorder uses a 2π rad complete rotation, while position disorder uses the characteristic length scale defined as the largest distance between two dipoles in the monomer (4.6 nm [57]). Due to the three disordered displacements for both position and angle we divide our characteristic values by $\sqrt{3}$. Consequently, whenever we refer to, say, 2% disorder in the following we shall mean both positional shifts in all three coordinates and three orthogonal rotations all based on Gaussian distributions with, respectively, widths 0.53 Å and angles of 0.023π rad.

4.3 Results

4.3.1 IsiA

4.3.1.1 Master configuration results

The first results results we consider with our IsiA model are those for the master configuration. We find a the lowest state leaking value for the monomer to be 0.195, implying an excitation lifetime roughly five times longer than would be expected for a single chlorophyll A molecule. The Boltzmann leaking value at 300 K is calculated to be 1.29, implying the room temperature lifetime would be roughly 6 times shorter than the lifetime at close to 0 K, which is well represented by the lowest state leaking value. This provides qualitative agreement from experimental results which see a factor of $\approx 4 \rightarrow 5$ separating cryogenic and room temperature

fluorescence lifetimes [154]. Note that due to the approximations used in our model, such as dropping other proteins, we do not expect complete quantitative agreement in our τ_α/L lifetimes.

In Fig. 4.7 we plot out the variation of L_{boltz} over a temperature range from 0 K to 450 K, highlighting room temperature (300 K) as well as temperatures that can be achieved when using liquid nitrogen (77 K) and liquid helium (4 K) as coolants. The difference between the leaking values at these different temperatures highlights the considerations experimentalists must make when studying molecules at cryogenic temperatures in order to learn about their normal operation in nature. We note that the Boltzmann weighted leaking value is very stable around room temperature, showing no significant variation over a temperature window of ±100 K, indicating a high degree of robustness.

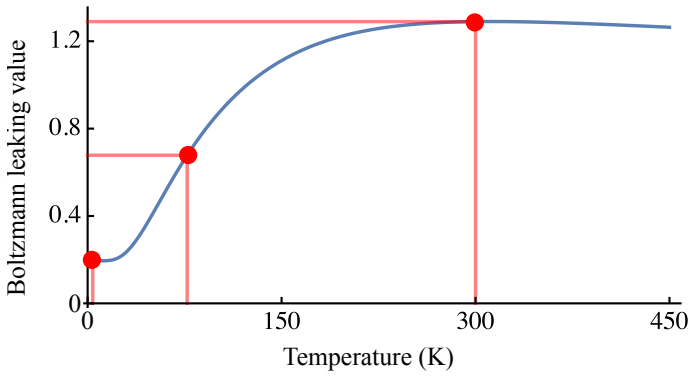

Figure 4.7: Boltzmann leaking value as a function of temperature for an IsiA monomer with all chlorophylls in their master positions. Room temperature, liquid nitrogen and liquid helium highlighted for reference. Note that the limit of $T \to 0$ K corresponds to the 'lowest state' leaking value.

Having established our model is able to qualitatively capture IsiA fluorescence lifetime behaviour seen in experiments [154], we move onto tests that could not easily be carried out experimentally, by varying the IsiA monomer structure.

4.3.1.2 Removal of single chlorophylls

Our first test on editing the structure was to remove one chlorophyll A molecule at a time, and measure the effect this has on the lowest state leaking value and Boltzmann leaking value. In Fig. 4.8 we can see that the removal of some chlorophyll A molecules appears to have very little affect on the leaking value, whereas some cause drastically stronger effects. These changes are generally more noticeable in the lowest state leaking value, where we see the removal of three dipoles lower L (12, 15, and 16), and six cause and increase in L (6, 7, 9, 10, 11, and 14). This pattern is mostly consistent in the Boltzmann weighted leaking value, other than for chlorophylls 6 and 14, the removal of which causes a reduction in L_{boltz}.

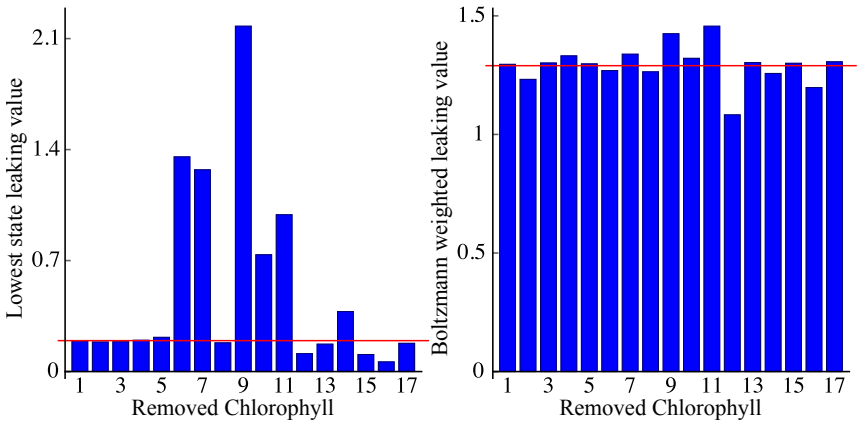

Figure 4.8: Leaking values as single chlorophyll A molecules are removed. The left panel shows the lowest state leaking value, while the right displays the Boltzmann weighted leaking value. In both panels the value from the master configuration is illustrated by a red line.

4.3.1.3 Disorder in single chlorophylls

Our second trial that perturbed the master configuration was to introduce geometric disorder to each chlorophyll A molecule, one at a time. In each trial we use a normal distribution with a 2% standard deviation window to introduce disorder for the parameters. In Fig. 4.9 we plot out histograms for both the lowest state, and Boltzmann leaking values. Due to the volume exclusions discounting invalid random setups where there is overlap on emitters we have between 109 and 299 valid trials for shifting each chromophore. These results support the result from the previous section, showing the IsiA leaking value is robust against changes in some chromophores, while others are able to dramatically affect the functionality from a relatively small shift.

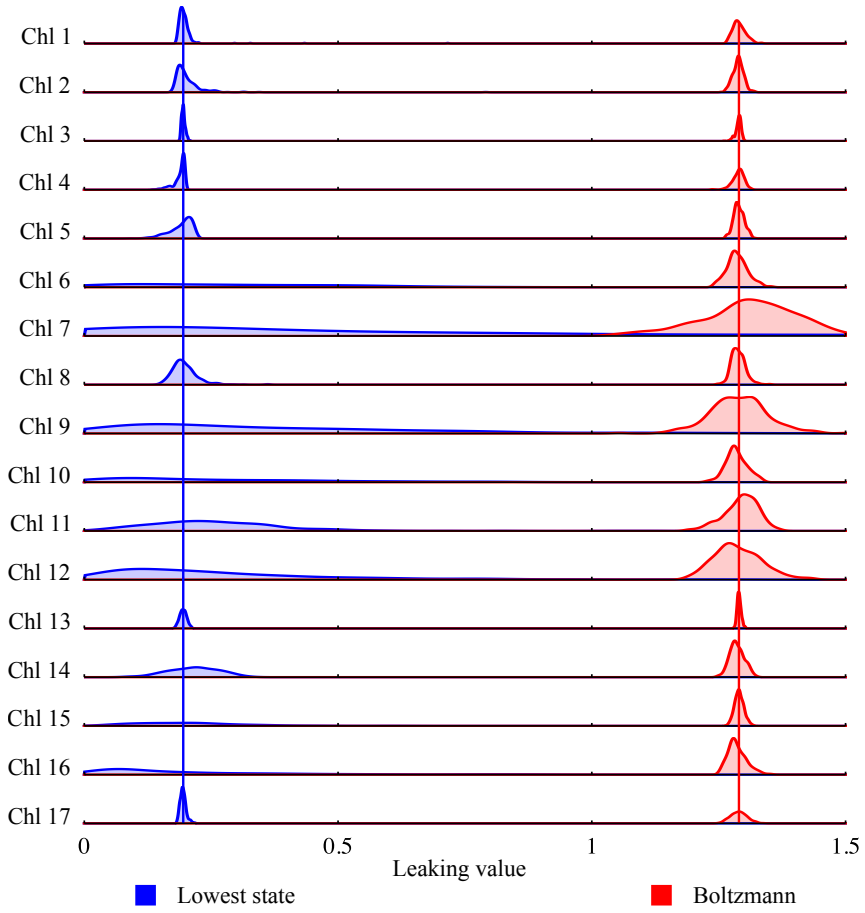

Figure 4.9: Distribution of leaking values as single chlorophyll A molecules are shifted with 2% disorder. The blue regions show the lowest state leaking value, while the red displays the Boltzmann weighted leaking value. In both panels the value from the master configuration is illustrated by a solid line. In each layered plot the data is normalised such that the highest peak in is the same height in each layer.

4.3.1.4 Disorder in all chlorophylls simultaneously

Finally, we ran simulations with disorder introduced at four different levels: 1%, 2%, 5%, and 10%. Both the position and orientation parameters of all chlorophyll A molecules were disordered simultaneously. In Fig. 4.10 are plotted probability distribution histograms for the leaking values arising from the trials with the different levels of disorder. In the upper panels show Boltzmann leaking value shows that the behaviour at room temperature is very robust to disorder levels of $1 \rightarrow 2\%$. The cryogenic temperature behaviour shows more of a spread in the lowest state leaking value, and is more likely to exhibit brighter behaviour that the Boltzmann case for disorder greater than 2%. It should be noted that fewer trials could be produced for larger disorder levels, as the majority of random trials needed to be disregarded due to overlap of chlorophylls.

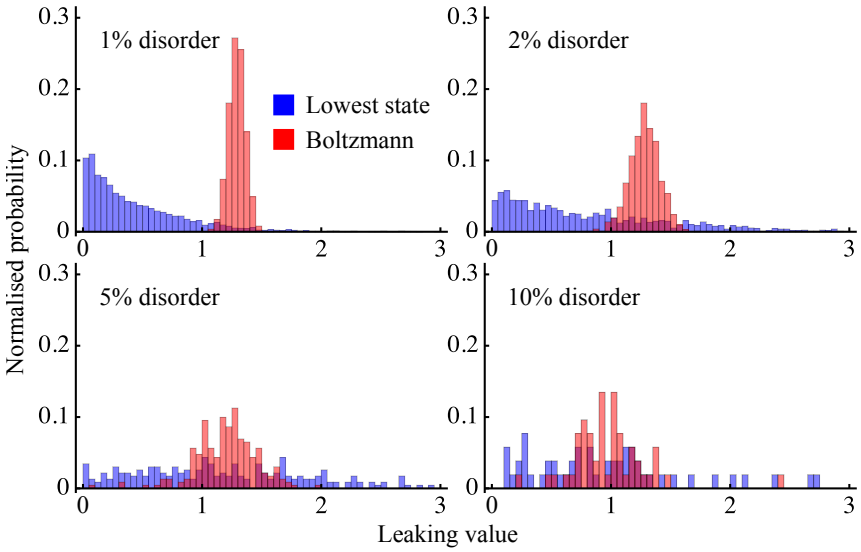

Figure 4.10: Probability distribution histograms of leaking values as all chlorophyll A molecules are shifted with 1%, 2%, 5%, and 10% disorder. The blue regions show the lowest state leaking value, while the red displays the Boltzmann weighted leaking value.

4.4 Conclusions

Through the work in this project, we were able to establish that the structure of IsiA does indeed support the suggestion that it has evolved to take advantage of optical darkness. The strength of this effect however, is greatly influenced by temperature of the vibrational environment when considering cryogenic temperatures vs room temperature, which is of note for experiments which study such systems using these temperatures. For the ambient temperatures one would naturally expect to find the complex in however, there is very little variation.

Through computational means which would be difficult to experimentally realise we established that the effect of optical darkness in IsiA was robust against general shifts in the chlorophylls, but it was susceptible to change in some specific components more than others. Our results support the suggestion that IsiA has evolved to operate robustly against both fluid motion, and the thermal noise it would naturally expect to encounter.

The approach we have used in this work of combining known biological structures with numerical modelling allow the relationship between structure and function to be easily explored computationally. This approach could be expanded to cover more components in the IsiA-PSI complex or other biological systems entirely. By including a reaction centre, we could also also begin to look at transport through the photosynthetic process, a subject of great interest in the field [155, 156, 20], while also considering loss collective optical effects.

This work has highlighted some of the constraints that are encountered when modelling larger biological systems with many components. This is a challenge that is encountered again in Chapter 5, where multiple large aggregates are considered.

Chapter 5

Molecular Dimer Laser Proposal

5.1 Introduction

5.1.1 Specific contributions

The primary results of this collaboration have been compiled into a manuscript that is currently being reviewed for publication [59], on which I am second author. This chapter however, after summarising the wider scope of the work in the following section, will be solely focused on my contributions.

The focus of my contribution was to provide supporting evidence for the approximations that were used in the manuscript to arrive at an equation for the laser behaviour that could be expected from molecular aggregates. We looked for agreement between the model developed by our collaborators and a more fleshed out model examining the behaviour of a dimer system under the Bloch-Redfield formalism which we developed. This agreement allowed us to have confidence that the approximations taken to reduce the computational demand of modelling laser behaviour from such a system were still producing reasonable results. Once agreement was established the reduced two level approach was then applied to larger molecular aggregates, as seen will be seen in Fig. 5.3 which is taken from the manuscript [59].

5.1.2 Project summary

This collaborative project with another open quantum systems theory group, as well as a quantum optics group, proposed a novel design for a laser (Fig. 5.1), based upon the idea of using molecular aggregates (initially dimers) as a gain medium. The idea relies upon using a collectively enhanced transition to pump the system with incoherent sunlight, before rapid vibrational relaxation moves the system to a state from which emission is directed into a resonant cavity.

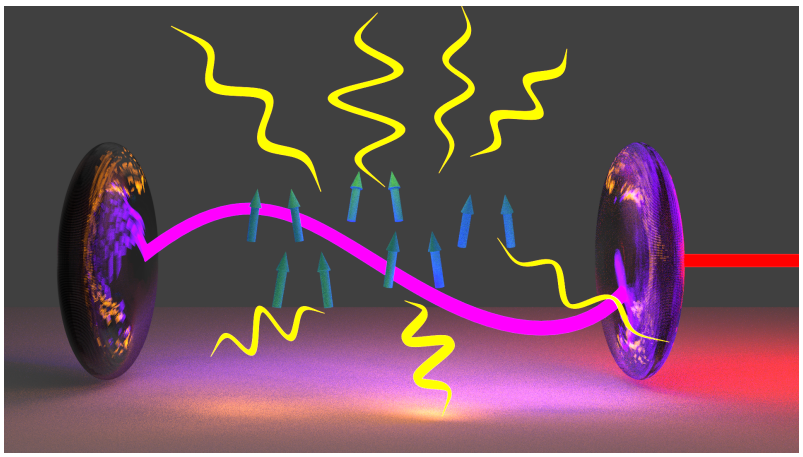

Figure 5.1: An artistic rendering of the proposed scheme; a collection of dimers excited by sunlight within a cavity.

Taking the design of the photosynthetic mechanism in purple bacteria as inspiration [39, 40], we found the use of molecular aggregates has potential to relax the conditions needed to achieve sunlight-pumped lasing. Sunlight is an abundant and renewable energy source, though from the surface of the Earth it is also dilute and variable, making schemes for storage and conversion important. Sunlight-pumped lasing offers a potential solution to these problems [157]. Transforming the incoherent sunlight into intense coherent light via sunlight-pumped lasing can allow the driving of chemical reactions for energy storage, and has been suggested as a key component in renewable energy solutions like the magnesium cycle [158, 159, 160].

One important consideration for sunlight-pumped lasing is the intensity required for achieving the lasing threshold. Concentration of sunlight is benchmarked in 'suns', where 1 sun= 0.14 W/cm^2, and can be achieved with either imaging or non-imaging concentrators, where the former involves concentration using mirrors to images the Sun, while the latter rely on passing radiative energy entering from a larger aperture out of a smaller aperture with minimal losses [161]. The current state of the art lasers operate with a lasing threshold over 1000 suns, and there are proposals with thresholds of a few hundred suns [162]. While concentrations of 10^5 suns have been experimentally realised, the substantial technical overhead makes reducing lasing thresholds a desirable goals. A commonly used means of concentration utilises mirrors to heat a black body cavity to temperatures from 1000 K to 3000 K [157].

Inspired by photosynthetic complexes which, as was seen in Chapter 4, are often modelled as as collections of two level systems (2LSs), each representing a component in the complex [39, 40, 163, 164, 35, 37, 165, 166, 167, 168, 127], we propose a biomimetic molecular architecture to achieve efficient sunlight-pumped lasers even able to operate with 1 sun pumping. From Chapters 2 and 3 we know that smaller systems of dipoles offer the possibility for very ordered and symmetric structures,

which can be used to form eigenstates with either a concentration, or lack, of dipole strength, leading to respectively bright or dark behaviour [39, 40, 166, 169]. The larger systems found in photosynthetic complexes such as IsiA-PSI, LHI and LHII are unlikely to display total darkness or brightness, as is discussed in Chapter 4, but instead balance absorption with excitation transfer reaction sites to initiate chemical reactions and store the absorbed energy [39, 40]. Both bright and dark states are present in the single excitation manifold of many naturally occurring and artificially synthesised molecular aggregates [170, 171, 172, 173], and the lasing properties of such aggregates have been the subject of previous studies [174, 175, 176].

At the centre of our design is a molecular H-dimer, where the higher energy state in the single-excitation manifold is brighter than the lower energy state. Since we consider identical absorbers in the aggregate, it is also a homodimer. Under solar illumination population is primarily absorbed by the bright state, and then rapid relaxation into phonon modes transfers population to the lower energy darker state. With enough of a difference between the brightness and the darkness of the two states such a system has the potential to achieve population inversion, a necessary step for designing a laser. Rather than just relying on precise dimer design in order to achieve the desired differences in brightnesses of the two states, we also consider increasing the pumping to the bright state by replacing the reaction centre in the middle of photosynthetic complexes in purple bacteria, "Rhodobacter Sphaeroides", with our H-dimer [39, 40]. This substitution allows the dimer to benefit from the antenna affect of the surrounding molecules, which have evolved to efficiently absorb light and transfer it to the central reaction centre for harvesting.

As a quick reminder, a laser design utilises a level structure (Fig. 5.2), exciting a gain medium via a pump transition, before relaxing with a lasing transition back to the ground state and then repeating the cycle. By placing the gain medium in a cavity which is resonant with the lasing transition, one can build up population in the cavity and have a controlled laser. The choice of gain medium determines the energy levels, and therefore the requirements of the pump as well as the properties of the laser.

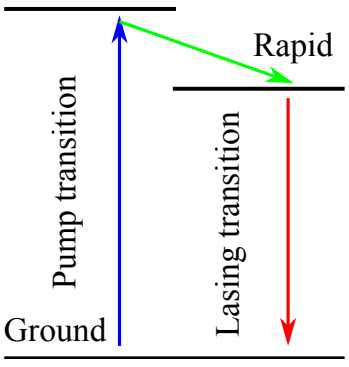

Figure 5.2: A cartoon of the basic level structure concept behind a three level laser.

By starting with a derivation of a lasing equations for a molecular aggregates, we investigate the conditions necessary for lasing in a random ensemble of H-dimers, before adding LHI and LHII rings to make the conditions necessary for lasing less restrictive. The lasing equation derivation, which can be found in full in Ref. [59], assumes rapid phonon thermalisation and discounts the possibility of further excitation beyond the single-excitation manifold. In Chapter 4 we discussed the low levels of solar illumination as justification for discounting higher excitation manifolds, however the potentially strong coupling to a cavity in this scenario means this cannot so easily be assumed, as a strong enough field may induce further excitation. With these assumptions our simplified model reduces the lasing behaviour of a molecular aggregate to incoherent interactions between two states. The population difference between the two states is found by summing contributions from each of the singe-excitation manifold eigenstates with

$$D_{eq} \approx \frac{\sum_k \chi_k n_T^k - \langle \chi \rangle}{\sum_k \chi_k n_T^k + \langle \chi \rangle} \ , \tag{5.1}$$

where the relative brightness of the eigenstate $|k\rangle$ is given by $\chi_k = \gamma_k/\gamma_o$. The spontaneous emission rate for a single molecule and a the eigenstate are, respectively, γ_o and γ_k. The thermal average of the relative decay rates of all the single-excitation states, $\langle \chi \rangle$, is:

$$\langle \chi \rangle = \sum_k \chi_k \frac{e^{-E_k/k_B T}}{\sum_n e^{-E_n/k_B T}} \ , \tag{5.2}$$

where E_k is the energy of the single-excitation eigenstate. By averaging across all single-excitation eigenstates, one can account for all the possible excitation and relaxation processes between the ground state and single excitation manifold. Excitations from the ground state are weighted by their relative brightnesses, with excitations to brighter states more likely to occur than to dark states. The relaxation processes require a thermal weighting however, as population due to vibrational relaxation is assumed to occur instantaneously, this means optical relaxation processes are both by their brightness and the probability of the thermal excitation necessary from the lowest energy single-excitation manifold eigenstate. This weighting is similar to the one used to define the Boltzmann leaking value in Chapter 4.

The intensity and power output for the field are, respectively

$$I = \frac{\hbar \omega_c c}{V} n_o \ , \tag{5.3}$$

$$P_{out} = \frac{\kappa V}{c} I = \kappa \hbar \omega_c n_o \ , \tag{5.4}$$

where V is the cavity volume, κ is the cavity loss rate, ω_c is the cavity frequency, and n_o is the stationary number of photons in the cavity. The form for n_o, which is derived in full in Ref. [59], is a function of D_{eq}, κ, the number of aggregates

in the cavity, and the total absorption and decay rates between the ground state and single-excitation manifold. In Fig. 5.3, which is taken from the collaborative manuscript associated with this work, the headline results involving the LHI and LHII complexes are displayed. In the top panels are schematics for the H-dimer and surrounding LHI ring, both with and without further antennae from LHII, as well as a schematic of the single excitation manifold eigenstates arising from such a configuration, and processes involved in linking those states. In the lower panels are the results for the laser field intensity and power output found when one varies the density of aggregates, n_A, and $\langle\chi\rangle$. In the final panel, Fig. 5.3h, we show that the behaviour for lasers utilising these complicated multi-chromophore aggregates can be calculated using our model developed for the dimer, and rescaling the pumping to account for the additional antenna, which is a much less resource intensive approach.

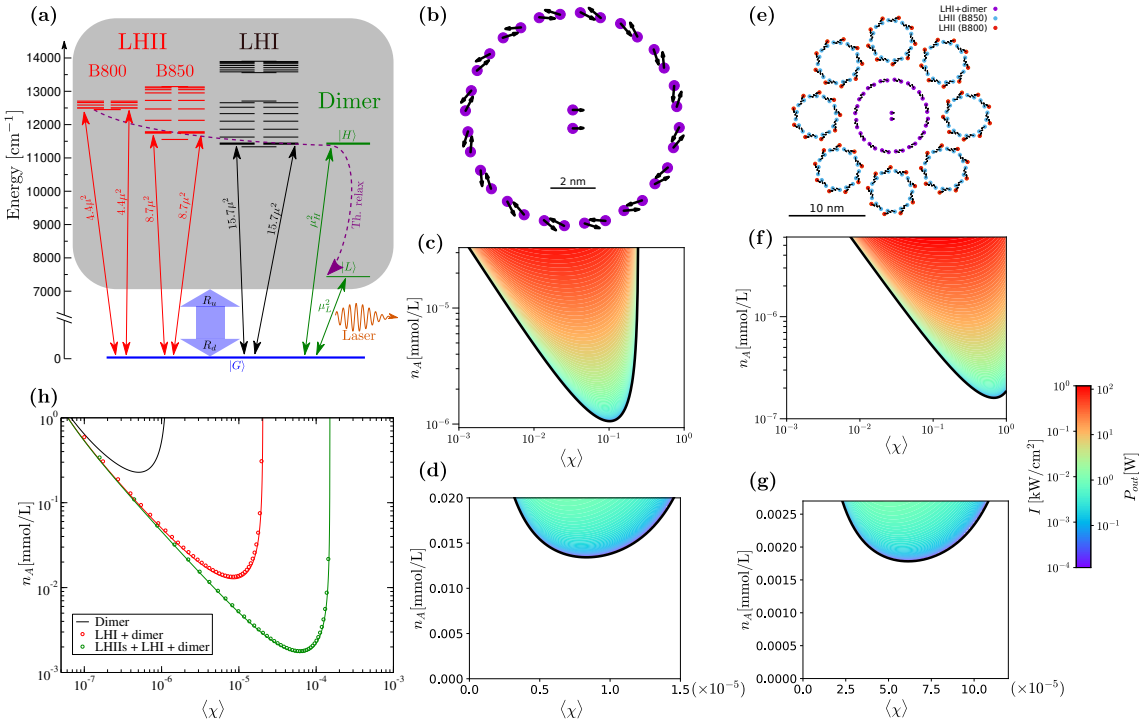

Figure 5.3: A results figure from the collaborative manuscript that came from this project [59]. a) Schematic of ground and single-excitation manifold eigenstates for the dimer, LHI, LHII system. b), e) Schematics of the dipole positions and orientations for the two proposed molecular aggregates with an H-dimer replacing the reaction centre in the middle of an LHI ring. c), d). f), g) The power output and lasing intensity of the two proposed aggregates as the density of aggregates, n_A, and $\langle\chi\rangle$, are varied. The black bounding lines denote the lasing threshold. The top two panels consider concentrated sunlight, using a blackbody at 3000 K, whereas the bottom two show operation under natural sunlight. h) The three curves display the lasing threshold density under natural sunlight for the two proposed molecular aggregates and the bare H-dimer. The circles are taken from a full analysis using all of the states shown in panel a), whereas the continuous lines are calculated with a reduced two level lasing model and rescaling the pumping to account for the additional antennae.

5.2 Isolated dimer

5.2.1 Model

5.2.1.1 Dimer Geometry

The original focus of this project centred on the feasibility of lasing in a molecular dimer. We consider two identical absorbers, modelled as 2LSs, with dipole moment

$\boldsymbol{d}$, in close proximity. A Hamiltonian describing the dimer system can then be written using the standard Pauli spin operator definitions as ($\hbar = 1$)

$$\hat{H}_{\text{dim}} = \omega_A \sum_{i=1}^{2} \hat{\sigma}_i^z + \sum_{i,j=1}^{2} J_{i,j}(\boldsymbol{r}_{i,j})(\hat{\sigma}_i^+ \hat{\sigma}_j^- + \hat{\sigma}_i^- \hat{\sigma}_j^+) \ , \tag{5.5}$$

where ω_A is the 2LS energy splitting, and J is the induced Förster-type dipole-dipole coupling [78, 79],

$$J_{i,j}(\boldsymbol{r}_{i,j}) = \frac{1}{4\pi\epsilon_0 |\boldsymbol{r}_{i,j}|^3} \left(\boldsymbol{d}_i \cdot \boldsymbol{d}_j - \frac{3(\boldsymbol{r}_{i,j} \cdot \boldsymbol{d}_i)(\boldsymbol{r}_{i,j} \cdot \boldsymbol{d}_j)}{|\boldsymbol{r}_{i,j}|^2} \right) . \tag{5.6}$$

The typical level structure for the eigenstates of such a dimer is shown in Fig. 5.4. The four energy levels represent the fully ($|F\rangle$) excited, higher ($|H\rangle$) and lower ($|L\rangle$) single excitation states, and finally the ground state ($|G\rangle$). Due to the close proximity of the absorbers, we can assume a shared optical bath, with collective optical interaction Hamiltonian [66], to determine how optical processes link the eigenstates of neighbouring excitation manifolds. When we examine the three-vector dipole components of each optical process, we find transitions which link to the $|H\rangle$ state use one polarisation, while those connected to $|L\rangle$ use an orthogonal polarisation. We can refer to these respectively as the H and L polarisations. The directions of H and L are determined by the alignment of the dipoles of the two 2LSs.

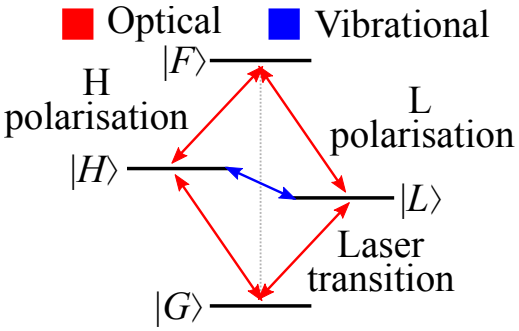

Figure 5.4: Schematic of the eigenstates of the dimer system. Optical (red) processes link eigenstates in neighbouring excitation manifolds, while vibrational (blue) processes link the $|H\rangle$ and $|L\rangle$ eigenstates in the single excitation manifold. Optical processes on the left and right side of the grey line use orthogonal polarisations.

The N^2 superabsorbing and superradiating optical behaviour discussed in Chapter 2 cannot be exhibited by a dimer, as it does not have enough excitation steps. A dimer can still exhibit single photon collective effects [5, 6, 7]; a single excitation in a dimer could potentially relax to the ground state twice as fast as would be expected from a single 2LS. This assumes that all of the dipole strength is concentrated on

one of the two possible optical transitions, since

$$\boldsymbol{d}_H \cdot \boldsymbol{d}_H + \boldsymbol{d}_L \cdot \boldsymbol{d}_L = 2|\boldsymbol{d}_{2\mathrm{LS}}| \ . \tag{5.7}$$

where $\boldsymbol{d}_H$, $\boldsymbol{d}_L$, and $\boldsymbol{d}_{2\mathrm{LS}}$ are the dipole moments respectively for the $|H\rangle$ and $|L\rangle$ transitions as well as a single absorber. The parameter we use to describe this weighting of dipole moments is χ, defined as

$$\boldsymbol{d}_L \cdot \boldsymbol{d}_L = \chi|\boldsymbol{d}_{2\mathrm{LS}}| \ , \tag{5.8}$$

$$\boldsymbol{d}_H \cdot \boldsymbol{d}_H = (2-\chi)|\boldsymbol{d}_{2\mathrm{LS}}| \ . \tag{5.9}$$

One can therefore envision pumping a dimer via the H polarisation. Assuming the energetic splitting between $|H\rangle$ and $|L\rangle$ is large compared to thermal energy at room temperature (~ 25 meV), rapid, one-way relaxation via phonon modes can be assumed to move any population in the first excitation manifold to the $|L\rangle$ state. Optical relaxation from $|L\rangle$ could then act as a lasing transition to populate a field in a cavity parallel to the L polarisation.

We begin with how the dipole-dipole coupling, J [78, 79], which governs the splitting between the two single excitation states, varies as the geometry is changed. We consider that we have precise control over the 2LS orientation and positioning, and then move our absorbers around each other with two angles, a dimer incline angle, θ_{DIA}, and a zenith angle, θ_{zen} (Figs. 5.5 and 5.6). These two angles are varied between 0 and $\pi/2$. For these results, since we are only looking at the relative behaviour, the choice of exact dipole parameters is not relevant.

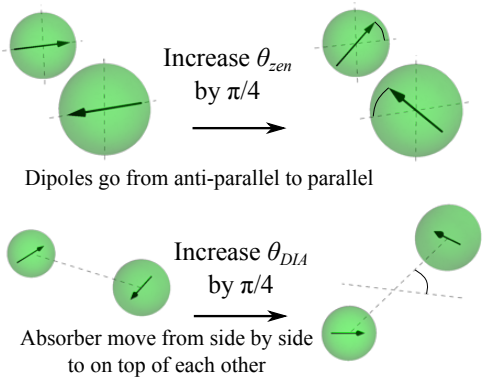

Figure 5.5: Schematic of the two key angles we consider when moving dimers, θ_{zen} and θ_{DIA}. Increasing θ_{zen} turns the dipole moments from anti-parallel towards a parallel setup, while increasing θ_{DIA} rotates the dimer so the dipoles move from side-by-side to a stacked arrangement.

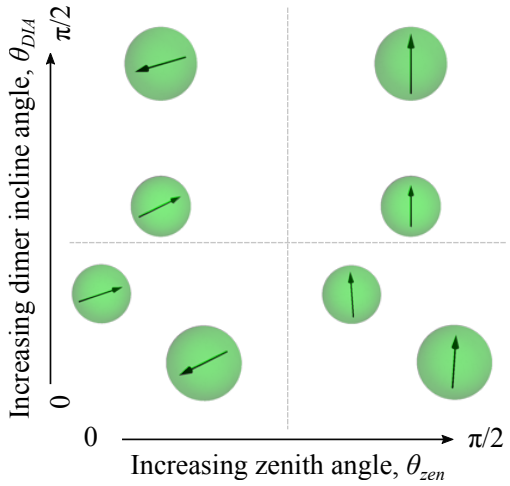

Figure 5.6: Schematic showing how the geometry of our dimer changes as we change our two key angles, θ_{DIA} and θ_{zen}. The 2LSs start side-by-side and anti-parrallel. Increasing θ_{DIA} moves one above the other, while increasing θ_{zen} causes the dipoles to angle upwards towards a shared parallel direction.

In Fig. 5.7 we see how the changing of the two angles affects the induced coupling, J, as well as the strengths of the dipole components of the two sets of optical transitions. limits are not included on the data range, as this is just a factor of the dipole strength of the two 2LSs and their separation. Changing those parameters would change the minimum and maximum values on the left hand colour bar, but the plot would look the same. One can see that as the coupling changes between negative and positive the symmetric and antisymmetric eigenstates ordering changes. This means the polarisations associated with $|H\rangle$ and $|L\rangle$ as well as their associated dipole strengths swap.

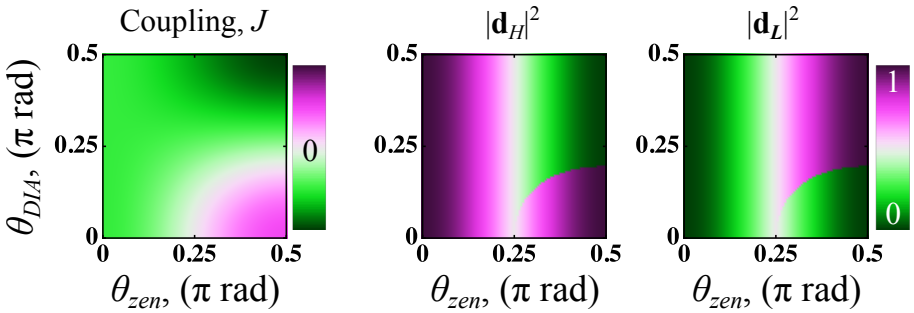

Figure 5.7: Left: Plot of how the coupling between absorbers varies over the angular parameter scan. The behaviour of the coupling, J, changing from positive to negative depends only on the 2LS geometry, but the magnitude of the minimum and maximum coupling values depends on 2LS brightness and separation. Right: Plot of how the two eigenstate dipole strengths vary over the same parameter scan when the total dipole is normalised to 1.

While our model allows for the variation of our two angles to cover the full parameter space in Fig. 5.7, for the sake of reducing the number of parameters of concern we fix θ_{DIA} to $\pi/2$, and relabell θ_{zen} as θ. This means that there is only a doubling effect on the coupling, J, as θ is moved between the minimum and maximum values. This restriction also means we do not need to consider the regime where a small J will restrict the splitting between $|H\rangle$ and $|L\rangle$, suppressing the effectiveness of the phonon relaxation between the two. As long as θ is small we are in the region of interest for an H-dimer that could exhibit lasing.

It should also be noted that unlike the previous chapters, where the optical properties of dipoles were used to calculate the system Hamiltonian, in this project we often define a system Hamiltonian term first, and then reverse-engineer the necessary dipole parameters. From hereon our starting point for optical parameters are inspired from H-dimers [177], these are summarised in Tab. 5.1.

ω_A	τ_L	θ	J
1.17 eV	36.8 ns	0.07 rad	2000 $\text{cm}^{-8} = 0.25$ eV

Table 5.1: Parameters we commonly used as a starting point for parameter scans throughout this work. Similar to values typical of H-dimers [177].

5.2.1.2 Optical and Vibrational Baths

We use a collective weakly-coupled photon bath to model absorption and emission associated with incoherent sunlight. Absorption via a bright transition acting as a pump our lasing scheme. Absorption and relaxation rates are calculated following the steps laid out i. Local phonon baths are also weakly-coupled to each of the absorbers in the dimer. Dissipators for both of these processes are formed following the steps laid out in Chapter 1. The shared quantum optical interaction Hamiltonian is [66]

$$\hat{H}_{I,\text{opt}} = \sum_{i=1}^{2} \boldsymbol{d}_i \hat{\sigma}_i^x \otimes \sum_k f_k(\hat{a}_k + \hat{a}_k^\dagger) \ , \tag{5.10}$$

and the interaction matrix for the local vibrational baths on each 2LS in the dimer is

$$\hat{H}_{I,\text{vib}} = \sum_{i=1}^{2} \hat{\sigma}_i^z \otimes \sum_q g_{i,q}(\hat{b}_{i,q} + \hat{b}_{i,q}^\dagger) \ . \tag{5.11}$$

The photon rates are determined by the choice of dipole parameters for the absorbers, using a flat spectral density as was the case in the previous chapters. We consider three different temperatures for calculating Bose-Einstein occupancy values for the photon bath:

- 5800 K, the blackbody temperature of the sun;

- 3000 K, the blackbody temperature that can be achieved with concentrated sunlight [157];
- 5800 K, but with a factor of 5.4×10^{-6} applied to the Bose-Einstein occupancy values. This prefactor accounts for the solid angle of the Sun as observed from the Earth, and is similar to the optical concentration adjustments made in Chapter 3. We refer to this as '1 sun' illumination.

Phonon rates are set such that the relaxation time between $|H\rangle$ and $|L\rangle$ is 1 ps at 0 K for a dimer with parameters $J = 2000$ cm^{-1} $= 0.25$ eV, we assume a flat phonon spectral density, so in the vibrational environment correlation terms $\Gamma_{nm}(\omega) = \frac{1}{2}\kappa_{\text{vib}}\omega(1 + n(\omega))$ we end up defining $\kappa_{\text{vib}} = 1.3 \times 10^{-3}$ (unitless). The reason for these choices is that this is the typical timescale for phonon processes, and we do not possess more detailed information about our vibrational environment without being more specific about our choice of system. In Fig. 5.8 we show that the timescale of evolution for the populations of, and dephasing between, states connected by phonons, is indeed picoseconds in a dimer system identical to what was considered in Ref. [59] and coupled only to phonon baths with an initial state given by

$$\begin{pmatrix} 0 & 0 & 0 & 0 \\ 0 & 0.5 & 0.5 & 0 \\ 0 & 0.5 & 0.5 & 0 \\ 0 & 0 & 0 & 0 \end{pmatrix} . \tag{5.12}$$

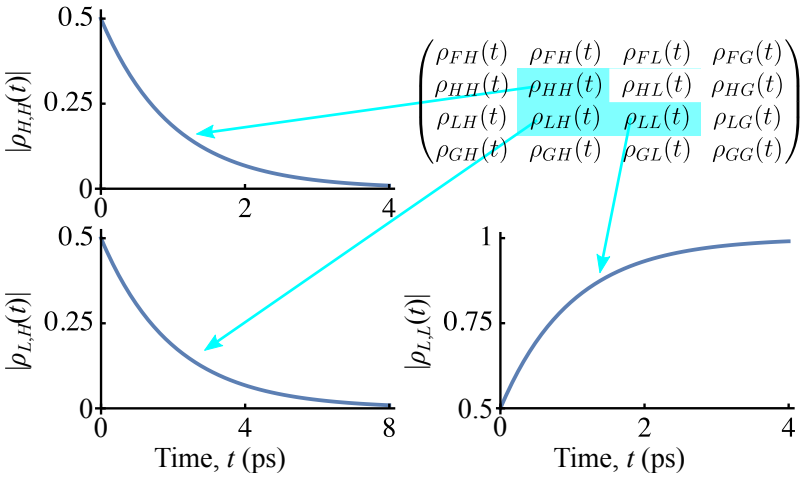

Figure 5.8: Plots of the density matrix component evolution for the populations of, and coherence between $|H\rangle$ and $|L\rangle$. The dimer is only connected to independent phonon baths. The timescale for the relaxation of population in the single excitation manifold and for dephasing between $|H\rangle$ and $|L\rangle$ are both on the order of picoseconds. The dimer parameters are summarised in Tab. 5.1. The initial density matrix is given by Eq. 5.12.

With these parameters set we can calculate the evolution of a dimer outside of a cavity with

$$\frac{d}{dt}\rho_S = -i[\hat{H}_{\text{dim}}, \rho_S] + \mathcal{D}_{\text{opt}} + \mathcal{D}_{\text{vib}} \ , \tag{5.13}$$

where $\mathcal{D}_{\text{opt}}$ and $\mathcal{D}_{\text{vib}}$ are Bloch-Redfield dissipators. We can then calculate either the evolution or the steady state of the dimer density matrix.

5.2.2 Results

To establish the validity of the simplified model (Eq. 5.1) we solve for the steady-state of the dimer with our full four level, Bloch-Redfield approach without making the assumptions of instant phonon thermalisation and discarding higher excitation states, which is used there to reduce a multi-site system down to two states.

In Fig. 5.9 we plot the populations of all four dimer states at the steady-state by solving Eq. 5.13. A parameter scan is performed by varying the dipole-dipole coupling, J (which is benchmarked against the thermal energy at room temperature, 300 K), and relative dipole strength of the lower energy state. The scan is performed at all three optical bath temperatures, and in each case we can see it is possible to achieve population inversion with large enough J and weak enough relative brightness for $|L\rangle$. The figure also shows the top two states can always be neglected, supporting the approximations made when producing the reduced 2LS analytical model of Eq. 5.1.

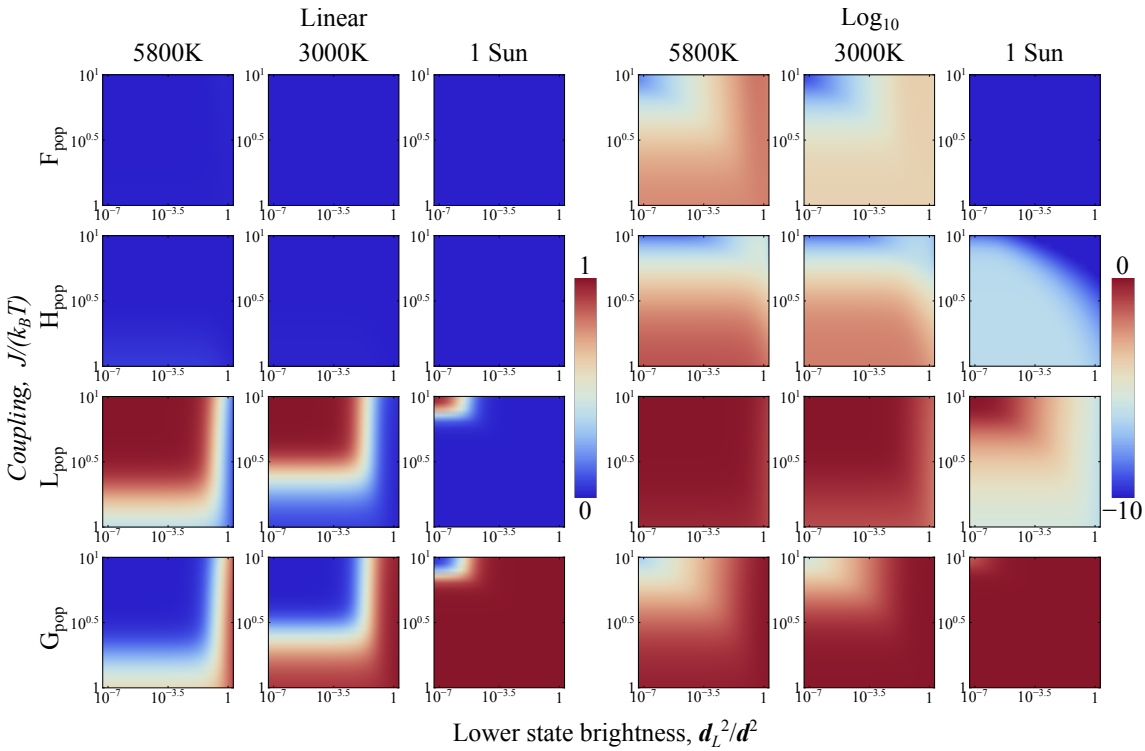

Figure 5.9: Total population of all four states of the dimer system at the steady-state, solving with the Bloch-Redfield approach (Eq. 5.13). A linear scale on the colour bar (left panels) is used to show population inversion in the lower states, while a logarithmic scale (right panels) shows the order of magnitude of the population in the higher energy states. The dipole parameters are summarised in Tab. 5.1. Phonon bath at 300 K, and phonon decay rate defined to match a picosecond spontaneous decay rate for $\theta = 0.07$ rad (Fig. 5.8). Comparison of cases with photon bath at 5800 K, 3000 K, and '1 sun' illumination.

Having established that the reduction to a two level system is generally valid, we now investigate the quantitative differences between our four level Bloch-Redield model and the reduced two level model (Eq. 5.1). In Fig. 5.10 we plot both the population difference, D_{eq}, produced by the two approaches in the top panels, as well as the difference between the results beneath. As was the case in Fig. 5.9, the results are calculated using three different temperature for the phonon bath. While there are some small differences visible in the lower panels, the Bloch-Redfeld model results do support those found with the reduced two level approach.

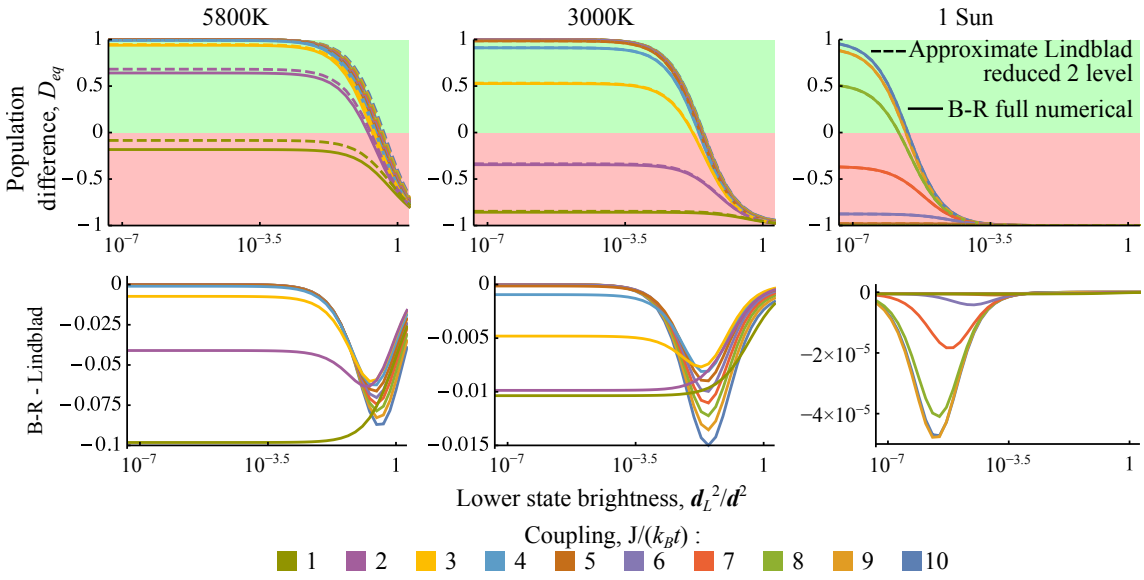

Figure 5.10: Comparison between the approximate steady-state solution given by Eq. 5.1 and the exact solution of Eq. 5.13 for different values of the coupling, $\Omega/(k_B T)$ (with $T = 300$ K), and lower state brightness. Shown below: the differences between the results of the two methods. Dimer parameters are summarised in Tab. 5.1. Phonon bath at 300 K, and phonon decay rate defined to match a picosecond thermal relaxation time (Fig. 5.8). Comparison of cases with photon bath at 5800 K, 3000 K, and '1 sun'.

5.3 Adding phenomenological dephasing

5.3.1 Model

While the master equation in Eq. 5.13 does introduce dephasing between the states coupled by phonons, $|H\rangle$ and $|L\rangle$ causing the decay of $\rho_{L,H}(t)$ visible in Fig. 5.8, it only induces dephasing between the ground state and single-excitation manifold on timescales on the order of optical processes. However, such a dephasing (between the excited and ground states either side of their lasing transition) needs to be faster than the Rabi frequency of the optical dipoles in the cavity laser field, so as to induce incoherent, rather than coherent, exchange of photons between the dimer and the cavity.

Rather than changing the model to treat the laser with a quantum approach, which would require scaling up the Hilbert space to include the cavity, we instead chose to introduce the expected dephasing behaviour with phenomenological Lindblad dissipators. In our dimer eigenbasis,

$$\{\, |F\rangle\,,\ |H\rangle\,,\ |L\rangle\,,\ |G\rangle\,\}\,, \tag{5.14}$$

we define the following dephasing operators:

$$\begin{pmatrix} 1 & 0 & 0 & 0 \\ 0 & -1 & 0 & 0 \\ 0 & 0 & 0 & 0 \\ 0 & 0 & 0 & 0 \end{pmatrix}, \begin{pmatrix} 1 & 0 & 0 & 0 \\ 0 & 0 & 0 & 0 \\ 0 & 0 & -1 & 0 \\ 0 & 0 & 0 & 0 \end{pmatrix}, \begin{pmatrix} 1 & 0 & 0 & 0 \\ 0 & 0 & 0 & 0 \\ 0 & 0 & 0 & 0 \\ 0 & 0 & 0 & -1 \end{pmatrix},$$

$$\begin{pmatrix} 0 & 0 & 0 & 0 \\ 0 & 1 & 0 & 0 \\ 0 & 0 & 0 & 0 \\ 0 & 0 & 0 & -1 \end{pmatrix}, \begin{pmatrix} 0 & 0 & 0 & 0 \\ 0 & 0 & 0 & 0 \\ 0 & 0 & 1 & 0 \\ 0 & 0 & 0 & -1 \end{pmatrix}. \tag{5.15}$$

There is no operator which covers the single-excitation states, as the this is already covered by the inclusion of the phonon dissipator. The new dephasing dissipator takes the form

$$\mathcal{D}_\phi[\rho] = \frac{2}{7}\Gamma_\phi \sum_k \hat{L}_k \rho \hat{L}_k^\dagger - \frac{1}{2}\{\hat{L}_k^\dagger \hat{L}_k, \rho\} , \tag{5.16}$$

where $\hat{L}_k$ are the dephasing interaction operators, and Γ_ϕ is the dephasing rate. The factor of $\frac{2}{7}$ ensures that the decay of the coherence term linking the two states connected by the lasing transition, $\rho_{G,L}(t)$, matches the timescale of $1/\Gamma_\phi$. This definition allows both the four level Bloch-Redfield model and reduced two level model to use the same dephasing rate, Γ_ϕ.

5.3.2 Results

In Fig. 5.11 we plot the evolution of $\rho_{G,L}(t)$ calculated with the exteded master equation,

$$\frac{d}{dt}\rho_S = -i[\hat{H}_{\text{dim}}, \rho_S] + \mathcal{D}_{\text{opt}} + \mathcal{D}_{\text{vib}} + \mathcal{D}_\phi , \tag{5.17}$$

with three different timescales for dephasing, as well as a no dephasing (infinite timescale) case against both linear and logarithmic time. The plots show that without the phenomenological dephasing included the decoherence naturally occurs at optical timescales, and once included, the $1/e$ decay time lines up with the choice of Γ_ϕ as expected.

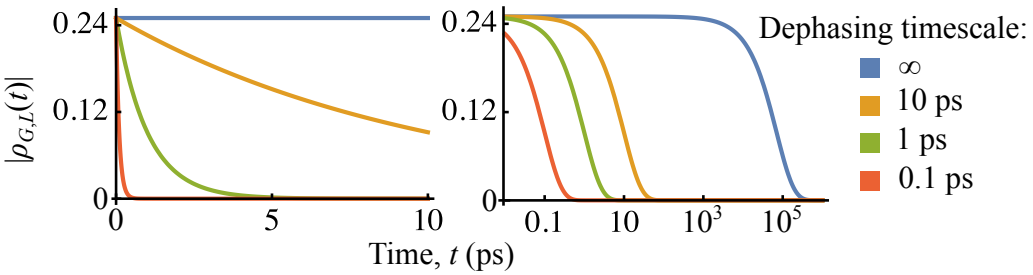

Figure 5.11: Plots of the decay of the $\rho_{G,L}(t)$ coherence term in a dimer only connected to a 3000 K photon bath for solar proccesses and local phonon baths. Phenomenological dephasing operators are added at varying rates and this produces the expected decay on picosecond timescales. The parameters are summarised in Tab. 5.1.

5.4 Including a semi-classical field

5.4.1 Moving to a rotating frame

Having shown agreement for the dissipative behaviour of both our four level, Bloch-Redfield model, and the simplified two level model, and then included dephasing terms consistently across both, we shall now expand our model to include coupling to a laser field inside a resonant cavity. The dimer needed to be coupled to a cavity mode ω_c, which is chosen to match the eigenenergy of $|L\rangle$, namely ω_L, making it degenerate with the transition energy of the lasing transition.

To couple the field to the dimer we begin with the laboratory frame dimer Hamiltonian and add time-dependent elements of the form $\boldsymbol{d}_i \cdot \boldsymbol{E}(t)$, thereby assuming a semi-classical field with a many-photon coherent state, where $\boldsymbol{E}(t) = \boldsymbol{E}_0 \cos(\omega_L t)$:

$$\hat{H} = \begin{pmatrix} 2\omega_A & \boldsymbol{d}_1 \cdot \boldsymbol{E}_0 \cos(\omega_L t) & \boldsymbol{d}_2 \cdot \boldsymbol{E}_0 \cos(\omega_L t) & 0 \\ \boldsymbol{d}_1 \cdot \boldsymbol{E}_0 \cos(\omega_L t) & \omega_A & J & \boldsymbol{d}_1 \cdot \boldsymbol{E}_0 \cos(\omega_L t) \\ \boldsymbol{d}_2 \cdot \boldsymbol{E}_0 \cos(\omega_L t) & J & \omega_A & \boldsymbol{d}_2 \cdot \boldsymbol{E}_0 \cos(\omega_L t) \\ 0 & \boldsymbol{d}_1 \cdot \boldsymbol{E}_0 \cos(\omega_L t) & \boldsymbol{d}_2 \cdot \boldsymbol{E}_0 \cos(\omega_L t) & 0 \end{pmatrix}. \tag{5.18}$$

The $\boldsymbol{d}_1 \cdot \boldsymbol{E}_0$ and $\boldsymbol{d}_2 \cdot \boldsymbol{E}_0$ terms account for the alignment of the absorber dipole moments with the orientation of the cavity mode containing the field, and are respectively now relabelled to E_1 and E_2. We then choose the unitary transformation matrix

$$\hat{U} = \begin{pmatrix} e^{i2\omega_L t} & 0 & 0 & 0 \\ 0 & e^{i\omega_L t} & 0 & 0 \\ 0 & 0 & e^{i\omega_L t} & 0 \\ 0 & 0 & 0 & 1 \end{pmatrix}, \tag{5.19}$$

to move to a frame rotating at the frequency of the lasing transition with the trans-

formed (prime) Hamiltonian given by

$$\hat{H}' = \hat{U}\hat{H}\hat{U}^\dagger + i\hat{U}\frac{d\hat{U}^\dagger}{dt} \ . \tag{5.20}$$

The transformation gives

$$\hat{H}' = \begin{pmatrix} 2\omega_A - 2\omega_L & \frac{E_1}{2}(1+e^{i2\omega_L t}) & \frac{E_2}{2}(1+e^{i2\omega_L t}) & 0 \\ \frac{E_1}{2}(1+e^{-i2\omega_L t}) & \omega_A - \omega_L & J & \frac{E_1}{2}(1+e^{i2\omega_L t}) \\ \frac{E_2}{2}(1+e^{-i2\omega_L t}) & J & \omega_A - \omega_L & \frac{E_2}{2}(1+e^{i2\omega_L t}) \\ 0 & \frac{E_1}{2}(1+e^{-i2\omega_L t}) & \frac{E_2}{2}(1+e^{-i2\omega_L t}) & 0 \end{pmatrix} . \tag{5.21}$$

We then drop the fast oscillating terms (oscillating at twice the lasing frequency) to leave

$$\hat{H}' \approx \begin{pmatrix} 2\omega_A - 2\omega_L & \frac{E_1}{2} & \frac{E_2}{2} & 0 \\ \frac{E_1}{2} & \omega_A - \omega_L & J & \frac{E_1}{2} \\ \frac{E_2}{2} & J & \omega_A - \omega_L & \frac{E_2}{2} \\ 0 & \frac{E_1}{2} & \frac{E_2}{2} & 0 \end{pmatrix} . \tag{5.22}$$

The next step is to move to the eigenbasis of the dimer. If we temporarily drop the field terms we have

$$\hat{H}'_S = \begin{pmatrix} 2\omega_A - 2\omega_L & 0 & 0 & 0 \\ 0 & \omega_A - \omega_L & J & 0 \\ 0 & J & \omega_A - \omega_L & 0 \\ 0 & 0 & 0 & 0 \end{pmatrix} , \tag{5.23}$$

which diagonalises (tilde) to (using $\omega_L = \omega_A - |J|$)

$$\begin{aligned} \hat{\tilde{H}}'_S &= \begin{pmatrix} 2\omega_A - 2\omega_L & 0 & 0 & 0 \\ 0 & \omega_A - \omega_L + |J| & 0 & 0 \\ 0 & 0 & \omega_A - \omega_L - |J| & 0 \\ 0 & 0 & 0 & 0 \end{pmatrix} , \\ &= \begin{pmatrix} 2|J| & 0 & 0 & 0 \\ 0 & 2|J| & 0 & 0 \\ 0 & 0 & 0 & 0 \\ 0 & 0 & 0 & 0 \end{pmatrix} . \end{aligned} \tag{5.24}$$

In the rotating frame, the two lower energy states $|L\rangle$, and $|G\rangle$ have become degenerate since they are linked by a transition which is driven by the resonant lasing field in the cavity.

The final step is to move the field components,

$$\begin{pmatrix} 0 & \frac{E_1}{2} & \frac{E_2}{2} & 0 \\ \frac{E_1}{2} & 0 & 0 & \frac{E_1}{2} \\ \frac{E_2}{2} & 0 & 0 & \frac{E_2}{2} \\ 0 & \frac{E_1}{2} & \frac{E_2}{2} & 0 \end{pmatrix} , \tag{5.25}$$

to the newfound dimer diagonal basis, becoming

$$\frac{1}{\sqrt{8}} \begin{pmatrix} 0 & E_1 + E_2 & \frac{J}{|J|}(-E_1 + E_2) & 0 \\ E_1 + E_2 & 0 & 0 & E_1 + E_2 \\ \frac{J}{|J|}(-E_1 + E_2) & 0 & 0 & \frac{J}{|J|}(-E_1 + E_2) \\ 0 & E_1 + E_2 & \frac{J}{|J|}(-E_1 + E_2) & 0 \end{pmatrix} . \tag{5.26}$$

The general Hamiltonian for the field-coupled dimer in the rotating frame is therefore

$$\hat{H}'_{D-F} = \begin{pmatrix} 2\omega_A - 2\omega_L & g_h E_0 & g_l E_0 & 0 \\ g_h E_0 & \omega_A - \omega_L & J & g_h E_0 \\ g_l E_0 & J & \omega_A - \omega_L & g_l E_0 \\ 0 & g_h E_0 & g_l E_0 & 0 \end{pmatrix} , \tag{5.27}$$

where g_l and g_h are coupling terms and E_0 is the absolute value of the initial field in the cavity. The master equation for system evolution is then updated to use this Hamiltonian:

$$\frac{d}{dt}\rho_S = -i[\hat{H}'_{D-F}, \rho_S] + \mathcal{D}_{\text{opt}} + \mathcal{D}_{\text{vib}} + \mathcal{D}_{\phi} . \tag{5.28}$$

We note that the optimal dimer ordered setup occurs when $\boldsymbol{d}_1 \cdot \boldsymbol{E}_0 = -\boldsymbol{d}_2 \cdot \boldsymbol{E}_0$, leading to $g_h = 0$ and $g_L E_0 = |\boldsymbol{d}_L| E_0/2$.

5.4.2 Static field

While the most complete version of our model considers a cavity field that is coupled dynamically to the molecular aggregates, considering the coupling of an ensemble of molecular aggregates with a non-evolving static field allows us to focus on a few more subtle behavioural aspects. For example, though the cavity is tuned to the frequency of the laser transition, and the detuning between ω_L and ω_H should prevent further excitation to $|F\rangle$, a strong enough coupling to the laser field could overcome this frequency selectivity.

To investigate this we performed a parameter scan using Eq. 5.28. We assume an ideally aligned cavity with the L polarisation, so there is no coupling to the field via the H polarisation ($g_h = 0$). The matter of a disordered setup with non-zero g_h is investigated later with the variable field model. To vary system the Hamiltonian

with the static field intensity we use

$$g_l E_0 = 2\frac{|\boldsymbol{d}|}{\sqrt{\epsilon_0 c}} \sin\theta \sqrt{I(\infty)} \ , \tag{5.29}$$

where (using our assumed default dipole parameters)

$$\frac{|\boldsymbol{d}|}{\sqrt{\epsilon_0 c}} = 4.106 \times 10^{-9} \frac{\text{eV}}{(\text{W/m}^2)^{1/2}} \ . \tag{5.30}$$

In Fig. 5.12 we plot the results of the parameter scans for the steady state populations using both linear and logarithmic scaling. The intensity of the coupled static field, I, and the dimer angle θ are varied across the parameter scan. The different dephasing rates from Fig. 5.11 are used, and show that stronger dephasing increases the minimum intensity at which point the choice of θ is irrelevant for population inversoin, but for small enough θ inversion can occur at any intensity. We can see that for large intensity values the frequency selectivity can be overcome, causing a second excitation, meaning $|F\rangle$ can no longer be ignored. This dictates a limit on the validity of the reduced two level approach, but the intensity where this breakdown occurs is much larger than is observed and considered in any other results in this project.

We also note that there is a minimum intensity level, below which behaviour is dominated by the phonon and photon dissipators rather than the coupling to the cavity. Once the cavity coupling takes over, population is evenly distributed between the states coupled by lasing transitions, namely $|G\rangle$, $|L\rangle$ and occasionally $|F\rangle$.

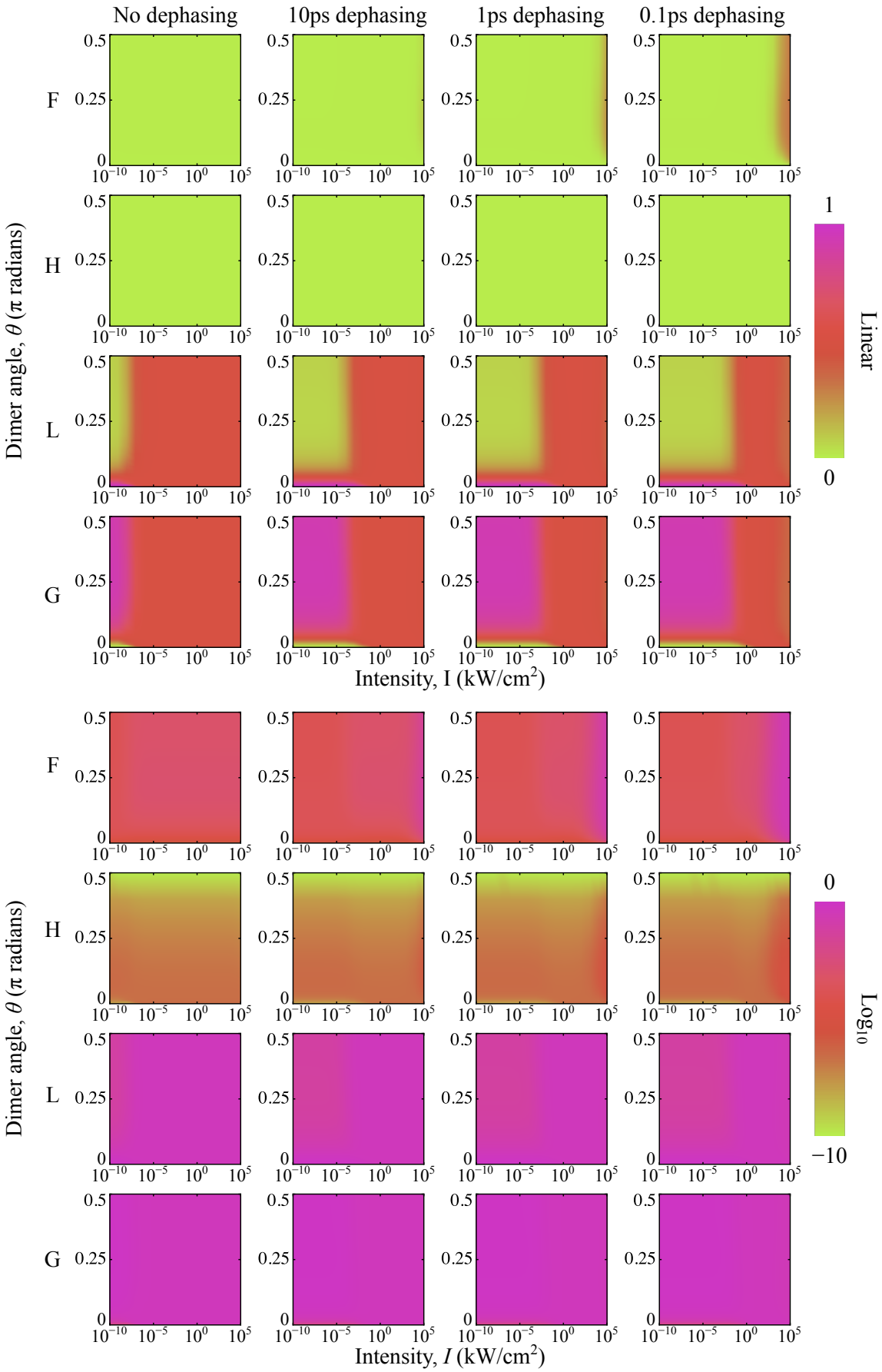

Figure 5.12: State populations using the static field model. The intensity of the coupled static field, I, and the dimer angle θ are varied across the parameter scan. The parameters otherwise match those used in Fig. 5.8.

5.4.3 Variable field

The final development for the dimer model was to use Eq. 5.28, but to couple with a variable field with a loss rate, κ. We also used this model to consider a collection of dimers in the cavity.

We model an ensemble of dimers by explicitly modelling a single dimer, which acts as an average for the ensemble. In a randomised ensemble some dimers will be aligned such that their L polarisation is parallel with the cavity as would be ideal, but some will have their H polarisation parallel with the field, or even have both optical polarisation axes perpendicular to the cavity. To model this disordered ensemble with our average dimer, we couple it to the field via both polarisations, and then reduce the coupling strength by a factor of $\sqrt{3}$ to account for the averaging of all the dimers over 3-D space, meaning one would expect the dipole moment for each coupling to be reduced to $\boldsymbol{d}_H^2/3$ and $\boldsymbol{d}_L^2/3$. The new field coupling terms are also proportional to the number of dimers in the ensemble.

The equation for the evolution was derived from Ref. [178]:

$$\frac{dE_0(t)}{dt} = -\frac{\kappa E_0(t)}{2} - i\alpha n_A\big[g_H(\rho_{F,H}(t) + \rho_{H,G}(t)) + g_L(\rho_{F,L}(t) + \rho_{L,G}(t))\big] \ . \quad (5.31)$$

The coupling terms are defined as $g_{L,H} = |\boldsymbol{d}_{L,H}|/(2\sqrt{3})$, and the pre-factor is $\alpha = 2\omega_L/\epsilon_0$.

By simultaneously solving Eq. 5.28 and Eq. 5.31 we find the evolution for both the dimer states and the field, the absolute value of which can be used to determine the laser intensity. In Fig. 5.13 the evolution of the intensity is plotted using the different dephasing timescales used in Fig. 5.11. It should be noted that the molecular densities are increased as the dephasing timescales are decreased to maintain the balance of parameters for incoherent exchange between the dimers and cavity. The initial state for the system is

$$\rho(t=0) = \begin{pmatrix} 0 & 0 & 0 & 0 \\ 0 & 0 & 0 & 0 \\ 0 & 0 & 0.5 & 0 \\ 0 & 0 & 0 & 0.5 \end{pmatrix} \ , \quad (5.32)$$

and $E_0(t=0) = 868$ Vm^{-1}, noting that an initial state with no field would require the off-diagonal elements in the initial density matrix to be non-zero. The field intensity settled on a steady state value in all of the scenarios except the case with no dephasing, where the intensity continued to rapidly oscillate over the observed timescale.

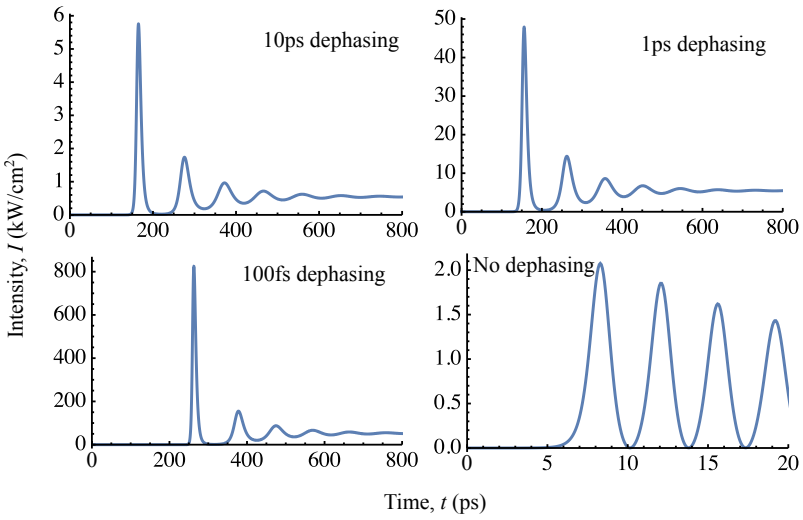

Figure 5.13: Plots of the intensity evolution for a field coupled to a disordered ensemble of dimers. Four different dephasing cases are used, and the density of dimers is changed across them. For dephasing timescales of $\{\infty$, 10 ps, 1 ps, 100 fs$\}$, the respective values of n_A are $\{3 \times 10^{14}$ cm^{-3}, 3×10^{14} cm^{-3}, 3×10^{15} cm^{-3}, 3×10^{16} cm$^{-3}\}$. The field loss rate, κ, is set to 50 MHz (2×10^{-7} eV). The parameters otherwise match those used in Fig. 5.8.

Figure 5.14 is taken from the supplement of our manuscript [59], but displays the results of full Bloch-Redfield coherent laser model (black line), side-by-side with the results of the reduced two level approach, which provides a steady state value (blue dashed), as well as a third approach which was based on incoherent lasing equations (red dashed). Dimer state populations are plotted on the left (the two level hybrid excited state being approximated as $|L\rangle$), and the intensity is plotted on the right. The additional final approach relies on having large enough dephasing to dominate the Rabi frequency to induce coherent exchange between the field and the dimer, and this is supported by the stronger agreement in the results for the faster dephasing time. The slower 10 ps dephasing time results still show agreement in the steady state, but early dynamics are slightly shifted.

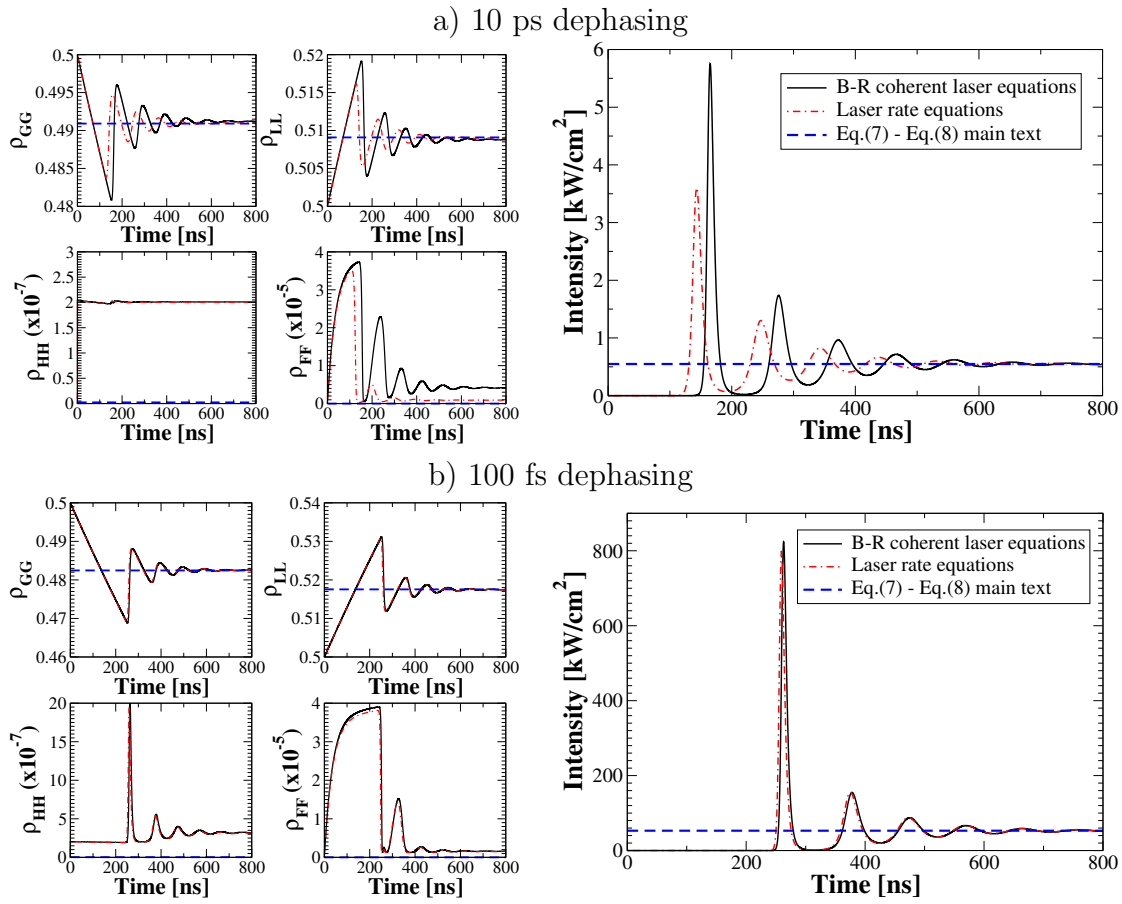

Figure 5.14: Figure components from the supplement of the collaborative manuscript [59]. The figure displays the agreement in steady state between the Bloch-Redfield coherent laser model (black line), and the reduced two level approach (blue dashed). We can also see that for adequately strong dephasing one can model the behaviour entirely using incoherent laser equations(red dashed) . The parameters match those used in Fig. 5.13.

5.5 Conclusions

In this chapter we developed a variety of models looking at the open systems behaviour of a molecular H-dimer. Beginning with an isolated dimer, we established that with adequate control of the dipole geometry and optical parameters a dimer could produce population inversion under the dissipative effects of a shared optical bath and local phonon baths. Inversion was found to rely on the combination of relative darkness in the dipole transition moments linking the two single-excitation manifold states to the ground state, alongside the rapid relaxation into vibrational modes. The interactions with these baths were modelled with a Bloch-Redfield formalism [66]. After adding phenomenological dephasing dissipators we then coupled a cavity to the dimer to see if lasing could be achieved.

This work supported a collaborative project which looked at modelling the lasing

potential of groups of molecular aggregates. Using our tractable, but more detailed and physically rigorous model for a dimer, we were able to establish potential limitations on the use cases after the approximations that were made to allow modelling of larger systems which would be too computationally demanding for our approach. Outside of these limiting cases we were able to find very good agreement between our two approaches.

After using our model to establish confidence in the newly derived equations for lasing in molecular aggregates, it is possible to investigate the potential lasing performance of proposed molecular structures. Two existing examples are the hybrid H-dimer-LHI-LHII systems proposed in Ref. [59], as well as using green sulphur bacteria [179], with the H-dimer. These additional antennae can increase the absorption cross-section, thereby reducing the demands on the dimer design to achieve adequate relative darkness for population inversion, while minimising the need for sunlight concentration to cross the lasing threshold, opening the possibility for achieving sunlight-pumped lasing under '1 sun' illumination. By changing the surrounding molecular aggregates, for example to photosystem II [180], one can change the regions of the solar spectrum feeding excitations into the excited state of the H-dimer, providing the potential for a lot of flexibility in the designing of the laser behaviour, assuming adequate control of design of molecular aggregates.

The parameter range examined in this work would lead to a short wavelength infrared laser, the low dispersion of which would make it a strong candidate for the benefit of efficiently distributing converted solar energy [177]. Additionally the proposed biomimetic molecular aggregates from this work might lend themselves towards sunlight-pumped nanolasers [181], as they should be able to lase in cavities of volume $(\lambda/20)^3$ [182].

While Bloch-Redfield dissipators can avoid issues that Lindblad dissipators encounter when modelling systems with near degenerate terms, the choice of large J values throughout this project meant that the additional computational work in forming Bloch-Redfield dissipators was arguable unnecessary, as the two approaches produced results agreeing to machine precision when both analysing the full Hilbert space. Most of the differences between the models examined here arose from the reduction to a two level system.

It should be noted that, as was seen in Chapters 2 and 3, the inclusion of strong coupling to vibrational modes can affect collective optical behaviour, reducing the relative darkness and brightness effects. The proposal of using additional molecules as antennae does counteract this somewhat, but while the models showed strong agreement at the dimer scale, one should be wary of other effects coming into play for larger systems like non-radiative decay pathways as well as exciton-exciton annihilation [151, 152].

Chapter 6

Conclusions and Outlook

This thesis has examined a variety of systems which can take advantage of collective optical effects in the presence of a vibrational environment due to their design. The underlying modelling in all systems considered relied upon open quantum systems techniques.

The first research chapter proposed a series of conditions for a guide-slide superabsorber. By examining our proposed candidate system, we showed that the sacrifice in optical coupling produced a system which was able to display a super-linear growth in net power production with system size, while also benefiting from vibrational effects which guide the system towards the enhanced behaviour. We found our candidate system could continue operating in the presence of disorder, as well as with a strongly-coupled vibrational environment in the polaron frame, amongst several other model extensions. While this work validates a range of potential condensed matter systems for designing a superabsorber, the comparative ease with which superconducting qubits can be designed to desirable specifications might mean an experimental realisation of parallel-superabsorption could occur before one of guide-slide superabsorption, unless the effect of phonons were modelled into the platform. Additionally, one could implement the trap modelling extensions being implemented in Chapter 3 to extend this work, or develop a multi-site variational model to look at vibrational coupling strengths between weak and strong coupling regimes.

The second research chapter considered optical ratcheting, a process whereby rapid vibrational relaxation after an absorption event allows an artificial light harvester to store one photon while still being able to absorb another. We applied a polaron transformation to confirm that ratcheting could still occur with strong vibrational coupling, which can be the undoing of collective optical effects. We then updated our trap modelling approach to treat it as an additional dipole in the system, considering the setups needed to achieve the optimal extraction. Some aspects of this work are ongoing, with the obvious open question being to combine these two features, but so far we have been held up by the range of questions each addition

has thrown up individually, delaying our plans to combine them.

Having looked at idealised collective optical effects in bio-inspired designs for artificial light harvesters, the third research chapter looked at whether an actual photosynthetic complex, iron stress-induced protein A (IsiA), might be able to rely on rapid vibrational relaxation and collective darkness to improve its performance beyond classical limitations. This collaborative work suggested the structure was optimised to suppress optical relaxation to a degree, but that experimental studies carried out at cryogenic temperatures would see this effect magnified. We were able to disturb the structure and establish which components were more impervious to shifts without noticeably changing the behaviour, providing insight into the function of the complex. Building off of this work, one could take our approach and use it to model other biological systems. Additionally the inclusion of other components like pigments and reactions centres could be included to develop a picture of transport in such systems as well.

Finally, the fourth research chapter also investigated the use of larger photosynthetic complexes for use as a gain medium in a laser proposal. Due to the complexities in modelling such large systems discussed in Chapter 4, our collaborators developed an equation for predicting the performance of lasers using such aggregates. My contributions looked at a smaller, more tractable system, which could be more fully analysed, and thereby provide validity for their approach. Considering a H-dimer, we showed that with adequate control of the geometry, the combination of collective optical coupling and rapid vibrational relaxation made population inversion possible. We then used a semi-classical approach to model a field in a resonant cavity coupled to a disordered ensemble of such dimers, showing that a steady field was achievable. It might be possible to perform such modelling with slightly larger systems, for example a quadmer, before needing to swap to the alternative model, allowing agreement with different system sizes to be established. Additionally, while Chapters 2 and 3 showed that collective optical effects can occur in a strong coupling regime, they also showed that they are a negative effect. It would be interesting how drastically the behaviour of this proposal would change with the inclusion of such a coupling.

Bibliography

[1] R. H. Dicke. Coherence in Spontaneous Radiation Processes. *Phys. Rev.*, 93(1):99–110, jan 1954.

[2] N. Skribanowitz, I. P. Herman, J. C. MacGillivray, and M. S. Feld. Observation of dicke superradiance in optically pumped hf gas. *Phys. Rev. Lett.*, 30:309–312, Feb 1973.

[3] R. G. DeVoe and R. G. Brewer. Observation of superradiant and subradiant spontaneous emission of two trapped ions. *Phys. Rev. Lett.*, 76:2049–2052, Mar 1996.

[4] Justin G Bohnet, Zilong Chen, Joshua M Weiner, Dominic Meiser, Murray J Holland, and James K Thompson. A steady-state superradiant laser with less than one intracavity photon. *Nature*, 484(7392):78–81, 2012.

[5] Marlan O. Scully, Edward S. Fry, C. H. Raymond Ooi, and Krzysztof Wódkiewicz. Directed spontaneous emission from an extended ensemble of n atoms: Timing is everything. *Phys. Rev. Lett.*, 96:010501, Jan 2006.

[6] Marlan O. Scully. Single photon subradiance: Quantum control of spontaneous emission and ultrafast readout. *Phys. Rev. Lett.*, 115:243602, Dec 2015.

[7] Philip A Vetter, Luojia Wang, Da-Wei Wang, and Marlan O Scully. Single photon subradiance and superradiance revisited: a group theoretic analysis of subradiant states. *Physica Scripta*, 91(2):023007, jan 2016.

[8] S. A. Gurvitz. Measurements with a noninvasive detector and dephasing mechanism. *Phys. Rev. B*, 56:15215–15223, Dec 1997.

[9] J. R. Petta, A. C. Johnson, C. M. Marcus, M. P. Hanson, and A. C. Gossard. Manipulation of a single charge in a double quantum dot. *Phys. Rev. Lett.*, 93:186802, Oct 2004.

[10] K. D. B. Higgins, S. C. Benjamin, T. M. Stace, G. J. Milburn, B. W. Lovett, and E. M. Gauger. Superabsorption of light via quantum engineering. *Nat. Commun.*, 5:4705, aug 2014.

[11] Alexey Kalachev. Quantum storage on subradiant states in an extended atomic ensemble. *Phys. Rev. A*, 76:043812, Oct 2007.

[12] Robert Alicki and Mark Fannes. Entanglement boost for extractable work from ensembles of quantum batteries. *Phys. Rev. E*, 87:042123, Apr 2013.

[13] Felix C Binder, Sai Vinjanampathy, Kavan Modi, and John Goold. Quantacell: powerful charging of quantum batteries. *New Journal of Physics*, 17(7):075015, jul 2015.

[14] Dario Ferraro, Michele Campisi, Gian Marcello Andolina, Vittorio Pellegrini, and Marco Polini. High-power collective charging of a solid-state quantum battery. *Phys. Rev. Lett.*, 120:117702, Mar 2018.

[15] William Shockley and Hans J Queisser. Detailed Balance Limit of Efficiency of pn Junction Solar Cells Theoretical efficiency limit for a two-terminal multi-junction " step-cell " using detailed balance method Detailed Balance Limit of Efficiency of p-n Junction Solar Cells*. *J. Appl. Phys.*, 32(98), 1961.

[16] Marlan O. Scully. Quantum photocell: Using quantum coherence to reduce radiative recombination and increase efficiency. *Phys. Rev. Lett.*, 104:207701, May 2010.

[17] C. Creatore, M. A. Parker, S. Emmott, and A. W. Chin. Efficient Biologically Inspired Photocell Enhanced by Delocalized Quantum States. *Phys. Rev. Lett.*, 111(25):253601, dec 2013.

[18] Amir Fruchtman, Rafael Gómez-Bombarelli, Brendon W. Lovett, and Erik M. Gauger. Photocell Optimization Using Dark State Protection. *Phys. Rev. Lett.*, 117(20):203603, nov 2016.

[19] K. D. B. Higgins, B. W. Lovett, and E. M. Gauger. Quantum-Enhanced Capture of Photons Using Optical Ratchet States. *J. Phys. Chem. C*, 121(38):20714–20719, sep 2017.

[20] Rocío Sáez-Blázquez, Johannes Feist, Elisabet Romero, Antonio I. Fernández-Domínguez, and Francisco J. García-Vidal. Cavity-modified exciton dynamics in photosynthetic units. *The Journal of Physical Chemistry Letters*, 10(15):4252–4258, 08 2019.

[21] Stefano Tomasi, Sima Baghbanzadeh, Saleh Rahimi-Keshari, and Ivan Kassal. Coherent and controllable enhancement of light-harvesting efficiency. *Phys. Rev. A*, 100:043411, Oct 2019.

[22] Sangchul Oh, Jungjun Park, and Hyunchul Nha. Quantum photovoltaic cells driven by photon pulses, 2020.

[23] W. M. Brown and E. M. Gauger. Light harvesting with guide-slide superabsorbing condensed-matter nanostructures. *The Journal of Physical Chemistry Letters*, 10(15):4323–4329, 2019. PMID: 31251067.

[24] Paul Benioff. The computer as a physical system: A microscopic quantum mechanical hamiltonian model of computers as represented by turing machines. *Journal of Statistical Physics*, 22(5):563–591, 1980.

[25] Robert E. Blankenship. *Molecular mechanisms of photosynthesis*. John Wiley & Sons, 2 edition, 2014.

[26] Gregory D. Scholes, Graham R. Fleming, Alexandra Olaya-Castro, and Rienk van Grondelle. Lessons from nature about solar light harvesting. *Nat. Chem.*, 3(10):763, 10 2011.

[27] Elisabet Romero, Vladimir I. Novoderezhkin, and Rienk van Grondelle. Quantum design of photosynthesis for bio-inspired solar-energy conversion. *Nature*, 543:355 EP –, 03 2017.

[28] Gregory D. Scholes, Graham R. Fleming, Lin X. Chen, Alán Aspuru-Guzik, Andreas Buchleitner, David F. Coker, Gregory S. Engel, Rienk van Grondelle, Akihito Ishizaki, David M. Jonas, Jeff S. Lundeen, James K. McCusker, Shaul Mukamel, Jennifer P. Ogilvie, Alexandra Olaya-Castro, Mark A. Ratner, Frank C. Spano, K. Birgitta Whaley, and Xiaoyang Zhu. Using coherence to enhance function in chemical and biophysical systems. *Nature*, 543:647 EP –, 03 2017.

[29] Koichiro Mukai, Shuji Abe, and Hitoshi Sumi. Theory of rapid excitation-energy transfer from b800 to optically-forbidden exciton states of b850 in the antenna system lh2 of photosynthetic purple bacteria. *The Journal of Physical Chemistry B*, 103(29):6096–6102, 1999.

[30] Richard John Cogdell, Alastair Thomas Gardiner, Hideki Hashimoto, and Tatas Hardo Panintingjati Brotosudarmo. A comparative look at the first few milliseconds of the light reactions of photosynthesis. *Photochemical & Photobiological Sciences*, 7(10):1150, 2008.

[31] Gregory D Scholes. Quantum-Coherent Electronic Energy Transfer: Did Nature Think of It First? *J. Phys. Chem. Lett*, 1:2–8, 2010.

[32] Pengfei Huo and David F Coker. Theoretical Study of Coherent Excitation Energy Transfer in Cryptophyte Phycocyanin 645 at Physiological Temperature. *J. Phys. Chem. Lett*, 2:825–833, 2011.

[33] R. E. Fenna and B. W. Matthews. Chlorophyll arrangement in a bacteriochlorophyll protein from Chlorobium limicola. *Nature*, 258(5536):573–577, dec 1975.

[34] Neill Lambert, Yueh-Nan Chen, Yuan-Chung Cheng, Che-Ming Li, Guang-Yin Chen, and Franco Nori. Quantum biology. *Nature Physics*, 9(1):10–18, 2013.

[35] Gregory S Engel, Tessa R Calhoun, Elizabeth L Read, Tae-Kyu Ahn, Tomáš Mančal, Yuan-Chung Cheng, Robert E Blankenship, and Graham R Fleming. Evidence for wavelike energy transfer through quantum coherence in photosynthetic systems. *Nature*, 446(7137):782–786, 2007.

[36] Hohjai Lee, Yuan-Chung Cheng, and Graham R Fleming. Coherence dynamics in photosynthesis: protein protection of excitonic coherence. *Science (New York, N.Y.)*, 316(5830):1462–5, jun 2007.

[37] Gitt Panitchayangkoon, Dugan Hayes, Kelly A Fransted, Justin R Caram, Elad Harel, Jianzhong Wen, Robert E Blankenship, and Gregory S Engel. Long-lived quantum coherence in photosynthetic complexes at physiological temperature. *Proceedings of the National Academy of Sciences*, 107(29):12766–12770, 2010.

[38] Alex C. Han, Moshe Shapiro, and Paul Brumer. Nature of quantum states created by one photon absorption: Pulsed coherent vs pulsed incoherent light. *The Journal of Physical Chemistry A*, 117(34):8199–8204, 2013. PMID: 23879891.

[39] Johan Strümpfer, Melih Sener, and Klaus Schulten. How quantum coherence assists photosynthetic light-harvesting. *The journal of physical chemistry letters*, 3(4):536–542, 2012.

[40] Melih K Şener, John D Olsen, C Neil Hunter, and Klaus Schulten. Atomic-level structural and functional model of a bacterial photosynthetic membrane vesicle. *Proceedings of the National Academy of Sciences*, 104(40):15723–15728, 2007.

[41] J Thomas Beatty, Jörg Overmann, Michael T Lince, Ann K Manske, Andrew S Lang, Robert E Blankenship, Cindy L Van Dover, Tracey A Martinson, and F Gerald Plumley. An obligately photosynthetic bacterial anaerobe from a deep-sea hydrothermal vent. *Proceedings of the National Academy of Sciences*, 102(26):9306–9310, 2005.

[42] Sima Baghbanzadeh and Ivan Kassal. Geometry, supertransfer, and optimality in the light harvesting of purple bacteria. *The journal of physical chemistry letters*, 7(19):3804–3811, 2016.

[43] Sima Baghbanzadeh and Ivan Kassal. Distinguishing the roles of energy funnelling and delocalization in photosynthetic light harvesting. *Physical Chemistry Chemical Physics*, 18(10):7459–7467, 2016.

[44] Thorsten Ritz, Salih Adem, and Klaus Schulten. A model for photoreceptor-based magnetoreception in birds. *Biophysical journal*, 78(2):707–718, 2000.

[45] Sönke Johnsen and Kenneth J. Lohmann. The physics and neurobiology of magnetoreception. *Nature Reviews Neuroscience*, 6(9):703–712, sep 2005.

[46] Nina Keary, Tim Ruploh, Joe Voss, Peter Thalau, Roswitha Wiltschko, Wolfgang Wiltschko, and Hans-Joachim Bischof. Oscillating magnetic field disrupts magnetic orientation in Zebra finches, Taeniopygia guttata. *Frontiers in Zoology*, 6(1):25, 2009.

[47] Christopher T Rodgers and Peter J Hore. Chemical magnetoreception in birds: the radical pair mechanism. *Proceedings of the National Academy of Sciences*, 106(2):353–360, 2009.

[48] Thorsten Ritz, Peter Thalau, John B. Phillips, Roswitha Wiltschko, and Wolfgang Wiltschko. Resonance effects indicate a radical-pair mechanism for avian magnetic compass. *Nature*, 429(6988):177–180, may 2004.

[49] Thorsten Ritz, Roswitha Wiltschko, P J Hore, Christopher T Rodgers, Katrin Stapput, Peter Thalau, Christiane R Timmel, and Wolfgang Wiltschko. Magnetic compass of birds is based on a molecule with optimal directional sensitivity. *Biophysical journal*, 96(8):3451–7, apr 2009.

[50] Erik M Gauger, Elisabeth Rieper, John JL Morton, Simon C Benjamin, and Vlatko Vedral. Sustained quantum coherence and entanglement in the avian compass. *Physical review letters*, 106(4):040503, 2011.

[51] Hamish G Hiscock, Susannah Worster, Daniel R Kattnig, Charlotte Steers, Ye Jin, David E Manolopoulos, Henrik Mouritsen, and PJ Hore. The quantum needle of the avian magnetic compass. *Proceedings of the National Academy of Sciences*, 113(17):4634–4639, 2016.

[52] M. I. Franco, L. Turin, A. Mershin, and E. M. C. Skoulakis. Molecular vibration-sensing component in Drosophila melanogaster olfaction. *Proceedings of the National Academy of Sciences*, 108(9):3797–3802, mar 2011.

[53] Thomas P Hettinger. Olfaction is a chemical sense, not a spectral sense. *Proceedings of the National Academy of Sciences of the United States of America*, 108(31):E349; author reply E350, aug 2011.

[54] Ross D. Hoehn, David E. Nichols, Hartmut Neven, and Sabre Kais. Status of the vibrational theory of olfaction. *Frontiers in Physics*, 6:25, 2018.

[55] Daeho Yang, Seung-hoon Oh, Junseok Han, Gibeom Son, Junki Kim, Jinuk Kim, and Kyungwon An. Observation of superabsorption by correlated atoms. *arXiv preprint arXiv:1906.06477*, jun 2019.

[56] Ahsan Nazir and Dara P S McCutcheon. Modelling exciton–phonon interactions in optically driven quantum dots. *J. Phys. Condens. Matter*, 28(10):103002, feb 2016.

[57] Hila Toporik, Jin Li, Dewight Williams, Po-Lin Chiu, and Yuval Mazor. The structure of the stress-induced photosystem I–IsiA antenna supercomplex. *Nature Structural & Molecular Biology*, 26(6):443–449, jun 2019.

[58] Hanan Schoffman and Nir Keren. Function of the IsiA pigment–protein complex in vivo. *Photosynthesis Research*, 141(3):343–353, sep 2019.

[59] F. Mattiotti, W. M. Brown, N. Piovella, S. Olivares, E. M. Gauger, and G. L. Celardo. Bio-inspired sunlight-pumped lasers. Under review, 2020.

[60] Igor Pochorovski, Tim Knehans, Daniel Nettels, Astrid M. Müller, W. Bernd Schweizer, Amedeo Caflisch, Benjamin Schuler, and François Diederich. Experimental and Computational Study of BODIPY Dye-Labeled Cavitand Dynamics. *J. Am. Chem. Soc.*, 136(6):2441–2449, feb 2014.

[61] Junhua Yu, Xuesong Wang, Baowen Zhang, Yuxiang Weng, and Lei Zhang. Prolonged Excited-State Lifetime of Porphyrin Due to the Addition of Colloidal SiO2 to Triton X-100 Micelles. *Langmuir*, 2004.

[62] Frank Würthner. Dipole–Dipole Interaction Driven Self-Assembly of Merocyanine Dyes: From Dimers to Nanoscale Objects and Supramolecular Materials. *Acc. Chem. Res.*, 49(5):868–876, may 2016.

[63] Elisa A. Hemmig, Celestino Creatore, Bettina Wünsch, Lisa Hecker, Philip Mair, M. Andy Parker, Stephen Emmott, Philip Tinnefeld, Ulrich F. Keyser, and Alex W. Chin. Programming Light-Harvesting Efficiency Using DNA Origami. *Nano Lett.*, 16(4):2369–2374, apr 2016.

[64] Melanie C. O'Sullivan, Johannes K. Sprafke, Dmitry V. Kondratuk, Corentin Rinfray, Timothy D. W. Claridge, Alex Saywell, Matthew O. Blunt, James N.

O'Shea, Peter H. Beton, Marc Malfois, and Harry L. Anderson. Vernier templating and synthesis of a 12-porphyrin nano-ring. *Nature*, 469(7328):72–75, jan 2011.

[65] Johannes K. Sprafke, Dmitry V. Kondratuk, Michael Wykes, Amber L. Thompson, Markus Hoffmann, Rokas Drevinskas, Wei-Hsin Chen, Chaw Keong Yong, Joakim Kärnbratt, Joseph E. Bullock, Marc Malfois, Michael R. Wasielewski, Bo Albinsson, Laura M. Herz, Donatas Zigmantas, David Beljonne, and Harry L. Anderson. Belt-Shaped π-Systems: Relating Geometry to Electronic Structure in a Six-Porphyrin Nanoring. *J. Am. Chem. Soc.*, 133(43):17262–17273, nov 2011.

[66] H.-P. Breuer and F. Petruccione. *The Theory of Open Quantum Systems*. Oxford University Press, 2002.

[67] M. Gross and S. Haroche. Superradiance: An essay on the theory of collective spontaneous emission. *Phys. Rep.*, 93(5):301–396, 1982.

[68] Gerald D. Mahan. *Many Particle Physics (Physics of Solids and Liquids)*. Springer, 3rd edition, 2000.

[69] Marlan O Scully, Kimberly R Chapin, Konstantin E Dorfman, Moochan Barnabas Kim, and Anatoly Svidzinsky. Quantum heat engine power can be increased by noise-induced coherence. *Proc. Natl. Acad. Sci. U.S.A.*, 108(37):15097–100, sep 2011.

[70] Yasuhiro Yamada, Youhei Yamaji, and Masatoshi Imada. Exciton Lifetime Paradoxically Enhanced by Dissipation and Decoherence: Toward Efficient Energy Conversion of a Solar Cell. *Phys. Rev. Lett.*, 115(19):197701, nov 2015.

[71] Yiteng Zhang, Sangchul Oh, Fahhad H. Alharbi, Gregory S. Engel, and Sabre Kais. Delocalized quantum states enhance photocell efficiency. *Phys. Chem. Chem. Phys.*, 17(8):5743–5750, 2015.

[72] Melina Wertnik, Alex Chin, Franco Nori, and Neill Lambert. Optimizing co-operative multi-environment dynamics in a dark-state-enhanced photosynthetic heat engine. *J. Chem. Phys.*, 149(8):084112, aug 2018.

[73] Yiteng Zhang, Aaron Wirthwein, Fahhad H. Alharbi, Gregory S. Engel, and Sabre Kais. Dark states enhance the photocell power via phononic dissipation. *Phys. Chem. Chem. Phys.*, 18:31845–31849, 2016.

[74] Christopher J. Law, Aleksander W. Roszak, June Southall, Alastair T. Gardiner, Neil W. Isaacs, and Richard J. Cogdell. The structure and function of

bacterial light-harvesting complexes (Review). *Mol. Membr. Biol.*, 21(3):183–191, jan 2004.

[75] Hitoshi Sumi. Bacterial photosynthesis begins with quantum-mechanical coherence. *The Chemical Record*, 1(6):480–93, 2001.

[76] Xiche Hu, Thorsten Ritz, Ana Damjanović, and Klaus Schulten. Pigment Organization and Transfer of Electronic Excitation in the Photosynthetic Unit of Purple Bacteria. *J. Phys. Chem. B*, 101(19):3854–3871, 1997.

[77] Shunichi Takahashi and Murray R. Badger. Photoprotection in plants: a new light on photosystem II damage. *Trends Plant Sci.*, 16(1):53–60, jan 2011.

[78] G. V. Varada and G. S. Agarwal. Two-photon resonance induced by the dipole-dipole interaction. *Phys. Rev. A*, 45(9):6721–6729, may 1992.

[79] Carles Curutchet and Benedetta Mennucci. Quantum Chemical Studies of Light Harvesting. *Chem. Rev.*, 117(2):294–343, jan 2017.

[80] G. S. Agarwal. Quantum statistical theories of spontaneous emission and their relation to other approaches. pages 1–128. Springer, Berlin, Heidelberg, 1974.

[81] Vyacheslav N Shatokhin, Mattia Walschaers, Frank Schlawin, and Andreas Buchleitner. Coherence turned on by incoherent light. *New J. Phys.*, 20(11):113040, nov 2018.

[82] Erik M. Gauger and Joachim Wabnig. Heat pumping with optically driven excitons. *Phys. Rev. B*, 82:073301, Aug 2010.

[83] A. J. Ramsay, T. M. Godden, S. J. Boyle, E. M. Gauger, A. Nazir, B. W. Lovett, Achanta Venu Gopal, A. M. Fox, and M. S. Skolnick. Effect of detuning on the phonon induced dephasing of optically driven ingaas/gaas quantum dots. *J. Appl. Phys.*, 109(10):102415, 2011.

[84] Andreas Angerer, Kirill Streltsov, Thomas Astner, Stefan Putz, Hitoshi Sumiya, Shinobu Onoda, Junichi Isoya, William J. Munro, Kae Nemoto, Jörg Schmiedmayer, and Johannes Majer. Superradiant emission from colour centres in diamond. *Nat. Phys.*, 14(12):1168–1172, dec 2018.

[85] Konstantin E Dorfman, Dmitri V Voronine, Shaul Mukamel, and Marlan O Scully. Photosynthetic reaction center as a quantum heat engine. *Proc. Natl. Acad. Sci. U.S.A.*, 110(8):2746–51, feb 2013.

[86] Giulio G. Giusteri, Francesco Mattiotti, and G. Luca Celardo. Non-Hermitian Hamiltonian approach to quantum transport in disordered networks with sinks: Validity and effectiveness. *Phys. Rev. B*, 91:094301, Mar 2015.

[87] Gernot Schaller, Giulio Giuseppe Giusteri, and Giuseppe Luca Celardo. Collective couplings: Rectification and supertransmittance. *Phys. Rev. E*, 94:032135, Sep 2016.

[88] Peter Würfel and Uli Würfel. *Physics of Solar Cells: From Basic Principles to Advanced Concepts*. Wiley-VCH, 3 edition, 9 2016.

[89] Yonatan Dubi. Interplay between Dephasing and Geometry and Directed Heat Flow in Exciton Transfer Complexes. *J. Phys. Chem. C*, 119(45):25252–25259, nov 2015.

[90] Sima Baghbanzadeh and Ivan Kassal. Geometry, Supertransfer, and Optimality in the Light Harvesting of Purple Bacteria. *J. Phys. Chem. Lett.*, 7(19):3804–3811, oct 2016.

[91] Yang Zhang, G. Luca Celardo, Fausto Borgonovi, and Lev Kaplan. Opening-assisted coherent transport in the semiclassical regime. *Phys. Rev. E*, 95(2):022122, feb 2017.

[92] Megan Creasey, Ji-Hoon Lee, Zhiming Wang, Gregory J. Salamo, and Xiaoqin Li. Self-Assembled InGaAs Quantum Dot Clusters with Controlled Spatial and Spectral Properties. *Nano Lett.*, 12(10):5169–5174, oct 2012.

[93] Brian D. Gerardot, Stefan Strauf, Michiel J. A. de Dood, Andrey M. Bychkov, Antonio Badolato, Kevin Hennessy, Evelyn L. Hu, Dirk Bouwmeester, and Pierre M. Petroff. Photon Statistics from Coupled Quantum Dots. *Phys. Rev. Lett.*, 95(13):137403, sep 2005.

[94] B. Lounis, H.A. Bechtel, D. Gerion, P. Alivisatos, and W.E. Moerner. Photon antibunching in single CdSe/ZnS quantum dot fluorescence. *Chem. Phys. Lett.*, 329(5-6):399–404, oct 2000.

[95] S B Brichkin and V F Razumov. Colloidal quantum dots: synthesis, properties and applications. *Russ. Chem. Rev.*, 85(12):1297–1312, dec 2016.

[96] A Albrecht, G Koplovitz, A Retzker, F Jelezko, S Yochelis, D Porath, Y Nevo, O Shoseyov, Y Paltiel, and M B Plenio. Self-assembling hybrid diamond–biological quantum devices. *New J. Phys.*, 16(9):093002, sep 2014.

[97] P. Neumann, R. Kolesov, B. Naydenov, J. Beck, F. Rempp, M. Steiner, V. Jacques, G. Balasubramanian, M. L. Markham, D. J. Twitchen, S. Pezzagna, J. Meijer, J. Twamley, F. Jelezko, and J. Wrachtrup. Quantum register based on coupled electron spins in a room-temperature solid. *Nat. Phys.*, 6(4):249–253, apr 2010.

[98] L.J. Rogers, K.D. Jahnke, T. Teraji, L. Marseglia, C. Müller, B. Naydenov, H. Schauffert, C. Kranz, J. Isoya, L.P. McGuinness, and F. Jelezko. Multiple intrinsically identical single-photon emitters in the solid state. *Nat. Commun.*, 5:4739, aug 2014.

[99] A Sipahigil, R E Evans, D D Sukachev, M J Burek, J Borregaard, M K Bhaskar, C T Nguyen, J L Pacheco, H A Atikian, C Meuwly, R M Camacho, F Jelezko, E Bielejec, H Park, M Lončar, and M D Lukin. An integrated diamond nanophotonics platform for quantum-optical networks. *Science*, 354(6314):847–850, nov 2016.

[100] Kevin J. Morse, Rohan J. S. Abraham, Adam DeAbreu, Camille Bowness, Timothy S. Richards, Helge Riemann, Nikolay V. Abrosimov, Peter Becker, Hans-Joachim Pohl, Michael L. W. Thewalt, and Stephanie Simmons. A photonic platform for donor spin qubits in silicon. *Sci. Adv.*, 3(7):e1700930, jul 2017.

[101] J. L. O'Brien, S. R. Schofield, M. Y. Simmons, R. G. Clark, A. S. Dzurak, N. J. Curson, B. E. Kane, N. S. McAlpine, M. E. Hawley, and G. W. Brown. Towards the fabrication of phosphorus qubits for a silicon quantum computer. *Phys. Rev. B*, 64(16):161401, sep 2001.

[102] Martin Fuechsle, Jill A. Miwa, Suddhasatta Mahapatra, Hoon Ryu, Sunhee Lee, Oliver Warschkow, Lloyd C. L. Hollenberg, Gerhard Klimeck, and Michelle Y. Simmons. A single-atom transistor. *Nat. Nanotechnol.*, 7(4):242–246, apr 2012.

[103] S. R. Schofield, N. J. Curson, M. Y. Simmons, F. J. Rueß, T. Hallam, L. Oberbeck, and R. G. Clark. Atomically Precise Placement of Single Dopants in Si. *Phys. Rev. Lett.*, 91(13):136104, sep 2003.

[104] Mikhail Y Berezin and Samuel Achilefu. Fluorescence lifetime measurements and biological imaging. *Chem. Rev.*, 110(5):2641–84, may 2010.

[105] Sabriye Acikgoz, Gulen Aktas, M. Naci Inci, Huseyin Altin, and Amitav Sanyal. FRET between BODIPY Azide Dye Clusters within PEG-Based Hydrogel: A Handle to Measure Stimuli Responsiveness. *J. Phys. Chem. B*, 114(34):10954–10960, sep 2010.

[106] Pei-Hua Chung, Carolyn Tregidgo, and Klaus Suhling. Determining a fluorophore's transition dipole moment from fluorescence lifetime measurements in solvents of varying refractive index. *Methods Appl. Fluoresc.*, 4(4):045001, nov 2016.

[107] Ulrich Rösch, Sheng Yao, Rüdiger Wortmann, and Frank Würthner. Fluorescent H-Aggregates of Merocyanine Dyes. *Angew. Chem.*, 45(42):7026–7030, oct 2006.

[108] Yuki Obara, Keita Saitoh, Masaru Oda, and Toshiro Tani. Room-temperature fluorescence lifetime of pseudoisocyanine (PIC) J excitons with various aggregate morphologies in relation to microcavity polariton formation. *Int. J. Mol. Sci.*, 13(5):5851–65, 2012.

[109] H. von Berlepsch, C. Böttcher, and L. Dähne. Structure of J-Aggregates of Pseudoisocyanine Dye in Aqueous Solution. *J. Phys. Chem. B*, 104(37):8792–8799, sep 2000.

[110] J. A. Mlynek, A. A. Abdumalikov, C. Eichler, and A. Wallraff. Observation of Dicke superradiance for two artificial atoms in a cavity with high decay rate. *Nat. Commun.*, 5:5186, 11 2014.

[111] Anton Potočnik, Arno Bargerbos, Florian A. Y. N. Schröder, Saeed A. Khan, Michele C. Collodo, Simone Gasparinetti, Yves Salathé, Celestino Creatore, Christopher Eichler, Hakan E. Türeci, Alex W. Chin, and Andreas Wallraff. Studying light-harvesting models with superconducting circuits. *Nat. Commun.*, 9(1):904, dec 2018.

[112] Jakub K. Sowa, Jan A. Mol, G. Andrew D. Briggs, and Erik M. Gauger. Environment-assisted quantum transport through single-molecule junctions. *Phys. Chem. Chem. Phys.*, 19:29534–29539, 2017.

[113] W E Moerner. Single-photon sources based on single molecules in solids. *New J. Phys.*, 6(1):88–88, jul 2004.

[114] J Hwang and E A Hinds. Dye molecules as single-photon sources and large optical nonlinearities on a chip. *New J. Phys.*, 13(8):085009, aug 2011.

[115] Debabrata Mandal, Samir Kumar Pal, Dipankar Sukul, and Kankan Bhattacharyya. Photophysical Processes of Merocyanine 540 in Solutions and in Organized Media. *J. Phys. Chem. A*, 1999.

[116] J. Kim, V. P. Drachev, Z. Jacob, G. V. Naik, A. Boltasseva, E. E. Narimanov, and V. M. Shalaev. Improving the radiative decay rate for dye molecules with hyperbolic metamaterials. *Opt. Express*, 20(7):8100, mar 2012.

[117] D M Rouse, E M Gauger, and B W Lovett. Optimal power generation using dark states in dimers strongly coupled to their environment. *New J. Phys.*, 21(6):063025, jun 2019.

[118] Zixuan Hu, Gregory S. Engel, and Sabre Kais. Double-excitation manifold's effect on exciton transfer dynamics and the efficiency of coherent light harvesting. *Phys. Chem. Chem. Phys.*, 20:30032–30040, 2018.

[119] Dara P. S. McCutcheon, Nikesh S. Dattani, Erik M. Gauger, Brendon W. Lovett, and Ahsan Nazir. A general approach to quantum dynamics using a variational master equation: Application to phonon-damped rabi rotations in quantum dots. *Phys. Rev. B*, 84:081305, Aug 2011.

[120] Felix A Pollock, Dara P S McCutcheon, Brendon W Lovett, Erik M Gauger, and Ahsan Nazir. A multi-site variational master equation approach to dissipative energy transfer. *New J. Phys.*, 15(7):075018, jul 2013.

[121] Vytautas Butkus, Jan Alster, Eglė Bašinskaitė, Ramunas Augulis, Patrik Neuhaus, Leonas Valkunas, Harry L. Anderson, Darius Abramavicius, and Donatas Zigmantas. Discrimination of diverse coherences allows identification of electronic transitions of a molecular nanoring. *J. Phys. Chem. Lett.*, 8(10):2344–2349, 05 2017.

[122] B. Prasanna Venkatesh, M. L. Juan, and O. Romero-Isart. Cooperative effects in closely packed quantum emitters with collective dephasing. *Phys. Rev. Lett.*, 120:033602, Jan 2018.

[123] Marco Gullì, Alessia Valzelli, Francesco Mattiotti, Mattia Angeli, Fausto Borgonovi, and Giuseppe Luca Celardo. Macroscopic coherence as an emergent property in molecular nanotubes. *New J. Phys.*, 21(1):013019, jan 2019.

[124] A. Löhner, T. Kunsel, M. I. S. Röhr, T. L. C. Jansen, S. Sengupta, F. Würthner, J. Knoester, and J. Köhler. Spectral and Structural Variations of Biomimetic Light-Harvesting Nanotubes. *J. Phys. Chem. Lett.*, pages 2715–2724, may 2019.

[125] Domenico Caruso and Alessandro Troisi. Long-range exciton dissociation in organic solar cells. *Proceedings of the National Academy of Sciences*, 109(34):13498–13502, 2012.

[126] Wayne M. Itano, D. J. Heinzen, J. J. Bollinger, and D. J. Wineland. Quantum zeno effect. *Phys. Rev. A*, 41:2295–2300, Mar 1990.

[127] Hanan Schoffman, William M. Brown, Yossi Paltiel, Nir Keren, and Erik M. Gauger. Structure-based hamiltonian model for isia uncovers a highly robust pigment protein complex, 2020.

[128] D. E. Laudenbach and N. A. Straus. Characterization of a cyanobacterial iron stress-induced gene similar to psbC. *Journal of bacteriology*, 170(11):5018–5026, nov 1988.

[129] R. L. Burnap, T. Troyan, and L. A. Sherman. The Highly Abundant Chlorophyll-Protein Complex of Iron-Deficient Synechococcus sp. PCC7942 (CP43[prime]) Is Encoded by the isiA Gene. *Plant Physiology*, 103(3):893–902, nov 1993.

[130] Rudi Berera, Ivo H.M. van Stokkum, Sandrine D'Haene, John T.M. Kennis, Rienk van Grondelle, and Jan P. Dekker. A Mechanism of Energy Dissipation in Cyanobacteria. *Biophysical Journal*, 96(6):2261–2267, mar 2009.

[131] Thomas S. Bibby, Jon Nield, and James Barber. Iron deficiency induces the formation of an antenna ring around trimeric photosystem I in cyanobacteria. *Nature*, 412(6848):743–745, aug 2001.

[132] H.-Y.S. Chen, A. Bandyopadhyay, and H. B. Pakrasi. Function, regulation and distribution of IsiA, a membrane-bound chlorophyll a-antenna protein in cyanobacteria. *Photosynthetica*, 56(1):322–333, mar 2018.

[133] Hui-Yuan S. Chen, Michelle Liberton, Himadri B. Pakrasi, and Dariusz M. Niedzwiedzki. Reevaluating the mechanism of excitation energy regulation in iron-starved cyanobacteria. *Biochimica et Biophysica Acta (BBA) - Bioenergetics*, 1858(3):249–258, mar 2017.

[134] Michel Havaux, Geneviève Guedeney, Martin Hagemann, Nataliya Yeremenko, Hans C.P. Matthijs, and Robert Jeanjean. The chlorophyll-binding protein IsiA is inducible by high light and protects the cyanobacterium Synechocystis PCC6803 from photooxidative stress. *FEBS Letters*, 579(11):2289–2293, apr 2005.

[135] Janne A. Ihalainen, Sandrine D'Haene, Nataliya Yeremenko, Henny van Roon, Ana A. Arteni, Egbert J. Boekema, Rienk van Grondelle, Hans C. P. Matthijs, and Jan P. Dekker. Aggregates of the Chlorophyll-Binding Protein IsiA (CP43') Dissipate Energy in Cyanobacteria . *Biochemistry*, 44(32):10846–10853, aug 2005.

[136] Thomas J. Ryan-Keogh, Anna I. Macey, Amanda M. Cockshutt, C. Mark Moore, and Thomas S. Bibby. The cyanobacterial chlorophyll-binding-protein IsiA acts to increase the in vivo effective absorption cross-section of PSI under iron limitation. *Journal of Phycology*, 48(1):145–154, feb 2012.

[137] Abhay K. Singh and Louis A. Sherman. Reflections on the function of IsiA, a cyanobacterial stress-inducible, Chl-binding protein. *Photosynthesis Research*, 93(1-3):17–25, aug 2007.

[138] Junlei Sun and John H. Golbeck. The Presence of the IsiA-PSI Supercomplex Leads to Enhanced Photosystem I Electron Throughput in Iron-Starved

Cells of Synechococcus sp. PCC 7002. *The Journal of Physical Chemistry B*, 119(43):13549–13559, oct 2015.

[139] Nataliya Yeremenko, Roman Kouřil, Janne A. Ihalainen, Sandrine D'Haene, Niels van Oosterwijk, Elena G. Andrizhiyevskaya, Wilko Keegstra, Henk L. Dekker, Martin Hagemann, Egbert J. Boekema, Hans C. P. Matthijs, and Jan P. Dekker. Supramolecular Organization and Dual Function of the IsiA Chlorophyll-Binding Protein in Cyanobacteria . *Biochemistry*, 43(32):10308–10313, aug 2004.

[140] George C. Knee, Patrick Rowe, Luke D. Smith, Alessandro Troisi, and Animesh Datta. Structure-dynamics relation in physically-plausible multi-chromophore systems. *The Journal of Physical Chemistry Letters*, 8(10):2328–2333, 2017. PMID: 28475337.

[141] Hideki Hashimoto, Chiasa Uragami, and Richard J. Cogdell. *Carotenoids and Photosynthesis*, pages 111–139. Springer International Publishing, Cham, 2016.

[142] Delmar S. Larsen, Emmanouil Papagiannakis, Ivo H.M. [van Stokkum], Mikas Vengris, John T.M. Kennis, and Rienk [van Grondelle]. Excited state dynamics of β-carotene explored with dispersed multi-pulse transient absorption. *Chemical Physics Letters*, 381(5):733 – 742, 2003.

[143] Martin Linke, Alexandra Lauer, Theodore von Haimberger, Angelica Zacarias, and Karsten Heyne. Three-dimensional orientation of the qy electronic transition dipole moment within the chlorophyll a molecule determined by femtosecond polarization resolved vis pumpir probe spectroscopy. *Journal of the American Chemical Society*, 130(45):14904–14905, 2008. PMID: 18928259.

[144] Rienk van Grondelle, Jan P. Dekker, Tomas Gillbro, and Villy Sundström. Energy transfer and trapping in photosynthesis. *Biochimica et Biophysica Acta*, 1187:1–65, 1994.

[145] Akihito Ishizaki and Graham R. Fleming. Theoretical examination of quantum coherence in a photosynthetic system at physiological temperature. *Proceedings of the National Academy of Sciences*, 106(41):17255–17260, 2009.

[146] C. Creatore, M. A. Parker, S. Emmott, and A. W. Chin. Efficient biologically inspired photocell enhanced by delocalized quantum states. *Phys. Rev. Lett.*, 111:253601, Dec 2013.

[147] D. P. S. McCutcheon, A. Nazir, S. Bose, and A. J. Fisher. Long-lived spin entanglement induced by a spatially correlated thermal bath. *Phys. Rev. A*, 80:022337, Aug 2009.

[148] Erik M Gauger, Ahsan Nazir, Simon C Benjamin, Thomas M Stace, and Brendon W Lovett. Robust adiabatic approach to optical spin entangling in coupled quantum dots. *New Journal of Physics*, 10(7):073016, jul 2008.

[149] James Lim, Mark Tame, Ki Hyuk Yee, Joong-Sung Lee, and Jinhyoung Lee. Comment on 'energy transfer, entanglement and decoherence in a molecular dimer interacting with a phonon bath'. *New Journal of Physics*, 16(1):018001, jan 2014.

[150] Zixuan Hu, Gregory S. Engel, and Sabre Kais. Double-excitation manifold's effect on exciton transfer dynamics and the efficiency of coherent light harvesting. *Phys. Chem. Chem. Phys.*, 20:30032–30040, 2018.

[151] H. van Amerongen, L. Valkunas, and R. van Grondelle. *Photosynthetic excitons*. World Scientific Publishing Co. Pte. Ltd., 2000.

[152] Volkhard May. Kinetic theory of exciton–exciton annihilation. *The Journal of Chemical Physics*, 140(5):054103, 2014.

[153] Michael Kasha. Characterization of electronic transitions in complex molecules. *Discuss. Faraday Soc.*, 9:14–19, 1950.

[154] Chantal D. van der Weij-de Wit, Janne A. Ihalainen, Edith van de Vijver, Sandrine D'Haene, Hans C.P. Matthijs, Rienk van Grondelle, and Jan P. Dekker. Fluorescence quenching of IsiA in early stage of iron deficiency and at cryogenic temperatures. *Biochimica et Biophysica Acta (BBA) - Bioenergetics*, 1767(12):1393–1400, dec 2007.

[155] Natasha B. Taylor and Ivan Kassal. Generalised marcus theory for multimolecular delocalised charge transfer. *Chem. Sci.*, 9:2942–2951, 2018.

[156] Fei Ma, Elisabet Romero, Michael R. Jones, Vladimir I. Novoderezhkin, and Rienk van Grondelle. Both electronic and vibrational coherences are involved in primary electron transfer in bacterial reaction center. *Nature Communications*, 10(1):933, 2019.

[157] National Research Council. *Advancing Land Change Modeling: Opportunities and Research Requirements*. The National Academies Press, Washington, DC, 2014.

[158] T Yabe, T Ohkubo, S Uchida, K Yoshida, M Nakatsuka, T Funatsu, A Mabuti, A Oyama, K Nakagawa, T Oishi, et al. High-efficiency and economical solar-energy-pumped laser with fresnel lens and chromium codoped laser medium. *Applied physics letters*, 90(26):261120, 2007.

[159] Shigeaki Uchida, Takashi Yabe, Yuji Sato, Kunio Yoshida, Akio Ikesue, Tomomasa Ohkubo, Akito Mabuchi, Youichi Ogata, Kenji Nakagawa, Atsushi Ohyama, et al. Experimental study of solar pumped laser for magnesium-hydrogen energy cycle. In *AIP Conference Proceedings*, volume 830, pages 439–446. American Institute of Physics, 2006.

[160] Duncan Graham-Rowe. Solar-powered lasers. *Nature Photonics*, 4(2):64, 2010.

[161] Srikanth Madala and Robert F. Boehm. A review of nonimaging solar concentrators for stationary and passive tracking applications. *Renewable and Sustainable Energy Reviews*, 71:309 – 322, 2017.

[162] Philip D Reusswig, Sergey Nechayev, Jennifer M Scherer, Gyu Weon Hwang, Moungi G Bawendi, Marc A Baldo, and Carmel Rotschild. A path to practical solar pumped lasers via radiative energy transfer. *Scientific reports*, 5:14758, 2015.

[163] Xiche Hu, Ana Damjanović, Thorsten Ritz, and Klaus Schulten. Architecture and mechanism of the light-harvesting apparatus of purple bacteria. *Proceedings of the National Academy of Sciences*, 95(11):5935–5941, 1998.

[164] Xiche Hu, Ana Damjanović, Thorsten Ritz, and Klaus Schulten. Architecture and mechanism of the light-harvesting apparatus of purple bacteria. *Proceedings of the National Academy of Sciences*, 95(11):5935–5941, 1998.

[165] Jonathan Grad, Griselda Hernandez, and Shaul Mukamel. Radiative decay and energy transfer in molecular aggregates: the role of intermolecular dephasing. *Physical Review A*, 37(10):3835, 1988.

[166] Frank C Spano and Shaul Mukamel. Superradiance in molecular aggregates. *The Journal of Chemical Physics*, 91(2):683–700, 1989.

[167] Giuseppe L Celardo, Fausto Borgonovi, Marco Merkli, Vladimir I Tsifrinovich, and Gennady P Berman. Superradiance transition in photosynthetic light-harvesting complexes. *The Journal of Physical Chemistry C*, 116(42):22105–22111, 2012.

[168] Diego Ferrari, GL Celardo, Gennady P Berman, RT Sayre, and Fausto Borgonovi. Quantum biological switch based on superradiance transitions. *The Journal of Physical Chemistry C*, 118(1):20–26, 2014.

[169] Marco Gullì, Alessia Valzelli, Francesco Mattiotti, Mattia Angeli, Fausto Borgonovi, and Giuseppe Luca Celardo. Macroscopic coherence as an emergent property in molecular nanotubes. *New Journal of Physics*, 21(1):013019, 2019.

[170] Prathap Reddy Patlolla, Amarjyoti Das Mahapatra, Sairam S Mallajosyula, and Bhaskar Datta. Template-free h-dimer and h-aggregate formation by dimeric carbocyanine dyes. *New Journal of Chemistry*, 42(9):6727–6734, 2018.

[171] Monica Caselli, Loredana Latterini, and Glauco Ponterini. Consequences of h-dimerization on the photophysics and photochemistry of oxacarbocyanines. *Physical Chemistry Chemical Physics*, 6(14):3857–3863, 2004.

[172] VI Gavrilenko and MA Noginov. Ab initio study of optical properties of rhodamine 6g molecular dimers. *The Journal of chemical physics*, 124(4):044301, 2006.

[173] Nicholas J Hestand and Frank C Spano. Expanded theory of h-and j-molecular aggregates: the effects of vibronic coupling and intermolecular charge transfer. *Chemical reviews*, 118(15):7069–7163, 2018.

[174] Johannes Gierschner, Shinto Varghese, and Soo Young Park. Organic single crystal lasers: A materials view. *Advanced Optical Materials*, 4(3):348–364, 2016.

[175] Serdar Özçelik, Isin Özçelik, and Daniel L Akins. Superradiant lasing from j-aggregated molecules adsorbed onto colloidal silver. *Applied physics letters*, 73(14):1949–1951, 1998.

[176] James C Hindman, Roger Kugel, Michael R Wasielewski, and Joseph J Katz. Coherent stimulated light emission (lasing) in covalently linked chlorophyll dimers. *Proceedings of the National Academy of Sciences*, 75(5):2076–2079, 1978.

[177] Arundhati P. Deshmukh, Danielle Koppel, Chern Chuang, Danielle M. Cadena, Jianshu Cao, and Justin R. Caram. Design principles for two-dimensional molecular aggregates using kasha's model: Tunable photophysics in near and short-wave infrared. *The Journal of Physical Chemistry C*, 123(30):18702–18710, 2019.

[178] Marlan O. Scully and M. Suhail Zubairy. *Quantum Optics*. Cambridge University Press, 1997.

[179] Joonsuk Huh, Semion K Saikin, Jennifer C Brookes, Stephanie Valleau, Takatoshi Fujita, and Alan Aspuru-Guzik. Atomistic study of energy funneling in the light-harvesting complex of green sulfur bacteria. *Journal of the American Chemical Society*, 136(5):2048–2057, 2014.

[180] Kapil Amarnath, Doran IG Bennett, Anna R Schneider, and Graham R Fleming. Multiscale model of light harvesting by photosystem ii in plants. *Proceedings of the National Academy of Sciences*, 113(5):1156–1161, 2016.

[181] Ren-Min Ma and Rupert F Oulton. Applications of nanolasers. *Nature nanotechnology*, 14(1):12–22, 2019.

[182] Jie Yao, Xiaodong Yang, Xiaobo Yin, Guy Bartal, and Xiang Zhang. Three-dimensional nanometer-scale optical cavities of indefinite medium. *Proceedings of the National Academy of Sciences*, 108(28):11327–11331, 2011.